NOTICE: When government or other drawings, specifications or other data are used for any purpose other than in connection with a definitely related government procurement operation, the U. S. Government thereby incurs no responsibility, nor any obligation whatsoever; and the fact that the Government may have formulated, furnished, or in any way supplied the said drawings, specifications, or other data is not to be regarded by implication or otherwise as in any manner licensing the holder or any other person or corporation, or conveying any rights or permission to manufacture, use or sell any patented invention that may in any way be related thereto.

THE UPPER ATMOSPHERE

P. J. NAWROCKI, K. WATANABE AND L. G. SMITH

SCIENTIFIC REPORT #5

CONTRACT NO. AF 19(604)-7405

ELECTRONICS RESEARCH DIRECTORATE
AIR FORCE CAMBRIDGE RESEARCH LABORATORIES
AIR FORCE RESEARCH DIVISION
AIR RESEARCH AND DEVELOPMENT COMMAND
UNITED STATES AIR FORCE
BEDFORD, MASSACHUSETTS

FEBRUARY 1961

61-2-4

GEOPHYSICS CORPORATION OF AMERICA
BEDFORD, MASSACHUSETTS

AFCRL 73

GCA Technical Report
61-13-A

THE UPPER ATMOSPHERE

P.J. Nawrocki, K. Watanabe and L.G. Smith

Scientific Report #5

Contract No. AF 19(604)-7405

Project Monitor: S. Horowitz, AFCRL

ELECTRONICS RESEARCH DIRECTORATE
AIR FORCE CAMBRIDGE RESEARCH LABORATORIES
AIR FORCE RESEARCH DIVISION
AIR RESEARCH AND DEVELOPMENT COMMAND
UNITED STATES AIR FORCE
BEDFORD, MASSACHUSETTS

February 1961

GEOPHYSICS CORPORATION OF AMERICA
Bedford, Massachusetts

Requests for additional copies by Agencies of the Department of Defense, their contractors, and other Government agencies should be directed to the:

ARMED SERVICES TECHNICAL INFORMATION AGENCY
ARLINGTON HALL STATION
ARLINGTON 12, VIRGINIA

Department of Defense contractors must be established for ASTIA services or have their 'need-to-know' certified by the cognizant military agency of their project or contract.

All other persons and organisations should apply o the:

U.S. DEPARTMENT OF COMMERCE
OFFICE OF TECHNICAL SERVICES
WASHINGTON 25, D.C.

TABLE OF CONTENTS

1 Introduction

A systematic review and account of our knowledge of the constitution, composition and dynamics of the upper atmosphere including the more applicable physical parameters would be extremely difficult. Indeed, such a wealth of material exists in the literature that a thorough evaluation detracts from the main point of interest, namely, the pertinent atmospheric processes. The atmosphere combined with the incident solar and cosmic radiation provides the environment for the particle-field and particle-particle interactions. For this reason it is desirable to include the important features of the various geophysical parameters including, where available, the appropriate quantitative data. Fortunately, an excellent review of the dynamic properties of the terrestrial atmosphere has been given by Nicolet et al[1] and our discussion may be considered to supplement rather than include this review. Figure 1 gives a self-explanatory description of the Nicolet's nomenclature which defines the gross characteristics of the various regions of demarcation. The several mass motions of interest such as vertical drift and mixing, thermodynamics of heating, etc., will not be treated as a single topic, but rather as applications of particular microscopic or macroscopic processes.

The atmospheric parameters considered as essential to the definition of the atmospheric particle interactions are the total density including fluctuations and cross-correlations), temperature, molecular and atomic composition, electron density, and ion composition, and solar flux. Again, the amount of attention devoted to a particular topic herein is not indicative

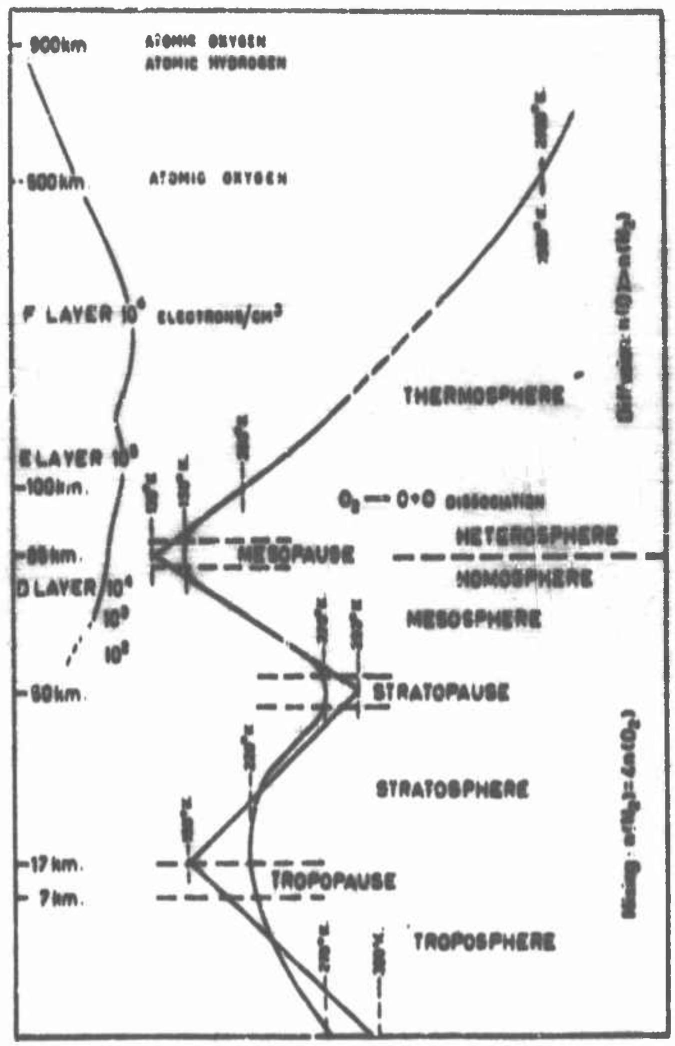

Figure 1. Atmospheric Nomenclature (after Nicolet)

of its importance to the physics of the upper atmosphere. Special attention has been paid to those areas which we consider to be treated inadequately in the literature or in which the GCA staff has particular competence. In addition, our view or interpretation of the data - when conflicting data or ambiguities exist - may be prejudiced by the requirement for self-consistancy.

In the pre-Sputnik era several model atmospheres were postulated defining the variation of descriptive geophysical parameters with altitude. Among the more comprehensive of these surveys was the 1956 ARDC Model Atmosphere. The introduction of satellites into the environment of interest in the 1957-58 era greatly accelerated the data gathering capability hitherto dependent upon the spatially and temporally limited rocket flight experiments. The satellite drag data thus accumulated frequently deviated from the theoretically postulated model atmospheres, and the observed time and space variations were incompatible with the assumptions of the mean model. For these reasons several attempts to modify the existent models were made circa 1959 and it has been demonstrated that among these the 1959 ARDC Model (fig. 2) is probably the most credulous at least for the mean of the diurnal, seasonal and solar fluctuations.

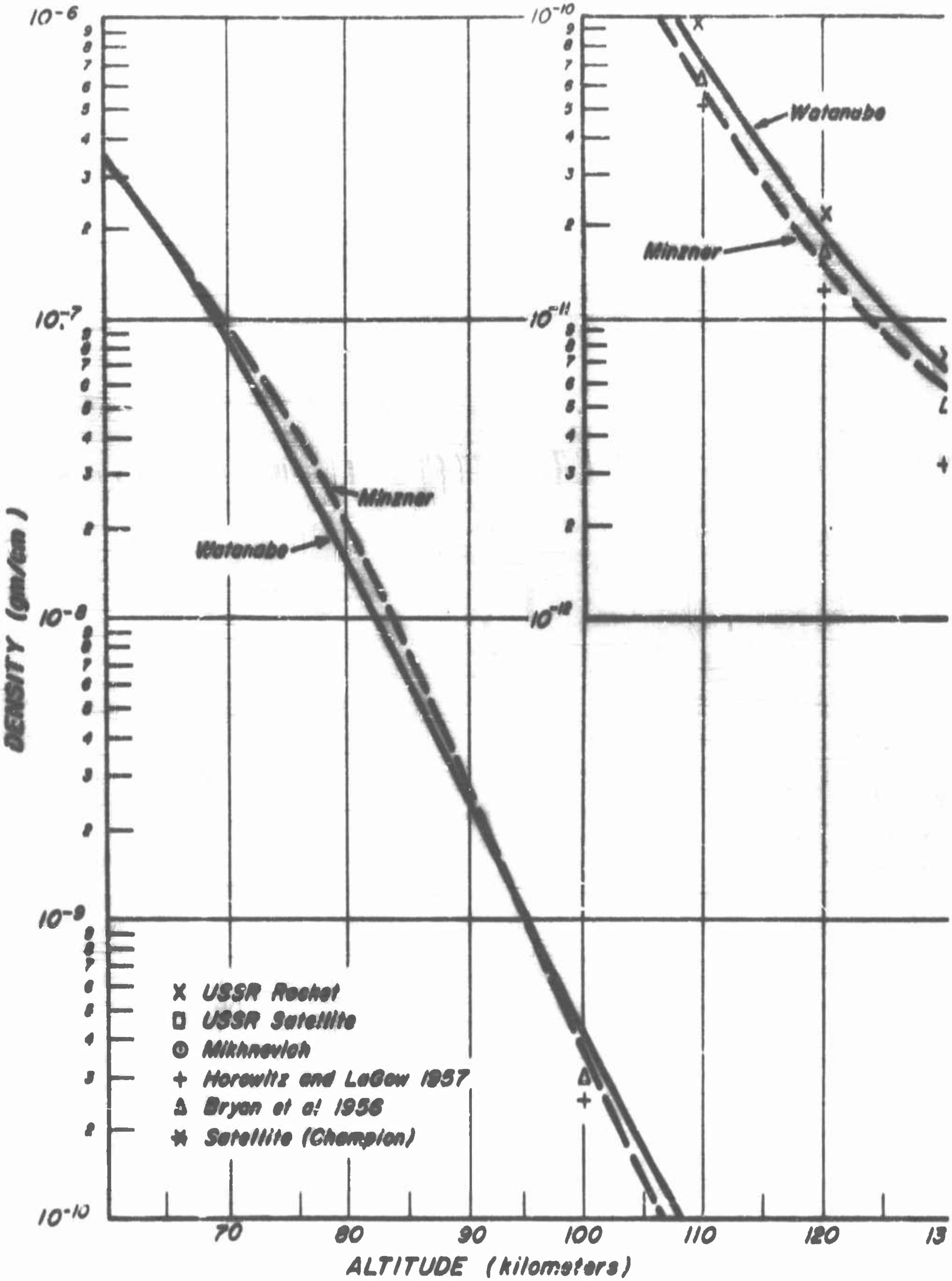

Figure 2a. Model Atmospheres 60-130 km

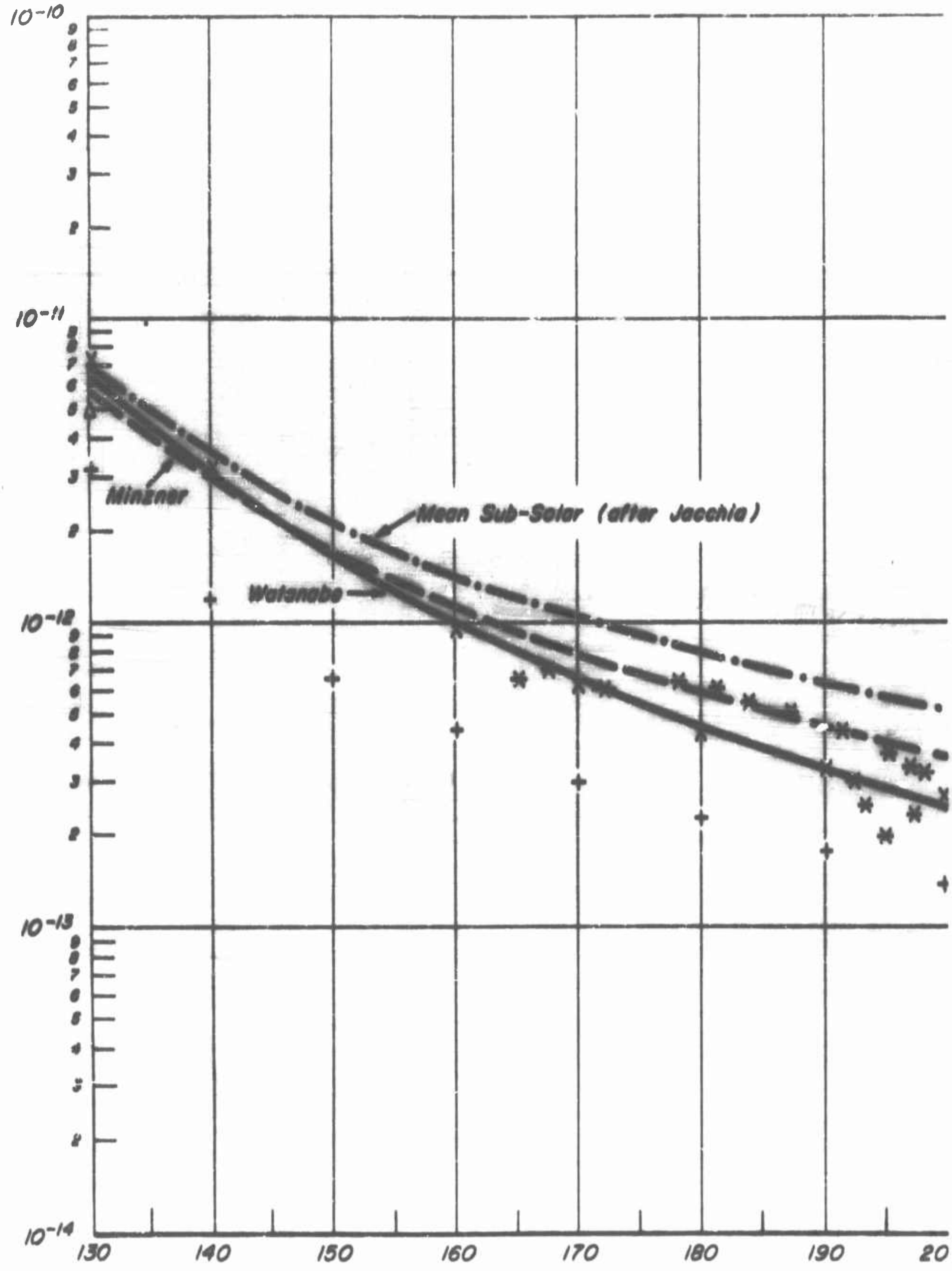

Figure 2b. Model Atmospheres 130-200 km

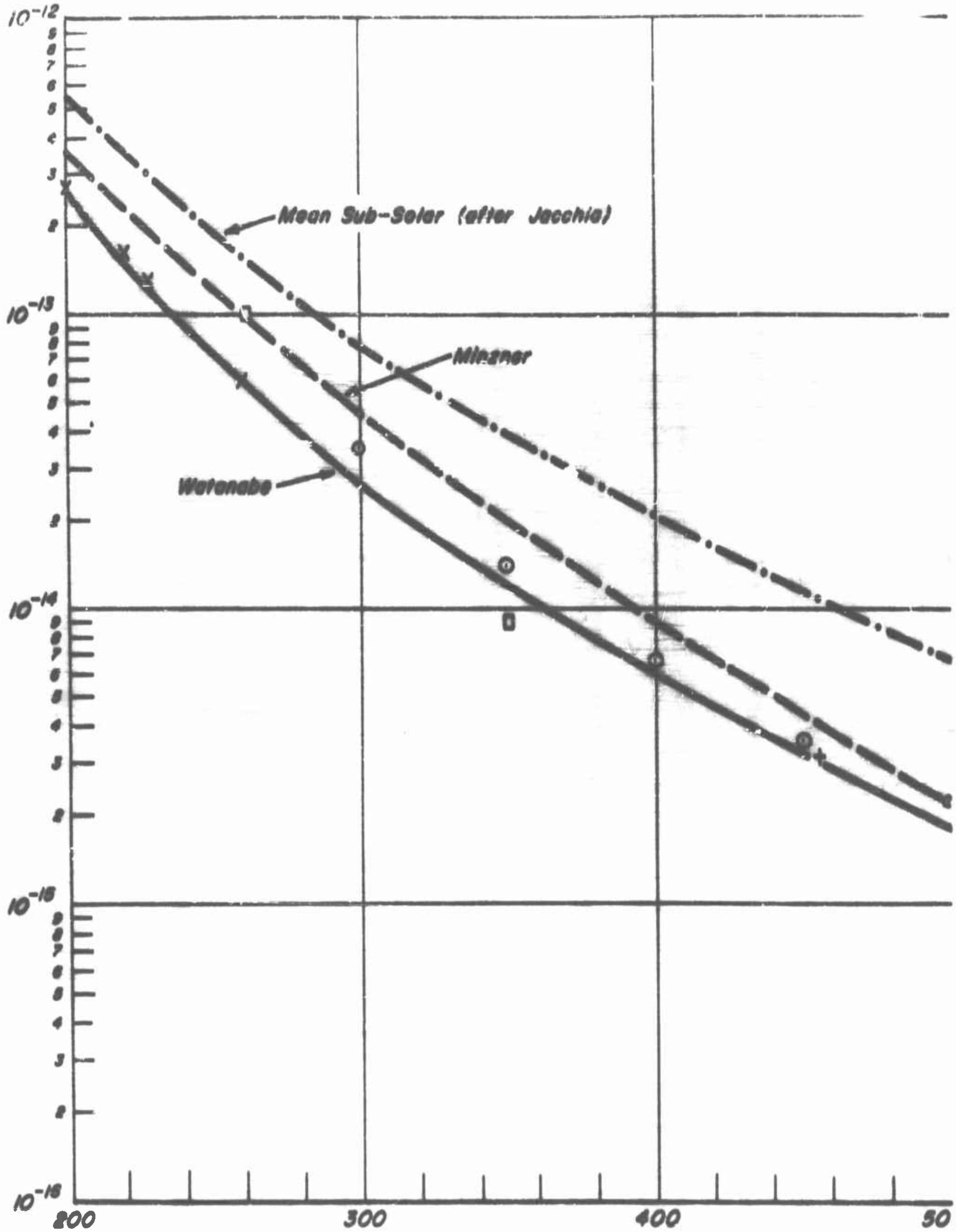

Figure 2c. Model Atmospheres 200-500 km

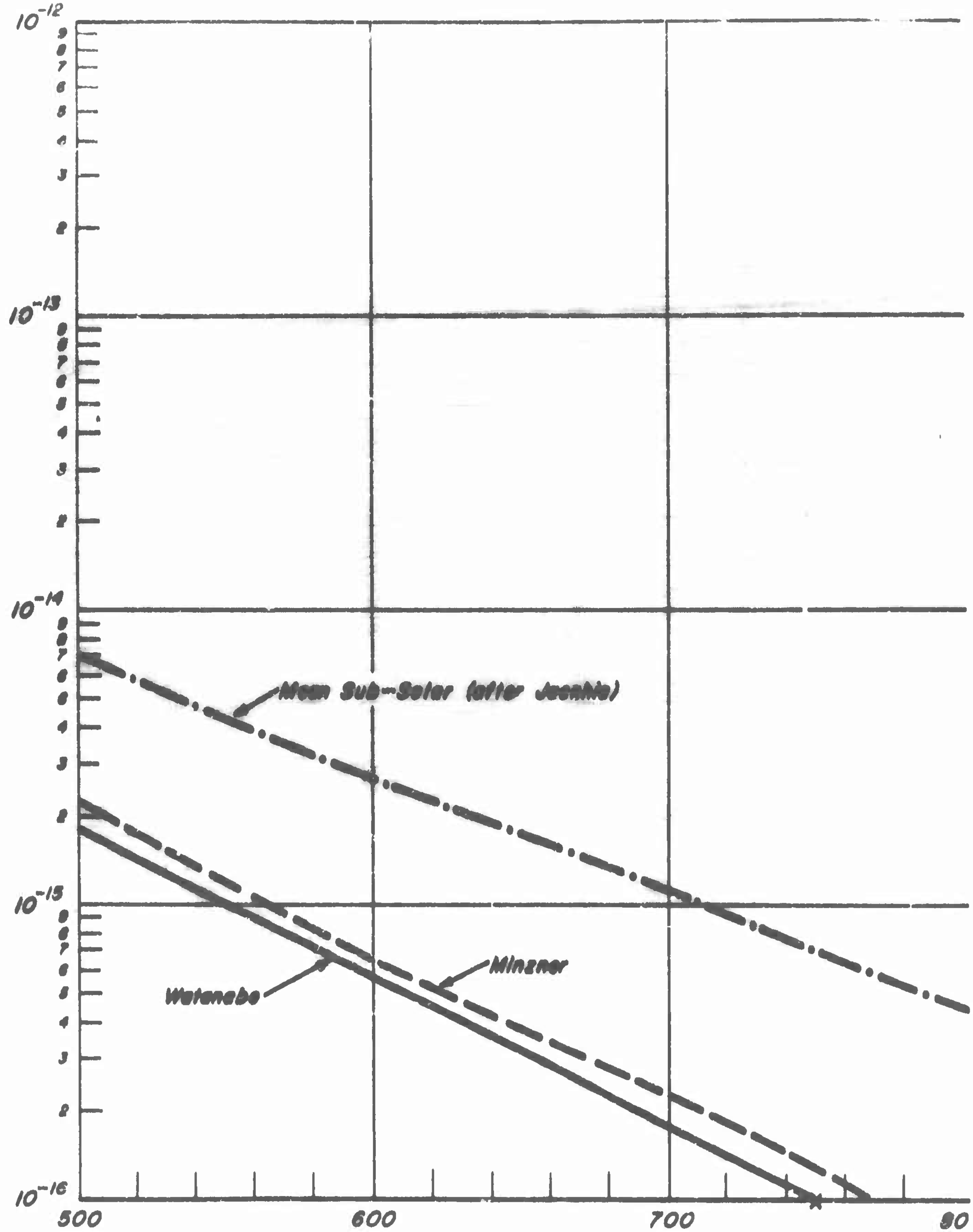

Figure 2d. Model Atmospheres 500-800 km

2. Density and Composition

2.1. The 1959 ARDC Model Atmosphere

In the 1959 revised model the molecular-scale-temperature has been computed as a function of the geopotential altitude consistent with data observed during several available rocket and satellite experiments. Starting at a well established point (53 km of the 1956 model), values of the molecular-scale-temperature were selected such that they defined densities in reasonable agreement (in slope) with the observed data. The ultimate result of this piece-meal construction was a profile (fig. 3) which showed a lower temperature (than previous models) in the 90km region and more spectacularly a considerable temperature increase at higher altitudes (105 - 170 km). An extension of the model from 600 km to 5 earth radii with a constant lapse rate of $\frac{dt}{dz} = 3.18^{o}/km$ and a mean molecular weight decreasing to unity (discounting electrons as a contributor to the mean molecular weight), yields values of mass density which are consistent with those derived by Chapman in the solar-corona analysis at the earth-sun distance. Minzner points out that extension of the model to altitudes above 700 km is tenuous since the assumption of hydrostatic equilibrium and the basic concept of temperature are probably inapplicable. Indeed, the action of the solar wind upon the magnetic B-field above a few earth radii as presented conceptually in another report* and the anisotropic behavior of the predominantly ionized medium in the terrestrial H-field precludes any simple hydrostatic model at these altitudes since the original equations of motion do not include forces other than gravitational.

* GCA Tech Report No 7 in the series (to be published)

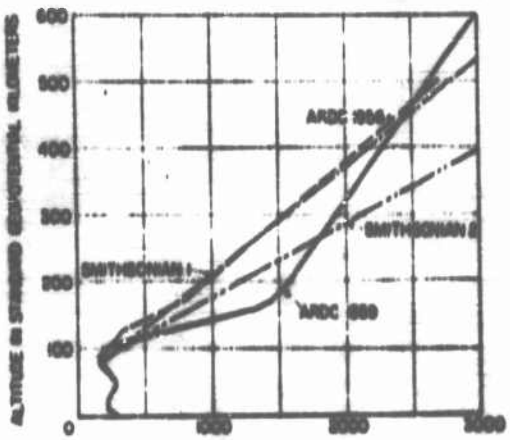

Figure 3. Comparison of Temperature-Altitude Functions for Various Atmospheric Models (after Minzner et al)

The 1959 ARDC atmosphere has been partially substantiated by the Russians (Tables 1 and 2) and by the work of Jacchia (Fig. 4), King-Hele, etc., if one ignores the latitude (auroral activity) and the temporal variations (solar bulge). Recognizing the various limitations, we include an abbreviated tabulation (Table 3) of the 1959 model including density, temperature, particle speed, mean free path, collision frequency, number density, and mean molecular weight.

TABLE 1: Structural Parameters of the Atmosphere at Heights 225-500 Km

Height km	N cm^{-3}	ρ gm/cm^3	H km	T K	P $dyne/cm^2$	p mm H_g
225	$6.01 \cdot 10^9$	$2.12 \cdot 10^{-13}$	40.0	936	$7.76 \cdot 10^{-4}$	$6.25 \cdot 10^{-7}$
230	5.31	1.79	40.6	938	6.88	5.54
235	4.7	1.7	41.3	941	6.1	4.92
240	4.17	1.42	42.0	946	5.44	4.4
245	3.71	1.25	42.8	952	4.88	3.94
250	3.3	1.1	43.5	958	4.36	3.54
255	2.94	$9.73 \cdot 10^{-14}$	44.3	964	3.91	3.17
260	2.64	8.66	45.2	971	3.54	2.88
265	2.36	7.77	46.0	979	3.19	2.6
270	2.12	6.83	47.0	987	2.89	2.35
275	1.91	6.1	47.9	996	2.63	2.14
280	1.72	5.44	48.8	1005	2.39	1.95
285	1.55	4.87	49.7	1015	2.17	1.78
290	1.4	4.36	50.7	1026	1.98	1.62
295	1.27	3.93	51.7	1037	1.82	1.49
300	1.15	3.53	52.7	1048	1.66	1.37
305	1.07	3.26	53.7	1059	1.56	1.29
310	$9.57 \cdot 10^8$	2.9	54.5	1072	1.42	1.17
315	8.73	2.63	55.9	1084	1.31	1.008
320	7 98	2.39	57.0	1097	1.21	1.0
325	7.31	2.17	58.1	1110	1.12	$9.28 \cdot 10^{-6}$
330	6.7	1.98	59.2	1124	1.04	8.62
335	6.17	1.82	60.3	1138	$9.69 \cdot 10^{-5}$	8.06
340	5.68	1.66	61.5	1153	9.04	7.52
345	5.22	1.52	62.8	1169	8.96	7.46
350	4.82	1.4	64.8	1185	7.88	6.58
355	4.46	1.29	65.2	1200	7.39	6.18
360	4.13	1.19	66.7	1219	6.95	5.82
365	3.86	1.1	68.1	1237	6.59	5.53
370	3.56	1.02	69.5	1257	6.18	5.19
375	3.31	$9.41 \cdot 10^{-15}$	70.9	1276	5.83	4.9
380	3.08	8.72	72.4	1295	5.51	4.64
385	2.92	8.24	73.9	1305	5.26	4.44
390	2.69	7.56	75.2	1335	4.96	4.19
395	2.52	7.07	76.7	1353	4.71	3.98
400	2.36	6.6	78.9	1373	4.47	3.79
405	2.21	6.16	79.7	1393	4.25	3.6
410	2.08	5.78	81.2	1417	4.07	3.46
415	1.95	5.41	82.9	1440	3.88	3.3
420	1.84	5.09	84.6	1465	3.72	3.17
425	1.73	4.79	86.3	1489	3.56	3.04
430	1.64	4.51	88.1	1514	3.43	2.93
435	1.55	4.25	90.0	1539	3.29	2.82
440	1.47	4.03	91.7	1563	3.17	2.72
445	1.39	3.8	93.6	1589	3.05	2.62
450	1.32	3.6	95.5	1614	2.94	2.53
455	1.25	3.4	98.6	1643	2.84	2.44
460	1.19	3.23	99.9	1675	2.75	2.37
465	1.13	3.06	102.0	1709	2.66	2.3
470	1.08	2.92	104.5	1745	2.6	2.25
475	1.03	2.79	107.0	1781	2.53	2.19
480	$9.82 \cdot 10^7$	2.65	109.3	1810	2.45	2.13
485	9.4	2.53	111.5	1845	2.39	2.08
490	8.97	2.42	113.9	1880	2.33	2.02
495	8.61	2.31	116.5	1917	2.28	1.98
500	8.24	2.21	119.0	1953	2 22	1 94

TABLE 2. Values of the Density (in gm-cm^{-3}) at Various Heights from Manometer

Height, km	Rocket Data: Containers and rockets Mean latitude of European USSR	Rocket Data: Viking-7 33° N lat.	Rocket Data: Aerobee-Hi 59° N lat.	Drag Data: 1957 α_1 1957 α_2 1957 β_1 (10,11)	Drag Data: 1957 α_1 1957 α_2 1957 β_1 1958 α 1958 β_2 1958 (19-25)
100	$4\cdot10^{-10}$	$2.5\cdot10^{-10}$	$7\cdot10^{-10}$	---	---
110	$9.8\cdot10^{-11}$	$5\cdot10^{-11}$	$1.5\cdot10^{-10}$	---	---
120	$2.2\cdot10^{-11}$	$1.2\cdot10^{-11}$	$2\cdot10^{-11}$	---	$6.9\cdot10^{-11}$
130	$7.4\cdot10^{-12}$	$3.3\cdot10^{-12}$	$6\cdot10^{-12}$	---	$3.01\cdot10^{-11}$
140	$3.2\cdot10^{-12}$	$1.2\cdot10^{-12}$	$3\cdot10^{-12}$	---	$1.69\cdot10^{-11}$
150	$1.6\cdot10^{-12}$	$6.6\cdot10^{-13}$	$2\cdot10^{-12}$	---	$8.07\cdot10^{-12}$
160	$9.5\cdot10^{-13}$	$4.3\cdot10^{-13}$	$1.3\cdot10^{-12}$	---	$4.70\cdot10^{-12}$
170	$6.4\cdot10^{-13}$	$3.0\cdot10^{-13}$	$1\cdot10^{-12}$	---	$2.89\cdot10^{-12}$
180	$4.4\cdot10^{-13}$	$2.3\cdot10^{-13}$	$8\cdot10^{-13}$	---	$1.87\cdot10^{-12}$
186	---	---	---	---	$6.7\cdot10^{-13}$
190	$3.3\cdot10^{-13}$	$1.8\cdot10^{-13}$	$7.5\cdot10^{-13}$	---	$1.25\cdot10^{-12}$
197 ± 1	---	---	---	---	$7.0\cdot10^{-13}$
200	$2.7\cdot10^{-13}$	$1.4\cdot10^{-13}$	$7\cdot10^{-13}$	---	$(3-8.65)\cdot10^{-13}$
201 ± 4	---	---	---	---	$6.7\cdot10^{-13}$
202 ± 4	---	---	---	---	$7.37\cdot10^{-13}$
206 ± 4	---	---	---	---	$5.4\cdot10^{-13}$
210	$2.0\cdot10^{-13}$	$1.1\cdot10^{-13}$	6.0·1[illegible]	---	$6.04\cdot10^{-13}$
211 + 4	---	---	---	---	$4.6\cdot10^{-13}$
212	---	---	---	---	$(4.4-4.8)\cdot10^{-13}$
215	---	---	---	---	$4.7\cdot10^{-13}$
220	$1.6\cdot10^{-13}$	$9.0\cdot10^{-13}$	---	---	$(3.5-5.7)\cdot10^{-12}$
225	---	---	---	$(2.9-4.1)\cdot10^{-13}$	---
228	---	---	---	$(2.4-3.2)\cdot10^{-13}$	---
230	$1.25\cdot10^{-13}$	---	---	---	$3.32\cdot10^{-13}$
232	---	---	---	---	$1.5\cdot10^{-13}$
233	---	---	---	---	$2.2\cdot10^{-13}$
240	$1.1\cdot10^{-13}$	---	---	---	$2.51\cdot10^{-13}$
241	---	---	---	---	$2.5\cdot10^{-13}$
250	$9\cdot10^{-14}$	---	---	$(1.5-1.6)\cdot10^{-13}$	$(1.1-1.9)\cdot10^{-13}$
260	$6.9\cdot10^{-14}$	---	---	---	$1.51\cdot10^{-13}$
270	---	---	---	$(9.4-10)\cdot10^{-14}$	$1.19\cdot10^{-13}$
275	---	---	---	---	$8.5\cdot10^{-14}$
280	---	---	---	---	$9.51\cdot10^{-14}$
290	---	---	---	$(5.8-7.0)\cdot10^{-14}$	$7.68\cdot10^{-14}$
300	---	---	---	---	$(5-6.27)\cdot10^{-14}$
310	---	---	---	$(3.8-4.7)\cdot10^{-14}$	$5.16\cdot10^{-14}$
320	---	---	---	---	$4.29\cdot10^{-14}$
330	---	---	---	$(2.6-3.2)\cdot10^{-14}$	$3.58\cdot10^{-14}$
340	---	---	---	---	$3.02\cdot10^{-14}$
350	---	---	---	$(1.8-2.2)\cdot10^{-14}$	$(2.1-3)\cdot10^{-14}$
360	---	---	---	---	$2.18\cdot10^{-14}$
368	---	---	---	$(1.4-1.5)\cdot10^{-14}$	$(1.4-1.5)\cdot10^{-14}$
370	---	---	---	---	$1.87\cdot10^{-14}$
400	---	---	---	---	$1.5\cdot10^{-14}$
405	---	---	---	---	$9.3\cdot10^{-15}$ $(9^{+6}_{-4})\cdot10^{-15}$
450	---	---	---	---	$(1.0-4.5)\cdot10^{-15}$
500	---	---	---	---	$(2.3-6)\cdot10^{-15}$
550	---	---	---	---	$(2.2-4)\cdot10^{-15}$
600	---	---	---	---	2.10^{-15} $6.8\cdot10^{-16}$
650	---	---	---	---	1.10^{-15} $3.8\cdot10^{-16}$
700	---	---	---	---	$7\cdot10^{-16}$
720	---	---	---	---	$(1.2 \pm 0.3)\cdot10^{-16}$

Above notations are conventional designations of the satellites.

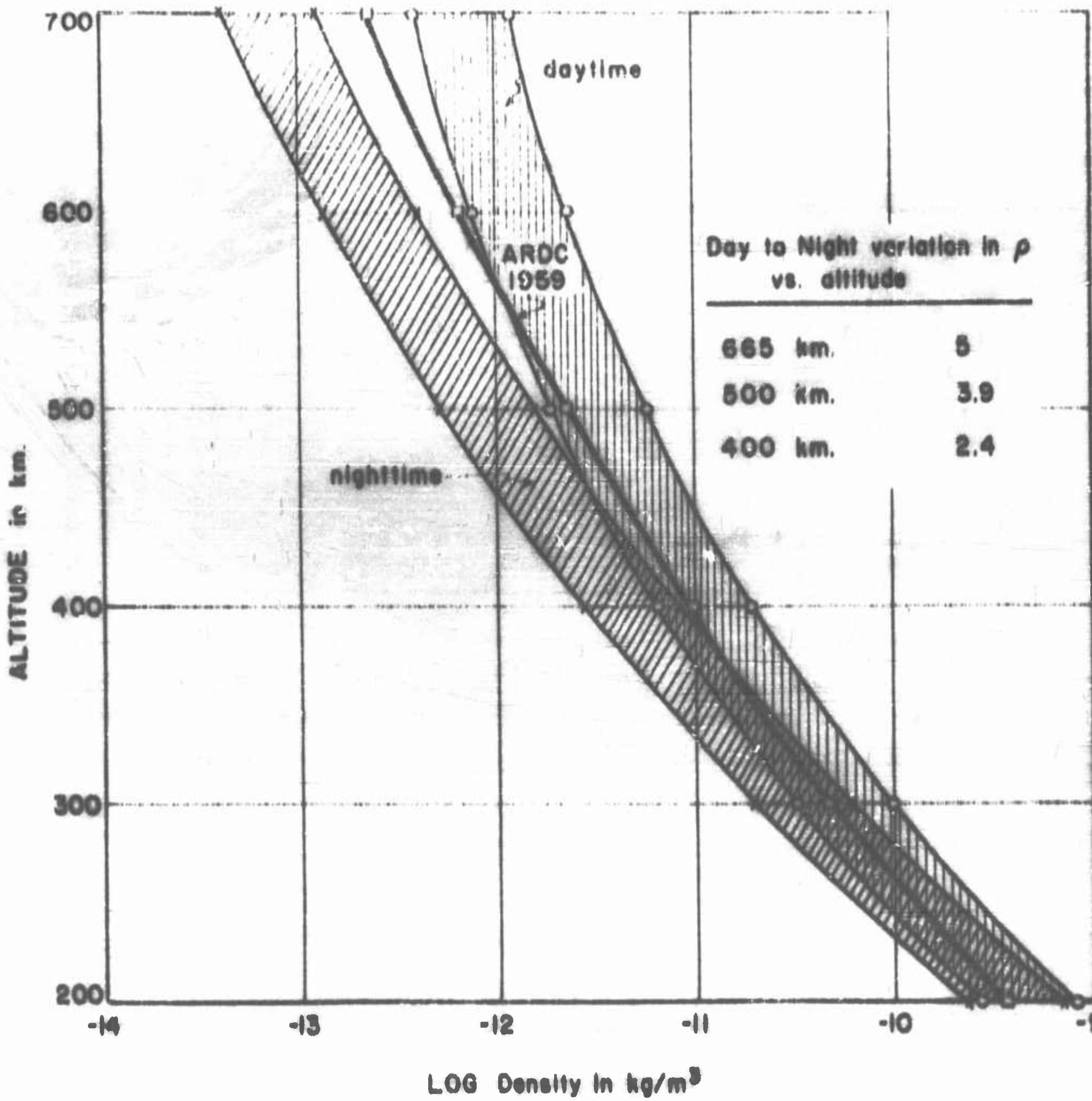

Range of possible Daylight and Nighttime densities as computed by Jacchia (Smithsonian Special Report No. 39) vs. altitude in km. in comparison with the ARDC Model Atmosphere 1959.

Figure 4

TABLE 3. Atmospheric Properties as a Function of Altitude (1959 ARDC)

ALTITUDE Z Km	Kft	Miles	DENSITY, Kg m^{-3}	KINETIC TEMPERATURE T, °K	PARTICLE SPEED V, m sec^{-1}	MEAN FREE PATH L, m	COLLISION FREQUENCY, sec^{-1}	NUMBER DENSITY n, m^{-3}	PRESSURE mm Hg	MOLECULAR WEIGHT M
0	0.0	0.0	1.22	288	459	6.63^{-8}	6.90^{+9}	2.55^{+25}	760.00	28.966
10	32.808	6.21	4.14^{-1}	223	400	2.00^{-7}	2.06^{+9}	8.60^{+24}	198.80	28.966
20	65.616	12.42	8.89^{-2}	217	393	9.10^{-7}	4.35^{+8}	1.85^{+24}	41.50	28.966
30	98.424	18.63	1.78^{-2}	231	411	4.50^{-6}	9.03^{+7}	3.71^{+23}	8.89	28.966
40	131.232	24.84	4.00^{-3}	261	437	2.00^{-5}	2.15^{+7}	8.32^{+22}	2.25	28.966
50	164.040	31.05	1.08^{-3}	283	454	7.50^{-5}	6.06^{+6}	2.25^{+22}	.659	28.966
60	196.848	37.26	3.51^{-4}	254	431	2.30^{-4}	1.86^{+6}	7.26^{+21}	.192	28.966
70	229.656	43.47	1.00^{-4}	210	392	8.10^{-4}	4.80^{+5}	2.08^{+21}	4.52^{-2}	28.966
80	262.464	49.68	2.12^{-5}	166	348	3.10^{-3}	9.10^{+4}	4.42^{+20}	7.56^{-3}	28.97
90	295.272	55.89	2.84^{-6}	166	348	2.90^{-2}	1.22^{+4}	5.90^{+19}	1.02^{-3}	28.97
100	328.080	62.10	3.73^{-7}	199	382	.22	1.75^{+3}	7.80^{+18}	1.60^{-4}	28.90
110	360.888	68.31	5.93^{-8}	287	459	1.36	3.37^{+2}	1.24^{+18}	3.68^{-5}	28.82
120	393.696	74.52	1.48^{-8}	477	593	5.45	1.09^{+2}	3.10^{+17}	1.53^{-5}	28.71
130	426.504	80.73	5.95^{-9}	665	702	13.50	52.10	1.25^{+17}	8.63^{-6}	28.59
140	459.312	86.94	3.02^{-9}	850	795	26.30	30.00	6.40^{+16}	5.63^{-6}	28.45

From: Minzner, Champion, Pond, The ARDC Model Atmosphere - 1959, Geophysics Research Directorate, AFCRS, Bedford, Mass. 1959.

TABLE 3. Atmospheric Properties as a Function of Altitude (Continued)

ALTITUDE Z Km	Kft	Miles	DENSITY , Kg m^{-3}	KINETIC TEMPERATURE T, °K	PARTICLE SPEED $\bar{V}$, m sec^{-1}	MEAN FREE PATH L, m	COLLISION FREQUENCY , sec^{-1}	NUMBER DENSITY n, m^{-3}	PRESSURE mm Hg	MOLECULAR WEIGHT M
150	492.120	93.15	1.76^{-9}	1031	879	45.10	19.50	3.75^{+16}	4.00^{-6}	28.270
160	524.928	99.36	1.12^{-9}	1207	955	70.00	13.60	2.41^{+16}	3.01^{-6}	28.04
170	557.736	105.57	7.94^{-10}	1323	1055	98.10	10.02	1.72^{+16}	2.36^{-6}	27.75
180	590.544	111.78	6.01^{-10}	1371	1030	128.00	8.06	1.32^{+16}	1.88^{-6}	27.36
190	623.352	117.99	4.68^{-10}	1389	1046	161.00	6.50	1.05^{+16}	1.51^{-6}	26.85
200	656.160	124.20	3.67^{-10}	1404	1062	201.00	5.30	8.40^{+15}	1.22^{-6}	26.32
220	721.776	136.62	2.34^{-10}	1414	1088	303.00	3.60	5.60^{+15}	8.16^{-7}	25.29
240	787.392	149.04	1.53^{-10}	1415	1110	446.00	2.50	3.86^{+15}	5.55^{-7}	24.32
260	853.008	161.46	1.02^{-10}	1416	1131	645.00	1.00	2.60^{+15}	3.84^{-7}	23.44
280	918.624	173.88	6.91^{-11}	1418	1152	919.00	1.30	1.86^{+15}	2.70^{-7}	22.65
300	984.240	186.30	4.75^{-11}	1423	1172	1,294.00	0.90	1.31^{+15}	1.92^{-7}	21.95
400	1312.320	248.40	9.00^{-12}	1480	1266	6,098.00	0.21	2.77^{+14}	4.25^{-8}	19.56
500	1640.400	310.50	2.20^{-12}	1576	1351	23,180.00	0.068	7.29^{+13}	1.19^{-8}	18.28
600	1968.480	372.60	6.62^{-13}	1691	1429	74,270.00	0.019	2.28^{+13}	3.98^{-9}	17.52
700	2296.560	434.70	2.30^{-13}	1812	1501	207,500.00	0.0072	8.14^{+12}	1.53^{-9}	17.03

NOTE: A one- or two-digit number (preceded by a plus or minus sign) following an entry indicates the power of 10 by which that entry should be multiplied.

FORMULAE FOR 1959 ARDC STANDARD ATMOSPHERE

1. **GEOPOTENTIAL ALTITUDE** - H

$$H = \frac{\frac{g_o}{G} rZ}{r + Z} = \frac{rZ}{r + Z}$$

2. **GEOMETRIC ALTITUDE** - Z

$$Z = \frac{rH}{\frac{g_o}{G}(r-H)} = \frac{rH}{r - H}$$

3. **DENSITY** - ρ

$$\rho = \frac{PM}{R^* T} = \frac{M_o P}{R^* T_M}$$

4. **PARTICLE SPEED** (Arithmetic Average) - $\bar{v}$

$$\bar{v} = \left[\frac{8R^* T_M}{\pi M}\right]^{1/2} = \left[\frac{8R^*}{\pi M_o} \quad (T_M)_o\right]^{\frac{1}{2}}$$

5. **MEAN FREE PATH** - L

$$L = \frac{1}{\sqrt{2}\,\pi \sigma^2 n} = \frac{R^* M T_M}{\sqrt{2}\,\pi \sigma^2 N M_o P}$$

6. **COLLISION FREQUENCY** - ν

$$\nu = \frac{\bar{v}}{L}$$

7. **PRESSURE** - P

For $L_M \neq 0$

$$P = P_b \left[\frac{(T_M)_b}{(T_M)_b + L_M(H - H_b)}\right]^{G M_o / R^* L_M}$$

For $L_M = 0$

$$P = P_b \exp \left[\frac{-GM_0(H - H_b)}{R^*(T_M)_b} \right]$$

8. NUMBER DENSITY - n

$$n = \frac{N\rho}{M'} = \frac{NM_0 P}{R^* M' T_M}$$

9. MOLECULAR WEIGHT - M

For Geopotential Altitudes - (H)

For $-5km \leq H \leq 90km$

$$M = 28.966$$

For $90km \leq H \leq 180km$

$$M = 22 - 5.044,835,74 \arctan \left[\frac{H-220}{25} \right]$$

For $180km \leq H$

$$M = 27.106 - 7.935,697,10 \arctan \left[\frac{H - 180}{140} \right]$$

2.2 Fine Structure of the Atmospheric Density (Secular Variations)

The attitude of the geophysicist during the past few years toward the subject of atmospheric density has been changing. The notion seemed to be quite general among the primary investigators that the density profile was an invariant and as a result the construction of static atmospheric models was a popular pastime. The satellite-drag data has been instrumental in demonstrating that the atmospheric density has considerable fine structure above 100 km - exhibiting diurnal and seasonal variations as well as those correlated with sun spot index, degree of auroral activity, etc. Therefore any particular static model is incapable of approximating the atmospheric density for all locations and times. The relation of satellite drag to orbital and atmospheric parameters has been derived by several investigators including King-Hele, Cook, and Walker[2] and is given approximately by

$$\rho H^{\frac{1}{2}} = - \frac{\sqrt{2/\pi}}{3C_D} \frac{dP}{dt} \frac{m}{AP} \sqrt{\frac{\epsilon}{a}} \left[1 - 2\epsilon + \frac{5\epsilon^2}{2} - \frac{H}{8a\epsilon} \left(1 - 10\epsilon + \frac{7H}{16a\epsilon} \right) \right] \tag{1}$$

where

ρ = atmospheric density at satellite perigee

H = atmospheric scale height near satellite perigee (function of temperature and molecular weight).

C_D = drag coefficient

dP/dt = satellite acceleration

m = mass of satellite

A = effective cross section of satellite

F = factor to account for rotation of atmosphere

ϵ = orbital eccentricity

a = semi-major axis of orbit.

The diurnal component had been anticipated in the early investigations on the upper atmosphere - at least for altitudes above 90 km. However, rocket observations were too isolated to resolve the question definitely. (Indeed the Fort Churchill flights (to 200 km) demonstrated a high pressure (or density) which was tentatively interpreted in terms of temporal variations.) Even the satellite data from 1957 α and 1957 β where perigee occurred at about 200 km failed to conclusively exhibit the appropriate correlations because of the masking affect of very short term perturbations due to solar flares and enhanced sunspot activity. The data derived from Vanguard I and its carrier 1958 β_1 and β_2) with a perigee at 650 km also could not demonstrate the diurnal density variation during its first year since its perigee remained in the sunlit portion for the entire period between launch in March, 1958 until mid-April of 1959. However, since 1959, the perigee of this pair as well as the perigees of 1959 α_1, 1959 α_2, 1959 β_1, 1959 β_2, and 1960 γ_2, have made the traverse from sunlit portion to the earth's shadow and/or vice verse. These latter satellites have perigees between 180 and 650 km and orbital inclinations of from 32.9 to 51.3 degrees. These inclinations therefore establish the regions within which the drag data has fully established particular temporal variations. A review of the drag data from earlier satellites with lower perigee altitudes indicates that there was a minor effect - a density variation dependent upon the GSP angle in which the magnitude of the variation appeared to decrease with decreasing perigee altitude until the effect disappeared around 200 km.

According to orbital theory, low altitude satellites orbiting in an atmosphere whose density is a function of altitude but not time would exhibit a period with a systematic decrease (decreasing altitude of perigee) which depends only upon the invariant density-altitude relation. For such a situation, the rate of change of the orbital period would remain essentially constant for long periods over the small range in perigee altitude.

The observed drag data clearly showed that the large variations in the rate of change of the orbital period were correlated with a passage of the satellite from sunlit to dark region (or vice versa).

However, a more careful examination of the data showed that even during the time when the perigee continued to remain in either a sunlit or a dark region of the atmosphere, the rate of change of the period appeared to be inversely related to the angular distance of perigee from the earth's sub-solar point. This angle is referred to as the geocentric-sun-perigee angle (GSP) and, of course shows a diurnal and seasonal variation to a fixed terrestrial observer.

Jacchia[3] has examined the variations in atmospheric density and observed in addition to the large diurnal effect the atmospheric bulge which occurs in the general vicinity of the sub-solar point but perhaps delayed two hours due to the earth's rotation):

a) an erratic fluctuation with a main component defined by a 27 day period excellently correlated with the observed solar flux at 10 and 20 cm wavelengths. Below 200 km, the fluctuations are small and independent of the OSP. At heights above 200 km, the fluctuations are large in the subsolar bulge but remain small in the earth's shadow.

b) transient increases in the density of the entire atmosphere above 200 km during magnetic storms. Jacchia[4] has reportedly observed two such events in which the perturbation was in phase with the magnetic storm so far as intensity and duration were concerned.

It must be pointed out that these conclusions depend upon the satellite-drag-derived data in which the observable involves the product of the density and the square root of the scale height. Since the latter is a function of temperature and since temperature and particularly the distribution of particle energies is unknown, the density measurements may be subject to some further ambiguity.

Jacchia[5] has worked out an empirical formulation of the expression $\rho H^{\frac{1}{2}}$ in terms of the geometric height, the 20 cm solar flux (F_{20}) and the angular distance from the center of the diurnal bulge, viz.,

$$\rho H^{\frac{1}{2}} = f_o(Z)\, F_{20} \left[1 + 0.185 \left(\exp(0.006\, Z) - 2 \right) \cos^6 (\psi/2) \right] \tag{2}$$

Comparison of this relation with the observed behavior of the satellites is given in fig. 5, and the diurnal bulge as a function of altitude in fig. 6.

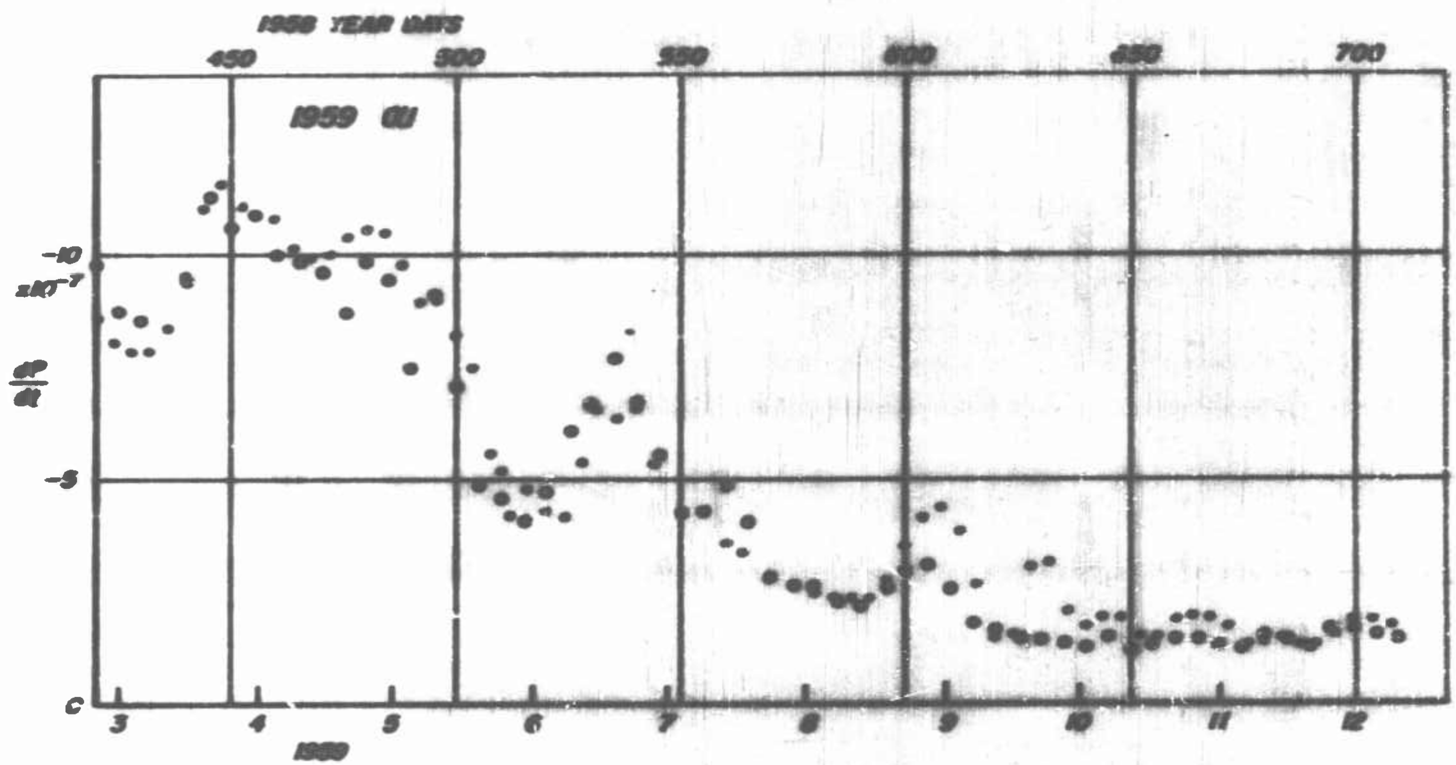

Figure 5. Observed Accelerations of Satellite 1959 α 1 (dots) Compared with Calculated Accelerations (open circles)(after Jacchia)

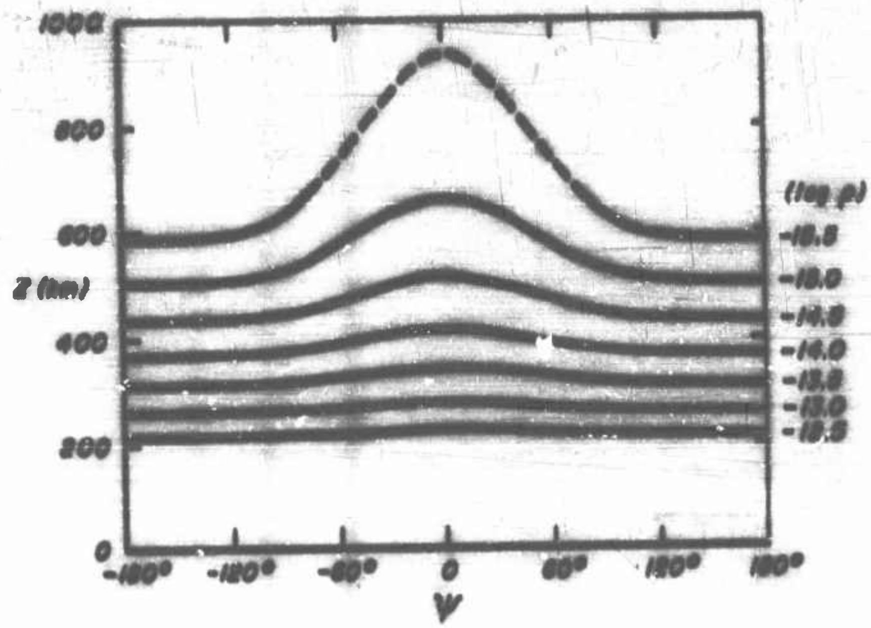

Figure 6. Heights of Surfaces of Equal Density above a Great Circle Across the Diurnal Bulge, Computed for a 20 cm Solar Flux of 200 x 10^{-22} watt/cm^2 cycles/sec. The value of log ρ corresponding to each curve is shown (after Jacchia).

2.3 Auroral Zones (latitude variation)

In addition to the diurnal bulge associated with solar electromagnetic radiation, Jacchia has noted apparent relationship between the observed atmospheric density and the solar corpuscular flux (the solar "wind"). Since this stream is predominantly ionized, corpuscles tend to be confined to the field lines and enter the lower atmosphere preferentially in the auroral zones. Indeed, as mentioned previously, pressure measurements at altitudes near 200 km over Fort Churchill were much greater than those measured over lower latitudes. The measurements refer to different phases of the solar cycle, but it was suggested in some quarters that the feature was more or less permanent and due to auroral particles. A consequence of this concept involves the effect of auroral activity on the thermobalance of the atmosphere (first considered by Bates.[6]) During a strong arc, the photon flux of the first negative system of nitrogen is about 3 x 10[illegible] cm^{-2} sec^{-1} (Omholt[7]), which, using the appropriate cross sections, corresponds to an ionisation flux of about 10^{13} cm^{-2} sec^{-1}. The associated thermal energy transferred to the atmosphere will be of the order 10^{14} ev cm^{-2} sec^{-1}. The altitude distribution of the heat source will have much the same shape as the luminosity curve so that the energy will be deposited in the region near 105 km for the majority of auroras. The mean thermal energy supplied by ionising radiation to the region above the base of the F_1 layer is at least 1×10^{10} ev cm^{-2} sec^{-1} (Bates[8]). Although the heating associated with visible auroras cannot be significant within the content of the overall thermobalance of the atmosphere (Bates[6]), appreciable local heating may occur. If we adopt 10 km for the vertical extent of a strong arc, the associated heat source is about 10^8 ev cm^{-3} sec^{-1}, which for a number density of 4×10^{12} cm^{-3} yields a rate of gain of thermal energy per particle of about 2×10^{-5} ev sec^{-1}. The temperature rise is therefore about 5°K per minute. In some auroras the luminosity distribution is greatly extended in altitude (Harang,[9] Harang and Ohmholt,[10]) and a rapid rise in temperature may occur at the upper levels. The rise will be limited by air motions and by heat conduction.

VanAllen, McIlwain and Ludwig[11] and Krassovsky[12] have drawn attention to the possibility that atmospheric heating may be caused by particles from the Van Allen radiation belts. Again, as Bates[13] has remarked the contribution cannot be of major importance to the heat economy of the atmosphere. According to Bates, the required energy flow is 4×10^{18} ergs sec^{-1} whereas Dessler and Vestine[14] suggest an upper limit of 6×10^{22} ergs for the energy content of the radiation belts. A very short turnover time would therefore be necessary.

The possibility that the trapped particles cause heating in the auroral zones has been discussed by Jastrow[15,16]. He supposes that the heat source arising from the particles can be written in the form

$$q = F \sigma E n \tag{3}$$

where F is the flux of energetic electrons, σ is the inelastic cross section, E is the mean energy transferred per collision and n is the atmospheric number density. For electrons of 10 keV, Jastrow[16] takes $\sigma = 10^{-18}$ cm^2 and E = 20 ev, corresponding to an effective heat transfer cross section of 2×10^{-17} ev cm^2.

The significance of these values is not entirely clear. The primary mechanism of heat transfer is that of momentum transfer during a collision and the mean energy transferred per collision by a 10 kev electron is about 0.5 ev. The associated cross section is uncertain but is probably of the order of 10^{-18} - 10^{-19} cm^2 giving a primary heat transfer cross section of between 5×10^{-19} ev cm^2. The primary contribution is however negligible compared to that arising from secondary electrons. Thus the stopping cross section associated with excitation and ionization is 6×10^{-16} ev cm^2 [17] and a large fraction of the associated energy will ultimately be converted into thermal energy (through such mechanisms as direct elastic collisions of the secondaries and recombination processes). Associated with the heating effect ionization and excitation occur with effective cross sections (including the secondary processes) of about 3×10^{-17} cm^2. The calculation of the distribution of energy deposition in the atmosphere by the trapped electrons presents a very difficult problem because of the importance of multiple scattering of the primary and secondary electrons, but the heating distribution should be similar to the luminosity distribution.

In his computations, Jastrow has adopted an energy flux of 4000 erg cm^{-2} sec^{-1} of electrons with energies above 10 kev at an altitude of 300 km. He assumes that the flux is inversely proportional to the ambient density up to altitudes ranging from 400 to 600 km and deduces that the temperature in the auroral zone will rise to about 2500°K. However, his assumed flux would also give rise to an electron production rate of 3×10^{4} cm^{-3} sec^{-1} and to a photon production rate of at least 10^{12} quanta per cm^{2} column per sec.

It may be remarked that heating by *fast* particle collisions is always associated with the production of ionization and excitation and that in order to obtain heating without luminosity it is necessary to invoke a flux of slowly moving particles.

We note finally that Dessler(18) has suggested that heating by hydromagnetic waves may be important but that according to Akasofu this contribution (see fig. 7 and table 4) is negligible.

TABLE 4. The Adopted Amplitude at 300 km above the Auroral Zone, Q_e and ΔT in the F2-region and Q at 90 km

Frequency (c/s)	Period (sec)	h (γ)	Q_e (ergs/cm^3 sec)	ΔT (°K)	Q (ergs/cm^3 sec)
			F2-Region		90 km
1	1	1	10^{-10}	0.21 (220 km)	2.08×10^{-22}
0.1	10	10	1.48×10^{-10}	0.03 (200 km)	1.81×10^{-14}
0.01	100.	31.6	2.30×10^{-10}	1.18 (190 km)	2.10×10^{-13}

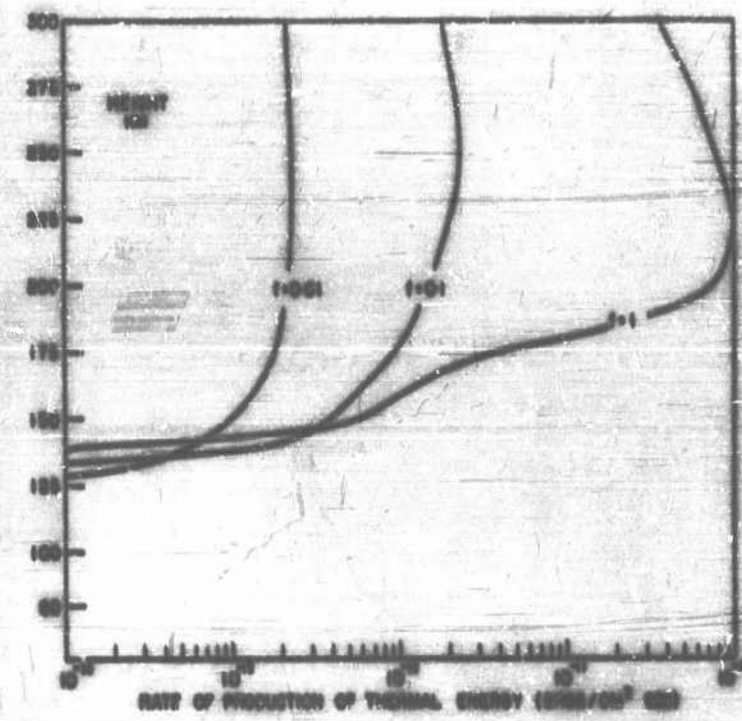

Figure 7. Thermal Energy Production Rate in the Ionosphere (ergs/cm^3 sec) for Frequencies $f = 1$, 0.1 and 0.01 c/s, for Waves of Amplitude $h = 1\ \gamma$ at 300 km (vertical incidence) (after Akasofu)

2.4 Neutral Composition

Both neutral and ionic composition depend to a large extent upon direct perturbation of the region by solar corpuscles (photons, electrons, and protons) and on the macroscopic motions such as atmospheric circulation, vertical drift, diffusion, and mixing. Yet, there exist quasi-static periods in the diurnal cycle where the specification of number densities would aid in the understanding and prediction of atmospheric phenomena. Perhaps logically, number densities should be couched in terms of the perturbations, in the same manner that Jacchia has phrased the total density term. With the recent increase in knowledge of the solar spectrum and of the photo-ionization cross-sections, this task for the first time appears possible. This suggests a combination of the statistical (cross correlation function) treatment and the deterministic particle-particle interactions. Such a task is beyond the scope of this work.

Inspection of the literature on the subject of number densities reveals a considerable lack of integration. In Table 5, the results of Nicolet and Bates [19] are given. These are daytime densities, yet their totals agree very well with the mean density as given by Minzner (1959 ARDC Atmosphere). In view of the excellent work of Jacchia and the relation of this work to the delineation of the proper use of the Minzner model as a mean of day and night-time values, the Table requires considerable modification. A simple modification applicable to mid-day conditions is to retain the same relative densities, but to increase them by the factors

TABLE 5

Number Densities
(After Bates and Nicolet)

H(km)	n(O)	$n(O_3)$	$n(O_2)$	$n(N_2)$	n(N)	n(NO)	n(H)	Minuner Mean
70	$2x10^{11}$	$1x10^{9}$	$4x10^{14}$	$2x10^{15}$	---	---	---	$2.1x10^{15}$
80	$2x10^{11}$	$6x10^{7}$	$9x10^{13}$	$4x10^{14}$	---	---	---	$4.4x10^{14}$
90	$4x10^{11}$	$2x10^{6}$	$1x10^{13}$	$5x10^{13}$	---	---	---	$5.9x10^{13}$
100	$7x10^{11}$	$7x10^{4}$	$1x10^{12}$	$6x10^{12}$	$2x10^{8}$	$2x10^{6}$	10^{8}	$7.8x10^{12}$
150	$2x10^{10}$	---	$2x10^{9}$	$3x10^{10}$	$5x10^{7}$	10^{6}	10^{8}	$3.8x10^{10}$
200	$5x10^{9}$	---	$2x10^{8}$	$5x10^{9}$	$1x10^{7}$	10^{6}	10^{7}	$8.4x10^{9}$
250	$3x10^{9}$	---	$6x10^{7}$	$1x10^{9}$	---	---	10^{7}	$3.3x10^{9}$
300	$1x10^{9}$	---	$2x10^{7}$	$3x10^{8}$	$4x10^{6}$	$4x10^{5}$	10^{7}	$1.3x10^{9}$
400	$3x10^{8}$	---	$4x10^{5}$	$5x10^{6}$	$7x10^{5}$	$5x10^{4}$	10^{6}	$2.8x10^{8}$
600	$2x10^{7}$	---	---	$5x10^{4}$	---	---	10^{6}	$2.6x10^{7}$
800	$3x10^{6}$	---	---	---	---	---	10^{5}	---
1000	$4x10^{5}$	---	---	---	---	---	10^{5}	---

which are characteristic of the deviations between the Minzner and Jacchia models. Such a procedure was employed by Watanabe in generating Table 20. Number densities at night would require more fundamental changes because of the radical decrease in the solar perturbation.

Figure 8 is a plot combining the Bates and Nicolet results with some results given by Miller.[20] The latter are to be considered even more tentative.

The secular variations in composition may well be exemplified in the ozone content. Figure 9 and 10 give some idea of the scope of these variations.

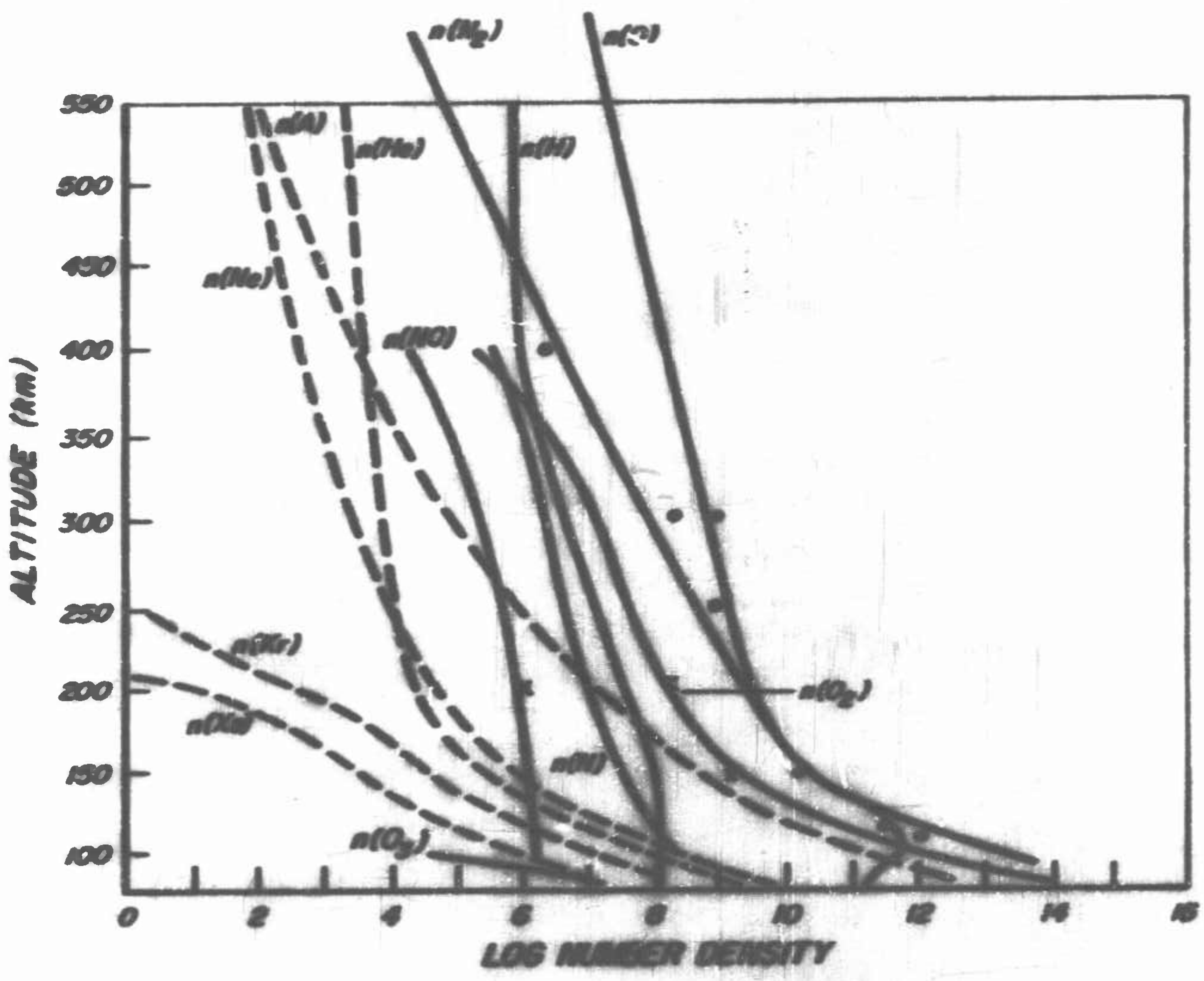

Figure 8. Atmospheric Composition Versus Altitude (solid lines Ref. 19) (dotted lines Ref. 20) (after Bates and Nicolet).

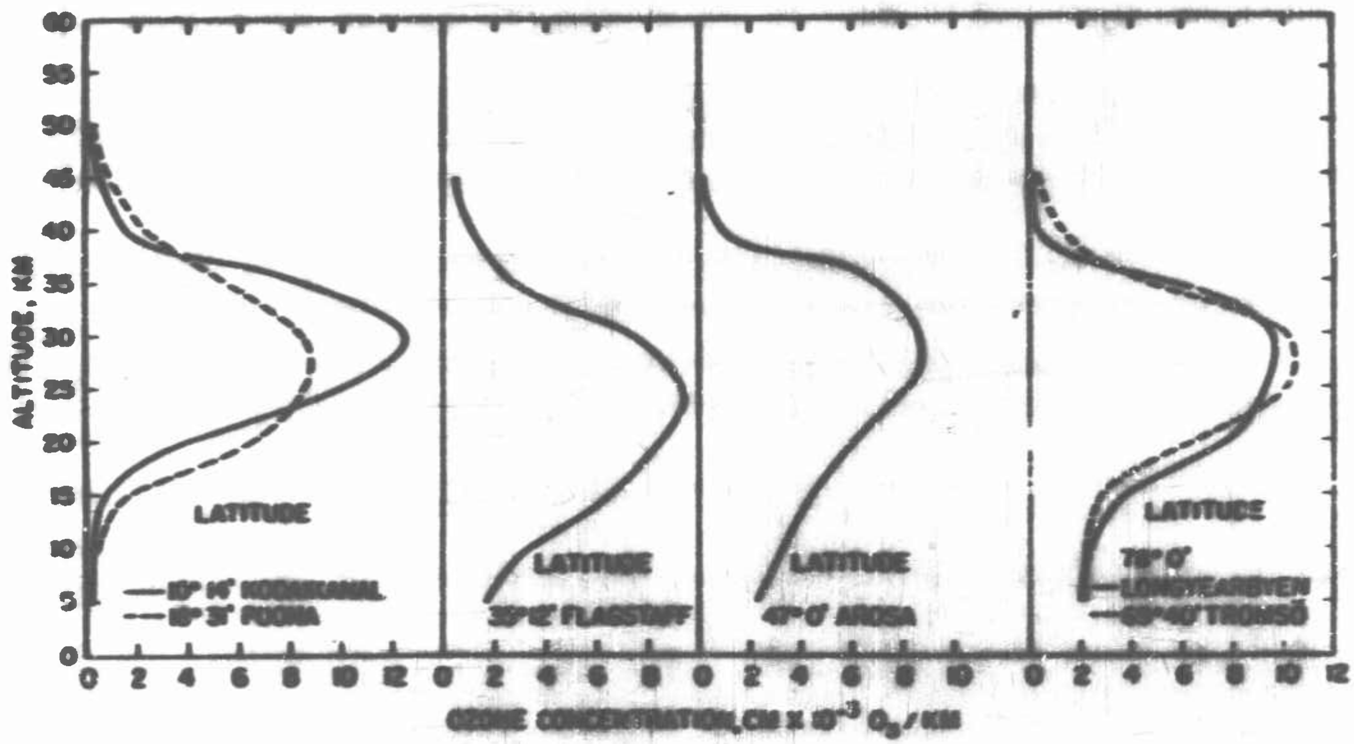

Figure 9a. Latitude Variation of Ozone Concentration

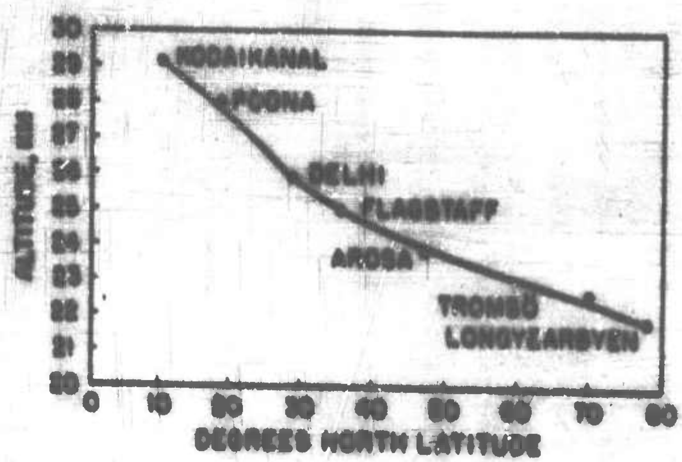

Figure 9b. Latitudinal Variation of Ozone Center of Gravity

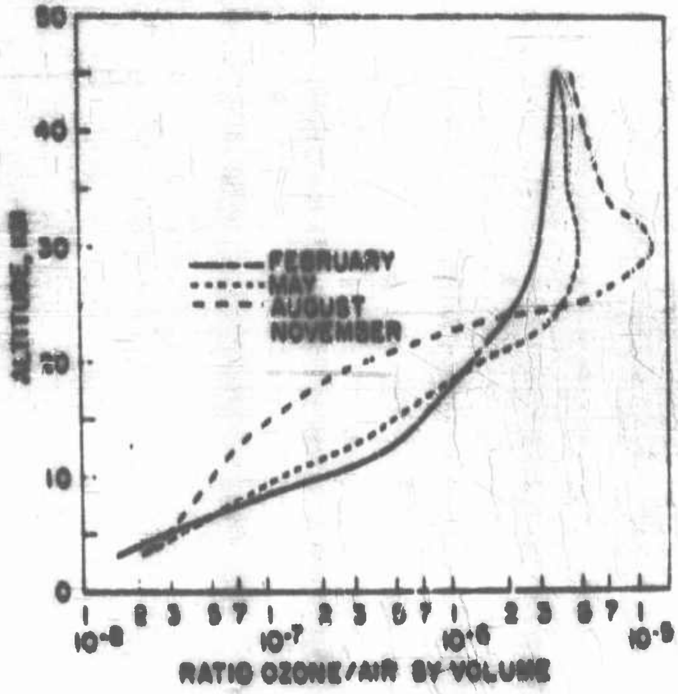

Figure 10a. Seasonal Variation of Ozone to Air Ratio at Flagstaff

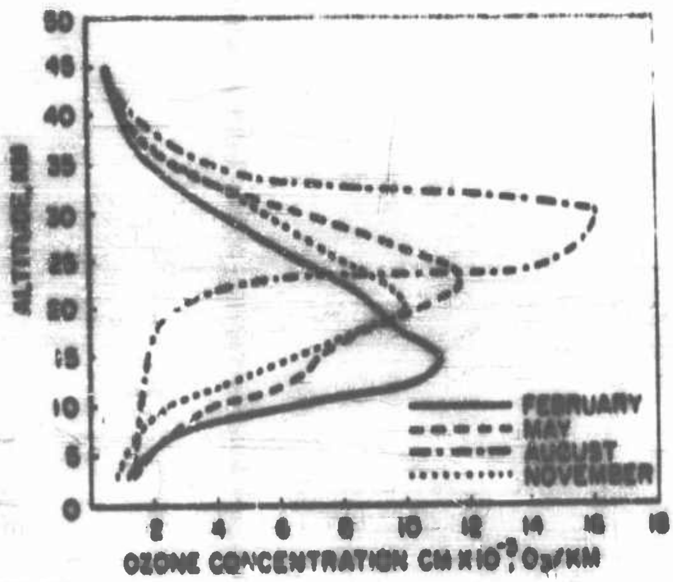

Figure 10b. Seasonal Variation of Ozone Concentration at Flagstaff

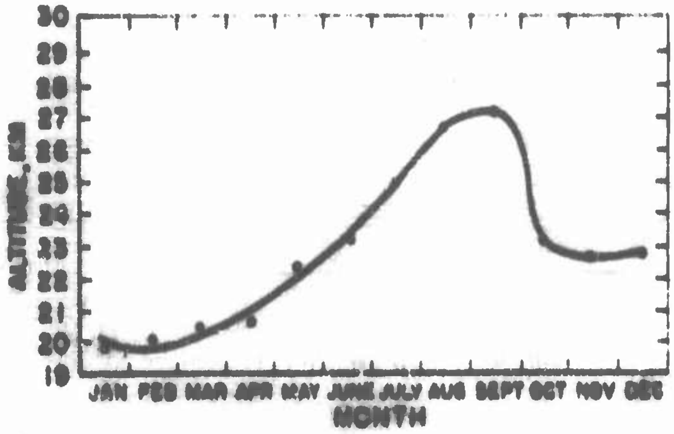

Figure 10c. Seasonal Variation of Ozone Center of Gravity at Flagstaff

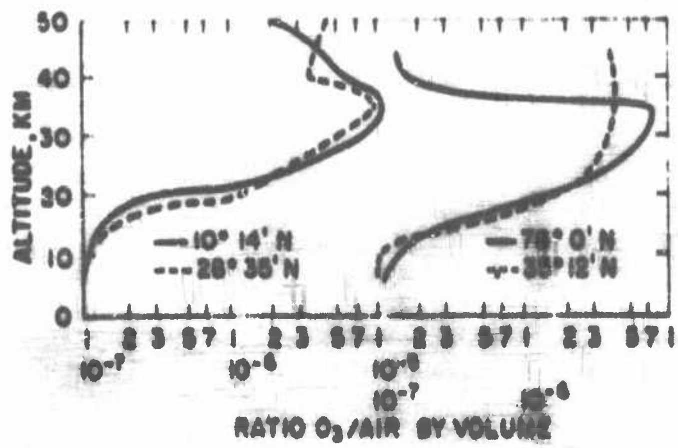

Figure 10d. Latitudinal Variation of Ozone to Air Ratio

2.5 Positive Ion Composition

The present status of the ion composition is similar to that of neutral composition - too few measurements have been made to date, and the composition may vary considerably with auroral or solar flare activity.

From rocket flights conducted in the United States, the following positive ions have been identified (N^+, O^+, N_2O^+, N_2^+, NO^+, O_2^+). In the E-region the results of the Fort Churchill flights (fig. 11) indicate that O_2^+, NO^+, and O^+ dominate the ion mass spectrum, constituting about 97% of the total. (See Figure 12 also)

The most striking feature of the ion densities in the region of 100 to 150 km is the preponderance of the NO^+ (density of the order of $3 \times 10^5/cm^3$). Other characteristics to be explained are the deficiency of N_2^+ and O^+, and the apparent diurnal effect (the ratio of the two dominent ions n (NO^+)/n (O_2^+) is larger during the day). This diurnal effect must be considered tentative in view of the possible contributions of seasonal and auroral effect (the measurements being made in different seasons). A detailed analysis of the problem of ion composition must take into consideration the neutral composition; the incident solar spectrum, the photo-ionization cross sections, the microscopic interactions of dissociative recombination, associative attachment, charge exchange, and atom-ion or atom-atom exchange, and perhaps the macroscopic processes of mixing and diffusion. Such an investigation is beyond the scope of this work.

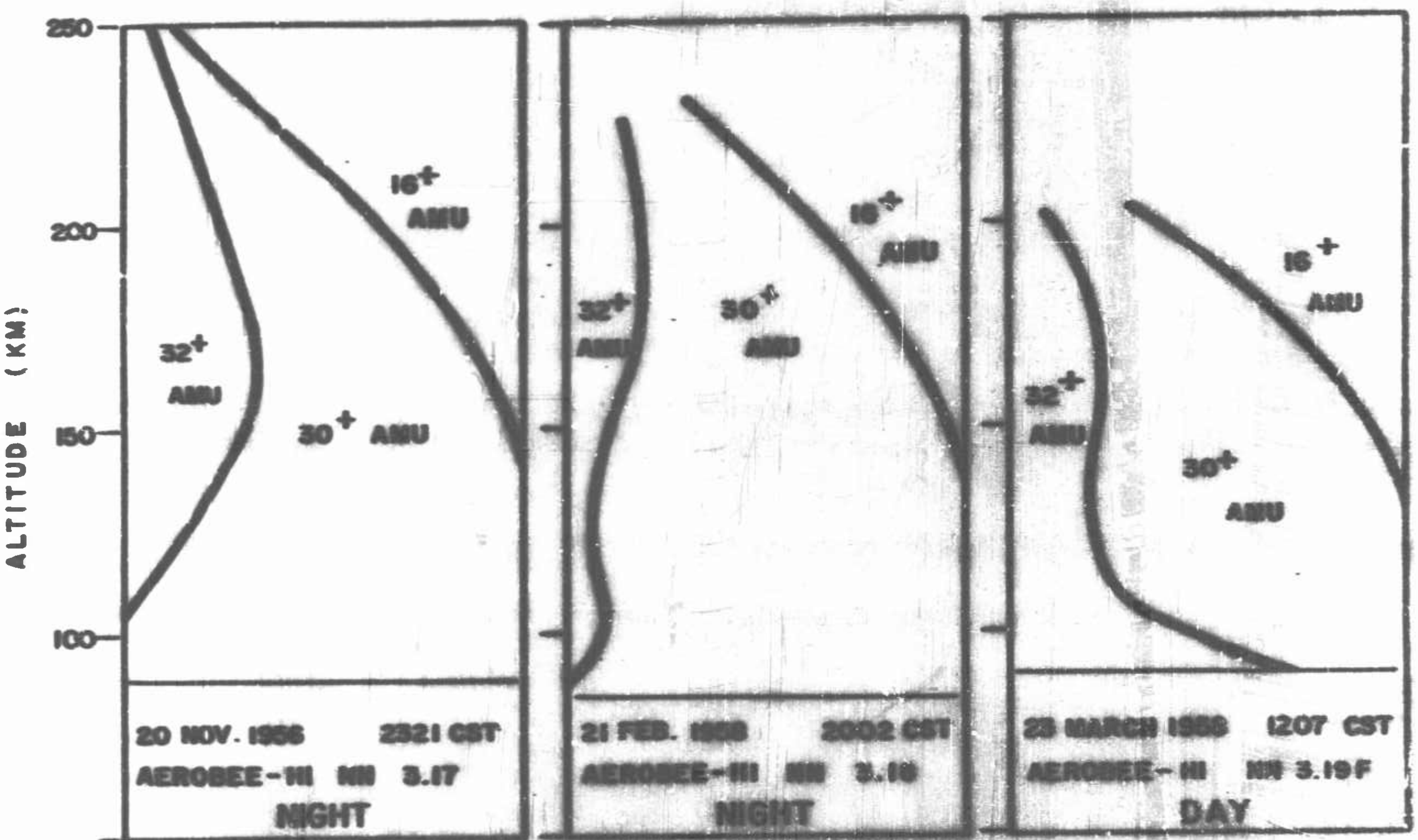

DISTRIBUTION OF THE MAJOR POSITIVE IONS ABOVE FORT CHURCHILL, CANADA

Figure 11

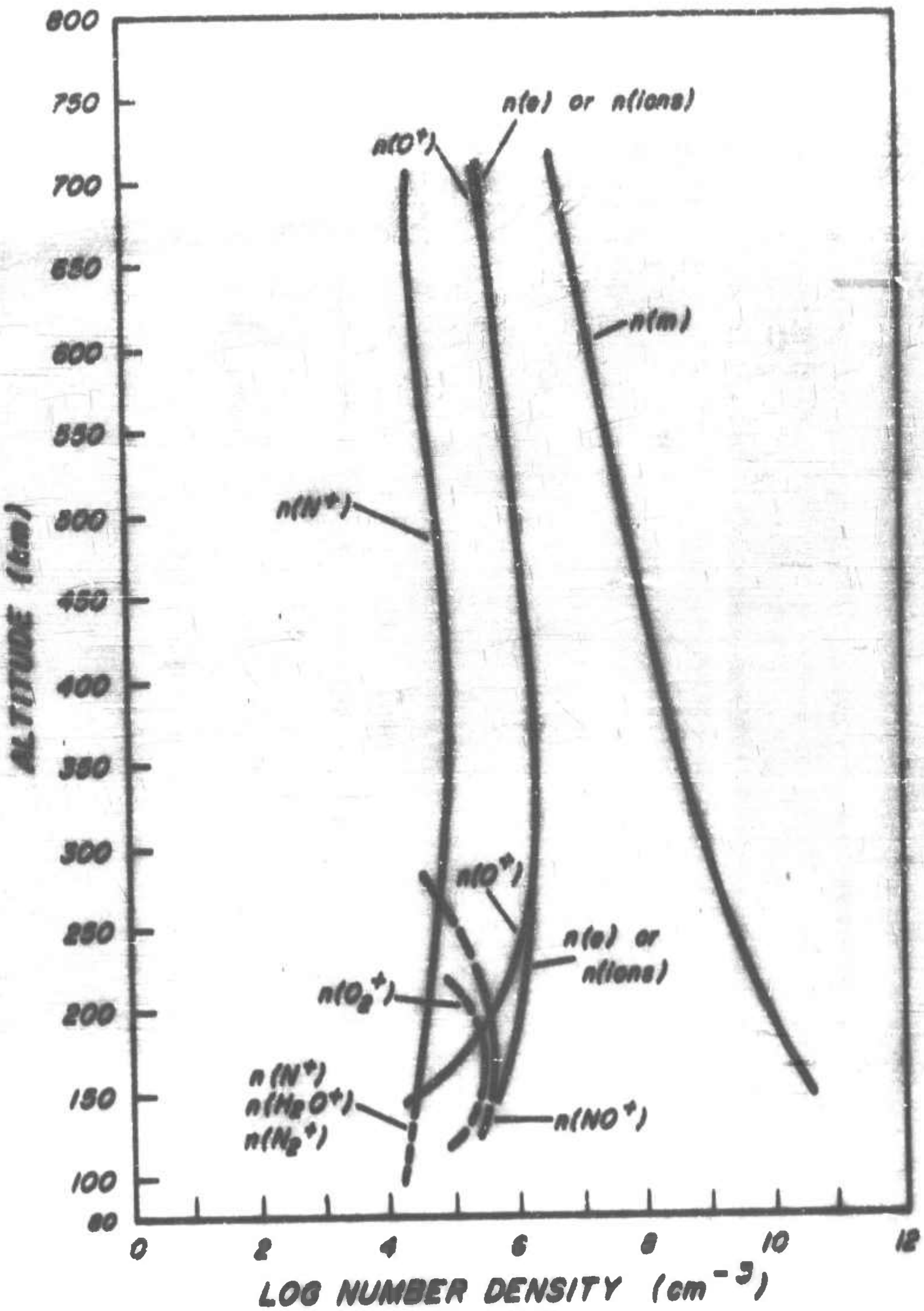

Figure 12. Positive Ion Concentration Versus Altitude

We shall take a quick look at the region of 100 km where typical densities are:

$n\,(N) = 2 \times 10^{8}\ cm^{-3}$

$n\,(N_2) = 6 \times 10^{12}\ cm^{-3}$

$n\,(O_2) = 1 \times 10^{12}\ cm^{-3}$

$n\,(O) = 7 \times 10^{11}\ cm^{-3}$

$n\,(NO) = 2 \times 10^{6}\ cm^{-3}$

$$\text{noon} \begin{cases} n\,(e) = 3 \times 10^{5}\ cm^{-3} \\ n\,(NO^+) = 3 \times 10^{5}\ cm^{-3} \end{cases}$$

$$\left[\frac{n(O_2^+)}{n(NO^+)}\right]_{night} \cong 0.5$$

$$n\,(N_2^+) \approx 10^{3}\ cm^{-3}$$

Bates has suggested that ion-atom-exchange may be a controlling factor. The rates of these reactions may be as high as 10^{-9} $cm^3\ sec^{-1}$ but the requirement of activation energy probably reduces the figure for ambient atmospheric conditions to the order of $10^{-12 \pm 1}$ $cm^3\ s^{-1}$. In considering the essential property of exothermicity of the reactions, only the ground state of the reacting species can realistically be considered. An inspection of the possible reactions (exothermicity but not rates) can be made with the aid of the potential well diagrams. For example, among the following reactions (4) and (5) are permissible, but reaction (6) is exothermic only when for reactants in particular elevated states.

$$N\,(^4S^o) + O_2^+\,(X^2\,\Pi_g) \longrightarrow NO^+(X^1\,\Sigma^+) + O(^3P) + 3.9\ ev. \qquad (4)$$

$$N_2(X^1\Sigma_q^+) + O^+(^4S^o) \longrightarrow NO^+(X^1\,\Sigma^+) + N\,(^4S^o) + 0.8\ ev. \qquad (5)$$

$$N_2^+(X^2\,\Sigma_g^+) + O(^3P) \longrightarrow NO^+(^3\Sigma^+) + N(^4S^o) - 1.7\ ev. \qquad (6)$$

One can obtain some idea of the role of these reactions by comparing them with say dissociative recombination. The rate of $(O_2^+ + e \rightarrow O' + O'')$ is of the order of 10^{-8} cm^3 s^{-1}, consequently, the rate of production of O at 100 km by this method is:

$$(10^5)\ (3 \times 10^5)\ (10^{-8}) = 6 \times 10^2\ cm^{-3}\ s^{-1} \qquad (7)$$

Reactions (4) give the representative figure for production of NO^+ and O as

$$(2 \times 10^8)\ (10^5)\ (10^{-12}) = 2 \times 10\ cm^{-3}\ s^{-1}$$

while reaction (5) for production of NO^+ and N yields

$$(6 \times 10^{12})\ (1 \times 10^4)(10^{-12}) = 6 \times 10^4\ cm^{-3}\ s^{-1}$$

Identical rate coefficients are taken for the ion-atom interchange reactions since the activation energy of the complexes $(N - O - O)^+$ and $(N - N - O)^+$ are unknown and neither complex suffers from obvious steric hindrance. Although these rates can only be considered as tentative, the values arrived at do point out the probable importance of these reactions.

In the F-region, both the US and the Russian rocket-borne mass spectrometers have identified O^+ as the dominant positive ion. The ratios of populations of N^+ to O^+ are given in table 7 for altitudes of 150 to 700 km.

TABLE 7

Height in Km.	Electron or ion density, cm^{-3}	Concentration of individual ions, cm^{-3} O^+	NO^+	O_2^+	N^+	H_2O^+	N_2^+	1959 ARDC model atmosphere molecules, cm^{-3}	Ratio of ions to unionized molecules
150	$5x10^5$	$3x10^4$	$3x10^5$	$2x10^5$	$< 2x10^4$			$3.8x10^{10}$	$1.3x10^{-5}$
200	$1x10^6$	$5x10^5$	$3x10^5$	$2x10^5$	$< 3x10^4$			$8.4x10^9$	$1.7x10^{-4}$
300	$1.5x10^6$	$1.5x10^6$	--	--	$6x10^4$	--	--	$1.3x10^9$	$1.2x10^{-3}$
400	$1.5x10^6$	$1.5x10^6$	--	--	$1x10^5$	--	--	$2.8x10^8$	$3.6x10^{-3}$
500	$1x10^6$	$1x10^6$	--	--	$6x10^4$	--	--	$7.3x10^7$	$1.4x10^{-2}$
600	$7x10^5$	$7x10^5$	--	--	$4x10^4$	--	--	$2.3x10^7$	$3.1x10^{-2}$
700	$5x10^5$	$5x10^5$	--	--	$4x10^4$	--	--	$8.4x10^6$	$6.0x10^{-2}$

2.6 Negative Ion Composition

One might anticipate on the basis of the published cross sections and mechanisms of electron attachment that the predominant negative ions existing in the D and E regions at night will be O_2^- and O^-. In the daytime, photo-detachment would be very effective in destroying these negative ion species. In spite of this, the only direct observation (Table 8) on negative ions was made during a day flight; (no negative ions were detected in the night flight).

Table 8

Species	Electron Affinity	"Mass"	%
NO_2^-	1.6	46	96.5
O_2^-	$.9 \mp .1$	32	1.6
?		29	0.2
?		22	1.0
O^-	1.465	16	0.7

If the fact that the probe detected negative ions only in the day flights can be attributed to some space charge accumulated by the carrier and not a perturbation of the environment, the measurement of a completely predominant negative ion specis as NO_2^- appears to have some basis of validity.

would be a rapid day time process at 100 km and above. The vertical detachment energy of O^- is known to be of the same order (1.465 ev), and because of its high electron affinity, exothermic charge transfer to another common atmospheric specie is improbable. O_2^- can be consumed with much greater ease if its vertical detachment energy is actually 0.15 ev (this value may refer to photo-detachment from the $4\Sigma_2^-$ state). O_2^- also participates in atom-ion and charge exchange ($O_2^- + O \rightarrow O^- + O_2 + .5$ ev) - the rate being of the order of $10^{-12}cm^3s^{-1}$.

3. Ionosphere

In discussing the ionization in the atmosphere, it is convenient to divide the first 1000 km of the atmosphere into two regions, with the altitude of demarcation orbit roughly set at 60 km. (This is slightly lower than the boundary set by the competitive processes of mixing and diffusion (see Figure 1 .)) The upper region is characterized by the presence of free electrons which makes it susceptible to investigation by radio-frequency sounding while at the lower altitudes negative ions formed from attachment of electrons to molecular oxygen predominate. The regions may also be differentiated on the basis of ionising agent. The lower region is principally ionised by cosmic rays whereas the normal ionosphere is the result of photoionization by solar electromagnetic radiation at energies equivalent to and less than Lyman-α . Since the sources of ionization are distinct, the two regions also differ in temporal and spatial variations (both regular and abnormal).

3.1 Atmospheric Parameters (0-60 km)

3.1.1 Ion Equilibrium in the Atmosphere

The concentration of ions in thisregion of the atmosphere is determined by an equilibrium between processes creating ions and those removing them.

The four basic equations for small ions (positive n_1, negative n_2)

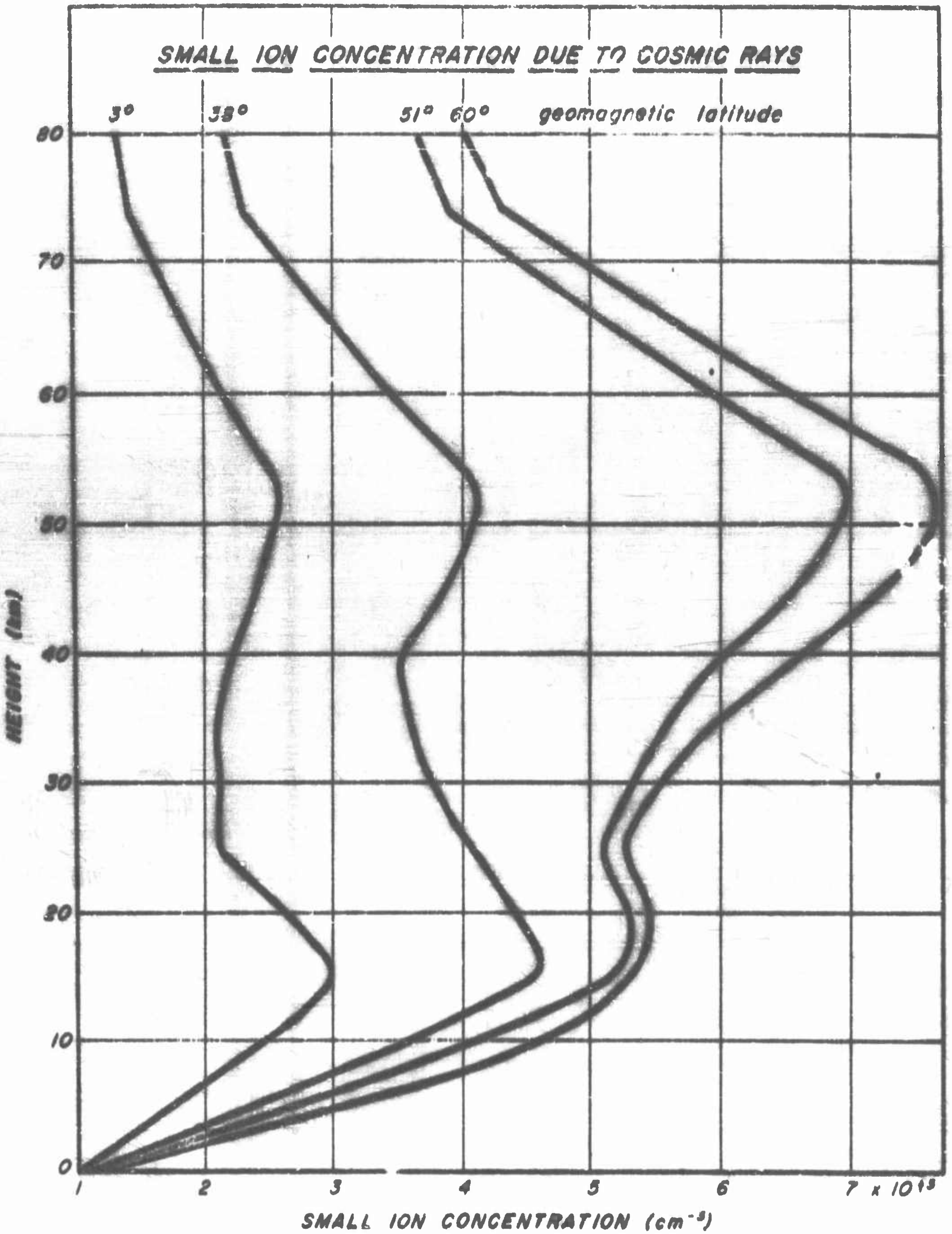

SMALL ION CONCENTRATION DUE TO COSMIC RAYS
3°
38°
51°
60°
geomagnetic latitude
80
70
60
50
40
30
20
10
0
HEIGHT (km)
1
2
3
4
5
6
7 x 10¹³
SMALL ION CONCENTRATION (cm⁻³)

Figure 13

and large ions (positive N_1, negative N_2) are

$$\frac{dn_1}{dt} = q - \alpha n_1 n_2 - \beta_{12} n_1 N_2 - \beta_{10} n_1 N_o \quad (8)$$

$$\frac{dn_2}{dt} = q - \alpha n_1 n_2 - \beta_{21} n_2 N_1 - \beta_{20} n_2 N_o \quad (9)$$

$$\frac{dN_1}{dt} = \beta_{10} n_1 N_o - \beta_{21} n_2 N_1 - \gamma N_1 N_2 \quad (10)$$

$$\frac{dN_2}{dt} = \beta_{20} n_2 N_o - \beta_{12} n_1 N_2 - \gamma N_1 N_2 \quad (11)$$

where q is the rate of production of small ions

α is the recombination coefficient for small ions

the β's are the attachment coefficients between small ions and nuclei

γ is the combination coefficient for large ions

N_o is the concentration of uncharged nuclei.

Unless the analysis is concerned specifically with the ratios n_1/n_2 and N_1/N_2, it is usual not to distinguish the signs of the ions, and n is used for small ions (of each sign) and N for large ions (of each sign). This also implies the assumption that $\beta_{12} = \beta_{21}$ and $\beta_{10} = \beta_{20}$. Finally, it is generally assumed that γ is small enough that the term $\gamma N_1 N_2$ can be neglected. The four equations then reduce to

$$\frac{dn}{dt} = q - \alpha n^2 - \beta_{12}\, n\, N - \beta_{10} n\, N_o \quad (12)$$

$$\frac{dN}{dt} = \beta_{10}\, n\, N_o - \beta_{12}\, n\, N \quad (13)$$

Under equilibrium conditions this last equation gives the ratio of charged to uncharged nuclei

$$N/N_o = \beta_{10} / \beta_{12} \qquad (14)$$

which may be used to determine the total nucleus concentration by measuring the concentration of large ions. The small ion equilibrium equation becomes

$$q = \alpha n^2 + 2 \beta_{12} n N \qquad (15)$$

This formula has been verified in the atmosphere. In Table 9 representative values of these relevant quantities are given for an altitude of 1 km for a non-industrial region over land, for a mid-ocean area and for the idealized case of no nuclei, probably typical of polar regions at this altitude.

TABLE 9: Average Properties at 1000 m

	λ_+ esu	$n_+ cm^{-3}$	$N_+ cm^{-3}$	r_o cm	$\beta_{12} cm^3 sec^{-1}$	$q\ cm^{-3} sec^{-1}$
Land	1.23×10^{-4}	540	1250	2×10^{-6}	3.2×10^{-6}	4.8
Ocean	1.05×10^{-4}	460	315	8×10^{-6}	5.3×10^{-6}	2.0
No nuclei	2.4×10^{-4}	1050	0	--		1.8

3.1.2 Exchange Layer

The region of the atmosphere from the ground up to a few km is characterized by a conductivity smaller than that deduced from cosmic ray measurements. The upper limit of the region is often sharply defined and varies with meteorological conditions from 1000 to 10,000 feet with an average of 6000 feet.

In this region the ionization rate is augmented by terrestrial sources and the rate of destruction of small ions increased due to combination with charged and uncharged Aitken nuclei. The net result is a reduction in the concentration of small ions to 20 to 30 per cent of the value computed from cosmic ray ionization, the lower values being found near sources of atmospheric pollution.

Whereas above the exchange layer the atmospheric conductivity shows negligible variation with time, a large variation is found within the layer. The release of nuclei into the atmosphere and the turbulent and convective mixing in the exchange layer all show a marked diurnal variation which results in a corresponding variation of conductivity. There is, in addition to this more or less regular change, an irregular variation in conductivity corresponding to air-mass changes.

3.1.3 Small Ion Concentration

Above the exchange layer and up to a height of about 60 km, the concentration of small ions is found to be given by

$$q = \alpha n^2 \tag{16}$$

where q is the rate of production by cosmic rays and α is the recombination coefficient for small ions. Since q is a function of geomagnetic latitude as well as height, the variation of n with height is also a function of geomagnetic latitude. Values of n computed for the four geomagnetic latitudes 3°, 38°, 51° and 60° are shown in Figure 13.

Below about 3 km the occurrence of Aitken nuclei and terrestrial sources of radioactive ionization reduce the conductivity below the values given.

3.1.4 Recombination Coefficient for Small Ions

The recombination coefficient for small ions in air is a function of temperature and pressure. Over the pressure range 760 mm Hg down to 10^{-2} mm Hg (0 to 75 km altitude) the coefficient is satisfactorily given by Thompson's expression:

$$\alpha = 1.73 \times 10^{-5} \left(\frac{273}{T}\right)^{3/2} \left(\frac{1}{M}\right)^{\frac{1}{2}} f\,(x) \qquad (17)$$

where T is the temperature (degrees Kelvin)

M is the mean molecular weight of the ions

x is the parameter $6.81 \left(\frac{273}{T}\right)^{2} \left(\frac{P}{760}\right) \left(\frac{L_A}{L}\right)$

in which P is the pressure (mm Hg) and L_A/L is the ratio at NTP of the mean free path of a molecule to that of an ion, and the function

$$f\,(x) = 1 - \frac{4}{x^4} \left[1 - (x + 1)\, e^{-x}\right]^2 \qquad (18)$$

is given in Table 10.

Values of α, assuming M = 85 a.m.u. and $L_A/L = 3$, for the 1959 ARDC Model atmosphere are given in Figure 14 for the range 0 to 80 km. The sea level value for this model is $\alpha = 1.60 \times 10^{-6}$ $cm^3 sec^{-1}$.

For heights greater than 30 km, the function f (x) may be

x	0	1	2	3	4	5	6	7	8	9
0.03	[illegible]	0.04046	[illegible]	[illegible]	[illegible]	[illegible]	[illegible]	[illegible]	[illegible]	[illegible]
0.04	[illegible]	[illegible]	[illegible]	[illegible]	[illegible]	[illegible]	[illegible]	[illegible]	0.05167	[illegible]
0.05	[illegible]	[illegible]	[illegible]	[illegible]	[illegible]	[illegible]	0.07279	[illegible]	0.07425	[illegible]
0.06	[illegible]	0.07792	[illegible]	[illegible]	[illegible]	[illegible]	[illegible]	[illegible]	[illegible]	0.08765
0.07	[illegible]	0.09007	[illegible]	[illegible]	[illegible]	[illegible]	[illegible]	[illegible]	[illegible]	0.09896
0.08	[illegible]	0.1030	[illegible]	0.1046	[illegible]	[illegible]	[illegible]	[illegible]	0.1103	0.1115
0.09	0.1117	[illegible]	[illegible]	[illegible]	[illegible]	[illegible]	[illegible]	[illegible]	0.1220	0.1232
0.1	[illegible]	[illegible]	[illegible]	[illegible]	[illegible]	[illegible]	[illegible]	0.2015	0.2119	0.2222
0.2	[illegible]	0.2423	[illegible]	[illegible]	[illegible]	[illegible]	[illegible]	0.2954	0.3085	0.3175
0.3	[illegible]	[illegible]	[illegible]	[illegible]	[illegible]	[illegible]	[illegible]	[illegible]	[illegible]	[illegible]
0.4	[illegible]	[illegible]	[illegible]	[illegible]	[illegible]	0.4449	0.4519	[illegible]	[illegible]	0.4726
0.5	[illegible]	[illegible]	[illegible]	[illegible]	[illegible]	0.5114	0.5175	[illegible]	0.5295	[illegible]
0.6	[illegible]	0.5471	[illegible]	[illegible]	[illegible]	[illegible]	[illegible]	[illegible]	0.5953	[illegible]
0.7	[illegible]	[illegible]	[illegible]	[illegible]	[illegible]	[illegible]	[illegible]	0.6274	[illegible]	[illegible]
0.8	[illegible]	0.6474	0.6527	[illegible]	[illegible]	[illegible]	[illegible]	0.6735	0.6766	[illegible]
0.9	[illegible]	0.6983	[illegible]	[illegible]	[illegible]	[illegible]	[illegible]	0.7103	0.7138	0.7173
1.0	[illegible]	0.7201	0.7274	0.7297	[illegible]	0.7371	[illegible]	0.7434	0.7465	[illegible]
1.1	[illegible]	0.7555	[illegible]	[illegible]	[illegible]	[illegible]	[illegible]	0.7724	0.7751	0.7778
1.2	[illegible]	[illegible]	[illegible]	[illegible]	[illegible]	[illegible]	[illegible]	[illegible]	0.8003	[illegible]
1.3	[illegible]	0.8072	[illegible]	[illegible]	[illegible]	0.8161	0.8182	0.8203	0.8224	[illegible]
1.4	[illegible]	0.8285	0.8305	[illegible]	[illegible]	[illegible]	0.8382	0.8401	0.8419	[illegible]
1.5	[illegible]	[illegible]	[illegible]	[illegible]	[illegible]	[illegible]	[illegible]	0.8574	0.8591	[illegible]
1.6	[illegible]	[illegible]	[illegible]	[illegible]	[illegible]	[illegible]	0.8713	[illegible]	0.8742	[illegible]
1.7	[illegible]	0.8784	[illegible]	[illegible]	[illegible]	[illegible]	[illegible]	[illegible]	0.8875	[illegible]
1.8	[illegible]	0.8913	0.8925	[illegible]	[illegible]	[illegible]	0.8971	[illegible]	[illegible]	[illegible]
1.9	[illegible]	0.9027	0.9037	[illegible]	[illegible]	[illegible]	0.9079	[illegible]	[illegible]	[illegible]
2.0	0.9118	0.9127	0.9137	0.9146	0.9156	0.9165	0.9174	0.9182	0.9191	0.9200
2.1	[illegible]	0.9217	0.9225	[illegible]	[illegible]	[illegible]	0.9258	[illegible]	0.9273	0.9281
2.2	[illegible]	0.9296	0.9304	0.9311	0.9318	0.9325	0.9332	0.9339	0.9346	[illegible]
2.3	[illegible]	0.9367	0.9373	[illegible]	[illegible]	[illegible]	[illegible]	0.9405	0.9411	0.9417
2.4	[illegible]	0.9429	0.9435	0.9441	0.9447	0.9453	0.9458	0.9464	0.9469	0.9475

Table 10. Probability Function f(x)

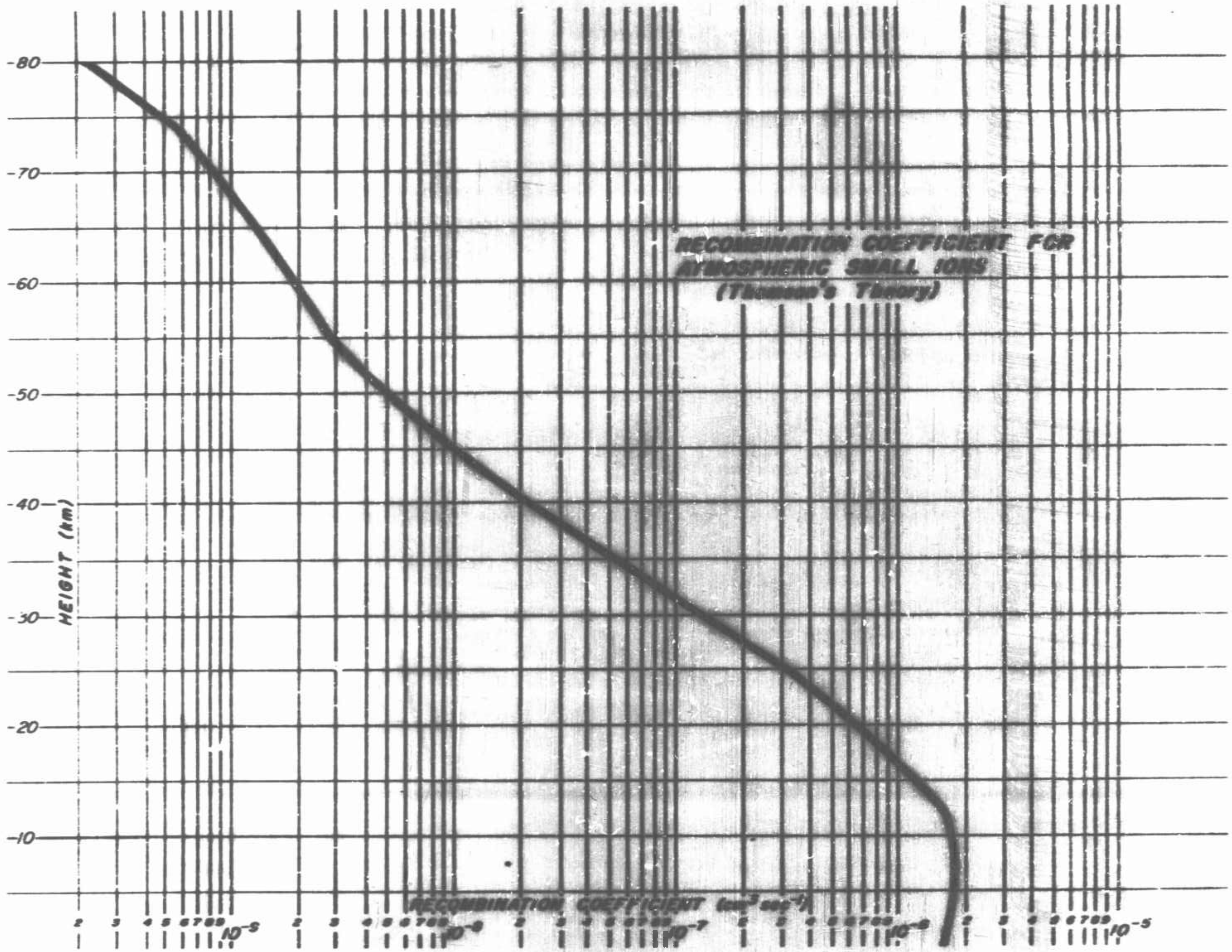
RECOMBINATION COEFFICIENT FOR
ATMOSPHERIC SMALL IONS
(Thomson's Theory)
HEIGHT (km)
-80
-70
-60
-50
-40
-30
-20
-10
RECOMBINATION COEFFICIENT (cm³ sec⁻¹)

Figure 14

closely approximated by f (x) = 4 x/3 $[x < 0.03]$

and the formula for α becomes

$$\alpha = 6.16 \times 10^{-6} \left(\frac{273}{T}\right)^{7/2} \left(\frac{P}{760}\right) \qquad [H > 30 \text{ km}] \qquad (19)$$

3.1.3 Bricard's Formulae for Attachment Coefficients[21]

Four attachment coefficients are defined as follows:

β'_{1p} between positive small ions and nuclei having p positive charges

β'_{2p} between negative small ions and nuclei having p positive charges

β''_{1p} between positive small ions and nuclei having p negative charges

β''_{2p} between negative small ions and nuclei having p negative charges

The values are given by

$$\beta'_{1p} = \frac{4\pi D'a}{I(\eta, p)} \qquad \beta''_{1p} = \frac{4\pi D'a}{I(\eta, -p)} \qquad (20)$$

$$\beta'_{2p} = \frac{4\pi D''a}{I(\eta, -p)} \qquad \beta''_{2p} = \frac{4\pi D''a}{I(\eta, p)}$$

where $I(\eta, p) = \int_1^\infty \frac{1}{x^2} \exp\left[\eta\left(\frac{p}{x} - \frac{1}{2x^2(x^2-1)}\right)\right] dx$

and D' and D" are the diffusion coefficients of positive and negative small ions:

$$D' = \left[\frac{760}{P}\left(\frac{T}{288}\right)^2\right] 0.032 \qquad D'' = \left[\frac{760}{P}\left(\frac{T}{288}\right)^2\right] 0.035 \qquad (21)$$

where P is pressure in mm Hg and T is the absolute temperature and a is the radius of the nuclei.

$$\eta = eK'/D'a = eK''/D''a = (6.18 \times 10^{-6}/a)\,(288/T) \qquad (22)$$

where K' and K" are the mobilities of positive and negative small ions and e is the electronic charge.

In the practical application to ion equilibrium in the atmosphere, it is usual to assume D' = D" and K' = K". In this case two coefficients are important:

β_{12} (= β_{21}) for attachment of small ions with large ions of opposite sign (p = -1), and

β_{10} (= β_{20}) for attachment of small ions with uncharged nuclei (p = 0).

Thus

$$\beta_{12} = \frac{4\pi Da}{I(\eta, -1)} \qquad (23)$$

$$\beta_{10} = \frac{4\pi Da}{I(\eta, 0)}$$

where D is the mean of D' and D". Values of I as a function of η are given in Figure 15 for integral values of p between -4 and +3. The variation of β_{12} and β_{10} with size is shown in Figure 16 for sea level (P = 760 mm Hg; T = 288°K) and 10,000 ft (P = 523 mm Hg; T = 268°K).

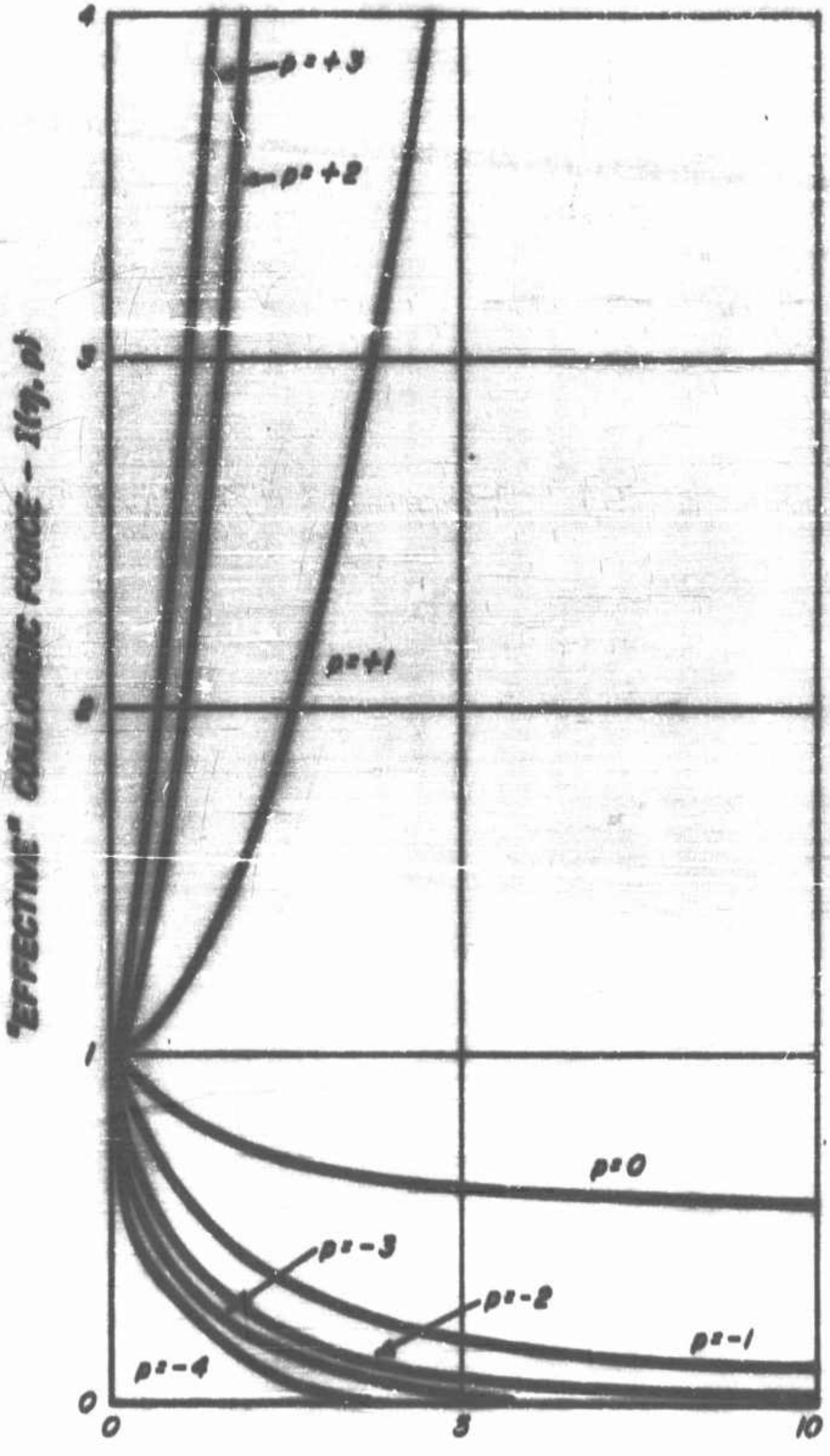

Figure 15. Effective Coulombic Force Versus η

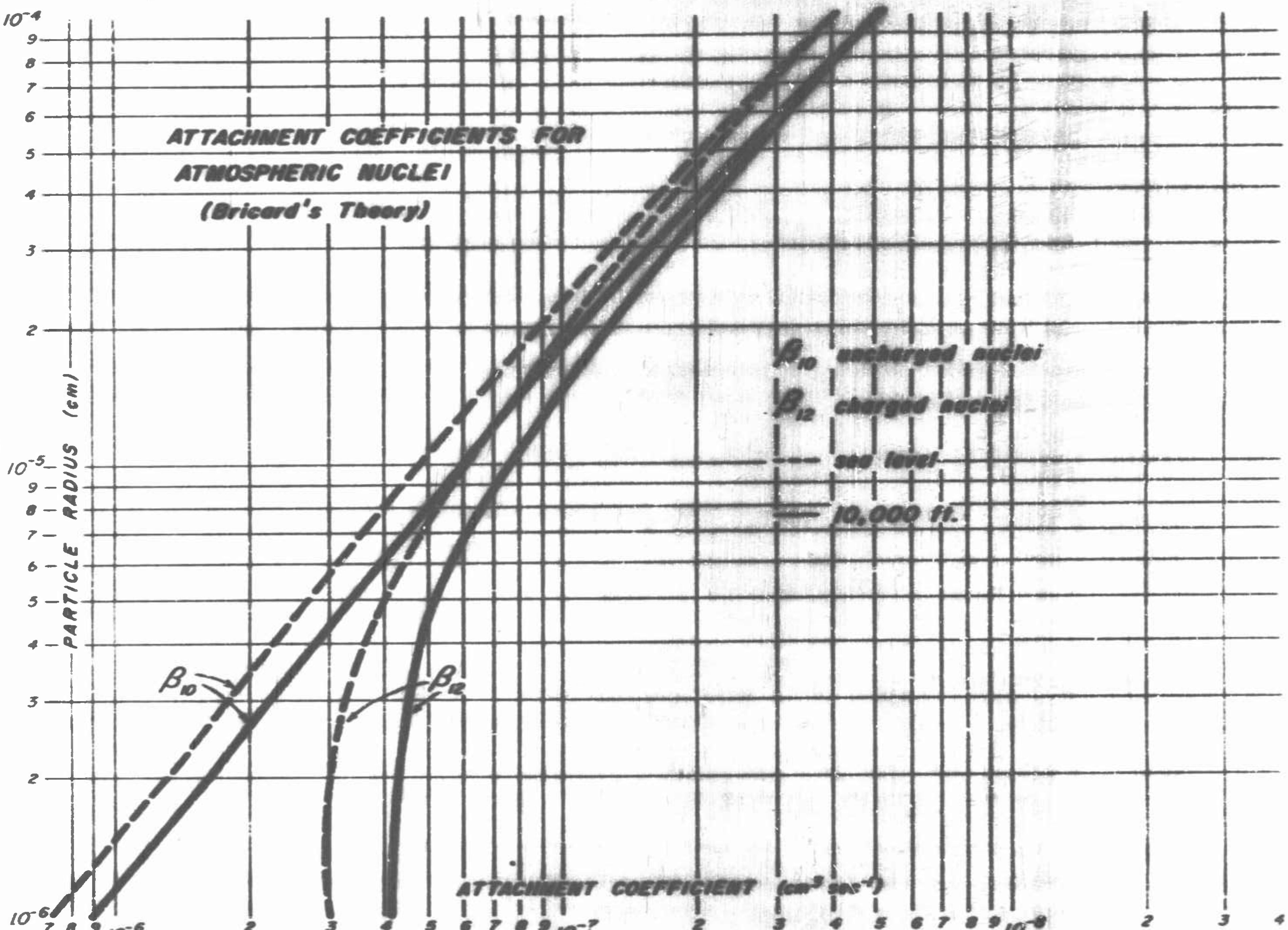
ATTACHMENT COEFFICIENTS FOR
ATMOSPHERIC NUCLEI
(Bricard's Theory)
β_{10} uncharged nuclei
β_{12} charged nuclei
sea level
10,000 ft.
β_{10}
β_{12}
PARTICLE RADIUS (cm)
ATTACHMENT COEFFICIENT (cm^3 sec^{-1})
10^{-4}
10^{-5}
10^{-6}
10^{-7}
10^{-8}

Figure 16

3.1.6 Ionic Mobility

(a) Small Ions. The mobility of small ions at room temperature (288°K) and 760 mm Hg are

$k_+ = 1.4\ cm^2 sec^{-1}\ volt^{-1}$

$k_- = 1.7\ cm^2 sec^{-1}\ volt^{-1}$

The mobility is inversely proportional to density; hence, the value at any height may be easily computed using the factor (ρ / ρ_o) given in the ARDC 1959 Model Atmosphere (see Figure 17) and Table 3).

(b) Large Ions. The mobility of large ions in the lowest few km of the atmosphere is adequately given by the Stokes-Millikan relation:

$$k = e / (6 \pi \eta a) \tag{24}$$

where e is the electronic charge

η is the viscosity of air

a is the radius of the ion.

The atmospheric large ions are assumed to be singly charged. Values typical of conditions over land and ocean are

	(a)	(k)
Land	2×10^{-6} cm	$0.0024\ cm^2 sec^{-1}\ volt^{-1}$
Ocean	8×10^{-6} cm	$0.0006\ cm^2 sec^{-1}\ volt^{-1}$

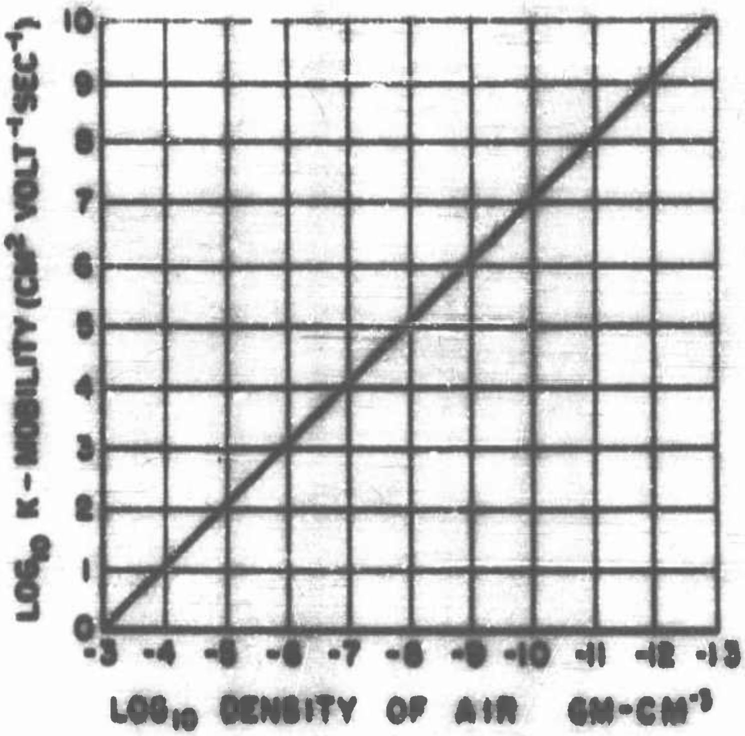

Figure 17. Mobility of Small Ions of One Sign Versus Atmospheric Density

3.1.7 Electrical Conductivity

The conductivity due to ions of mobility $k_{\pm}$ is

$$\lambda_{\pm} = n_{\pm}\, e\, k_{\pm} \tag{25}$$

where $n_{\pm}$ is the concentration of ions and e their charge. In the atmosphere the contribution due to large ions is negligible and only small ions are normally considered.

Owing to the small change in $n_{\pm}$ with height the variation in conductivity is mainly determined by the mobility which varies inversely as density. Hence the conductivity increases rapidly with height in the atmosphere as shown in Figure 18. The total conductivity λ is plotted where

$$\lambda = \lambda_{+} + \lambda_{-} = n\, e\, (k_{+} + k_{-}) \tag{26}$$

3.2 The D-Region

The D-region (approximately 60 to 85 km) has electron-ion pair production processes which are to some extent distinct from those characteristic of the main ionosphere. The region is of particular interest for, because of its relatively high electron collision frequencies, it is the seat of absorption or even blackout of ionospherically propagated radio waves. Solar radiation reaching this altitude regime (see Figure 19) is basically limited to X-rays below 10 A, Lyman-α (λ 1215.7), and photons with wavelengths greater than 1800 A.

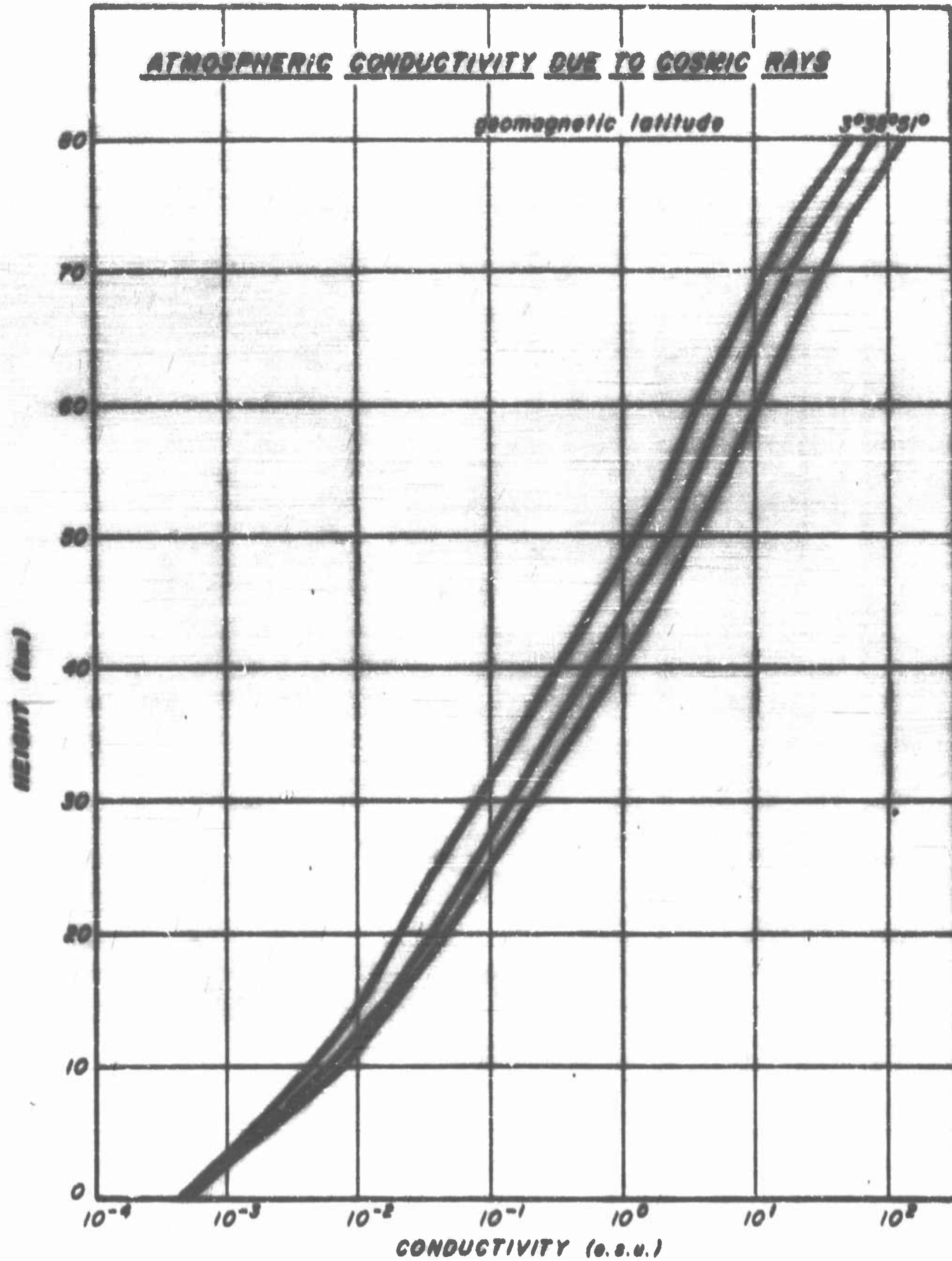
ATMOSPHERIC CONDUCTIVITY DUE TO COSMIC RAYS
geomagnetic latitude
3° 38° 51°
HEIGHT (km)
80
70
60
50
40
30
20
10
0
10^-4
10^-3
10^-2
10^-1
10^0
10^1
10^2
CONDUCTIVITY (e.s.u.)

Figure 18

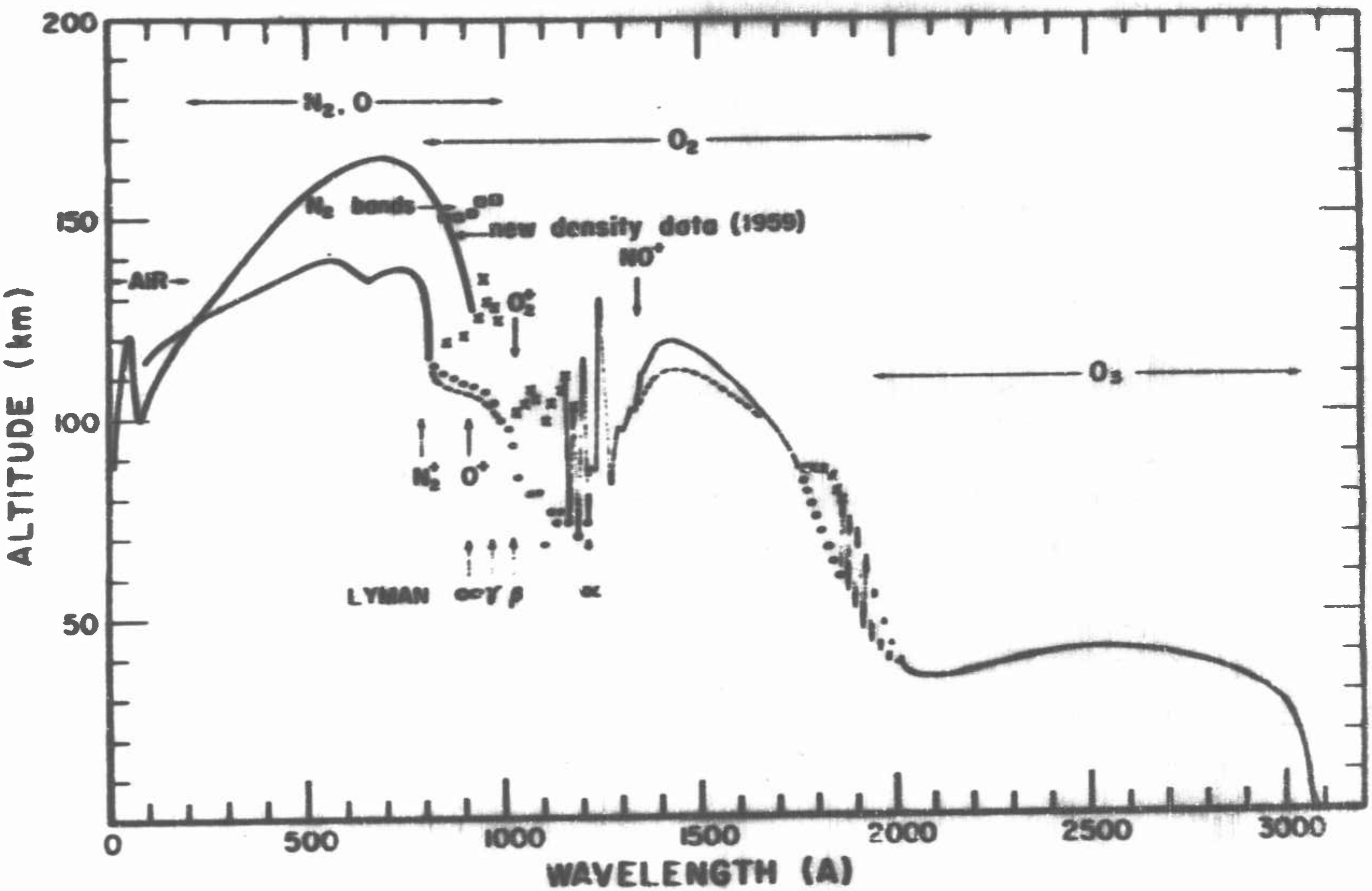

Figure 19. Altitude at which Solar Radiation Drops to 1/e of its Value (for Vertical Incidence)

In addition to Lyman-α there is some contribution of photons with energies lying between the Schumann-Runge bands of O_2 (1800-2000 A) and in the narrow atmospheric windows at λ 1216, λ 1187, λ 1167, λ 1157, λ 1143, and λ 1108. For the latter individual wavelengths, unit optical depth of 10^{20} molecules cm^{-2} $column^{-1}$ is normally attained for vertical incidence at about an altitude of 75 km.

Whereas the accepted solar flux in the 10 to 1000 A range has been radically modified by the recent observation of Tousey[22] and of Hinteregger[23], the three spectral areas which are the principal sources of the D-region as reported by Nicolet and Aiken[24] have remained essentially unaltered. Therefore the accepted dynamics (outside of some reservations in regard to composition), is still very nearly that given by these investigators. The following brief summary of their material is included for completeness of presentation.

3.2.1 Composition

X-rays are capable of ionising all the atmospheric species (mostly molecular nitrogen and oxygen at these altitudes); but Lyman-alpha can only ionise nitric oxide, and λ 1800 the low concentration metallic atoms of sodium and calcium. Therefore, the composition of the "trace" substances are particularly important to the dynamics of the ionisation.

Table 11 is Nicolet's version of the height variations of the particle densities of the main atmospheric constituents between 50 and

Atmospheric Data between 50 and 90 Km

Altitude, km	Temperature, °K	$n(O_2)$, cm^{-3}	$n(NO)$, cm^{-3}	$n(N_2)$,* cm^{-3}	$n(M)$, cm^{-3}
50	274	4.93 × 10[illegible]	2.35 × 10[illegible]	1.83 × 10[illegible]	1.9 × 10[illegible]
52.5	274	3.63	1.73	1.35	1.4
55	271	2.65	1.28	9.97 × 10[illegible]	1.0
57.5	263	2.04	9.72 × 10[illegible]	7.58	7.6 × 10[illegible]
60	253	1.53	7.31	5.70	5.5
62.5	242	1.14	5.43	4.24	3.9
65	232	8.35 × 10[illegible]	3.98	3.11	2.8
67.5	221	6.05	2.80	2.25	1.9
70	210	4.31	2.06	1.61	1.3
72.5	207	2.94	1.40	1.09	8.7 × 10[illegible]
75	203	1.90	9.48 × 10[illegible]	7.40 × 10[illegible]	5.3
77.5	200	1.26	6.23	4.96	3.8
80	197	8.13 × 10[illegible]	4.28	3.24	2.5
82.5	193	5.33	2.88	2.21	1.6
85	190	3.50	1.88	1.45	1.1
87.5	191	2.45	1.83	9.24 × 10[illegible]	6.9 × 10[illegible]
90	192	1.59 × 10[illegible]	1.20 × 10[illegible]	5.93 × 10[illegible]	4.5 × 10[illegible]

* $n(N_2)$ = 0.7808 of the total concentration $n(M)$.

Table 11 (after Nicolet and Aikin)

90 km. Also included are the absolute temperatures and the total number of particles in a cm^2 column $[n(M)H]$. The total densities agree reasonably well with those quoted previously. In regard to the NO concentration which is important in ionization by Lyman-α, the concentration is probably too low to be measured reliably. Nicolet has obtained an estimate of the concentration by inspection of the production and dissipation processes involved. From the data of Kistiakowsky and Volpi[25], the rate coefficient of the reaction ($N + O_2 \rightarrow NO + O$) is $1.5 \times 10^{-13} T^{\frac{1}{2}} \exp(-6200/RT)$ and the rate of the probable dissipative reaction of NO (as suggested by Nicolet, $N + NO \rightarrow N_2 + O$) is $1.5 \times 10^{-11} T^{\frac{1}{2}}$. Therefore, the NO concentration is determined by the relation:

$$n(NO) = 10^{-2}\, n\,(O_2) \exp\,(-6200/RT) \qquad (27)$$

with the proviso "that the number of nitrogen atoms are sufficiently numerous". The condition, of course, points up the tentative nature of the analysis.

3.2.2 Ionization

Nicolet and Aiken[24] discuss some aspects of the ionization mechanisms which contribute to the D-layer formation outside of the auroral zones where solar protons and electrons can be the controlling feature. The details of energy deposition of cosmic rays and solar corpuscles are discussed in Cosmic Rays and Geomagnetism[26] and in Energy Loss Processes of Solar Corpuscles in Air[27], both by Nawrocki and Papa. Nicolet and Aiken give the following rough estimate of the geomagnetic latitude effect. The ionization rate (cosmic rays) at altitudes above 40 km is related to the geomagnetic latitude ϕ by

$$q(\phi) = q_o(\phi)\,\frac{n(z)}{n_o} \quad cm^{-3}sec^{-1} \tag{28}$$

where n_o is taken to be 2.5×10^{19} cm^{-3}, and n is the molecular concentration at the altitude (z). For a representative case, these investigators conclude that there is a factor of approximately 10 in going from the magnetic equator ($\phi = 0°$) to the magnetic latitude $\phi = 60°$. Their further assertion that the electron density varies as $q^{\frac{1}{2}}$ cannot be considered realistic in view of the preponderance of 3-body attachment ($e + 2O_2$) as a loss mechanism at these altitudes. For such a dissipative mechanism, the electron density varies linearly with the production rate. This feature is borne out qualitatively in Figure 20 giving the variation with altitude for the ratio of negative ions to electrons

The X-ray contribution to the ionization rate is given by $q = I_\lambda\, n\, \sigma_\lambda$, where I_λ is the solar intensity and σ_λ the cross section for ionization, both at the wavelength λ . The mechanisms for ionization, predominately photoelectric and Klein-Nishina effects, (cross sections calculated by Dalgarno) are discussed at some length by Nawrocki et al.[27] Of particular interest are the data gathered from the literature by Nicolet and Aiken for the variation of the ionization parameters with solar activity. Tables 12 and 13 give the

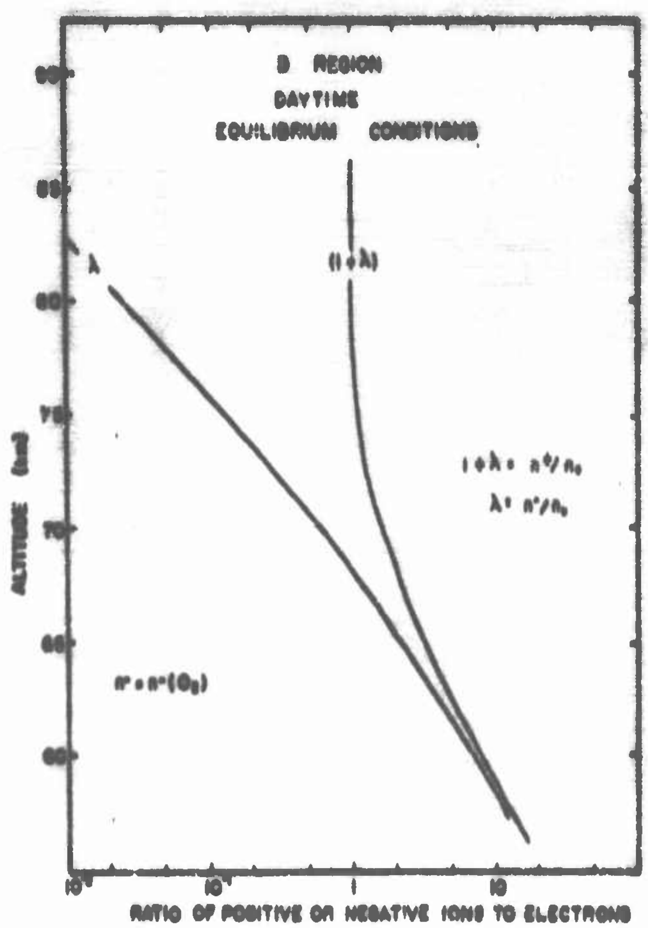

Figure 20. Variation of λ and $1 + \lambda$ with Altitude (after Nicolet and Aiken)

Variations in the X-Ray Intensities according to Various Solar Conditions
Energies in $erg \cdot cm^{-2} - sec^{-1}$.

Condition of the Sun	2 Å	4 Å	8 Å
Completely quiet	$10^{-[illegible]}$	10^{-7}	$10^{-[illegible]}$
Quiet	10^{-7}	$10^{-[illegible]}$	$10^{-[illegible]}$
Lightly disturbed	$10^{-[illegible]}$	$10^{-[illegible]}$	$10^{-[illegible]}$
Disturbed	$10^{-[illegible]}$	$10^{-[illegible]}$	$10^{-[illegible]}$
Special events (flares)	$10^{-[illegible]}$	$10^{-[illegible]}$	$10^{-[illegible]}$
Strong flares	$10^{-[illegible]}$	$10^{-[illegible]}$	$10^{-[illegible]}$

Table 12

Condition of the Sun	Ionization Coefficients, per molecule sec⁻¹ 2 Å	4 Å	8 Å
Completely quiet	1.0 × 10^[illegible]	9.8 × 10^[illegible]	2.8 × 10^[illegible]
Quiet	1.0 × 10^[illegible]	9.8 × 10^[illegible]	2.8 × 10^[illegible]
Lightly disturbed	1.0 × 10^[illegible]	9.8 × 10^[illegible]	2.8 × 10^[illegible]
Disturbed	1.0 × 10^[illegible]	9.8 × 10^[illegible]	2.8 × 10^[illegible]
Special events	1.0 × 10^[illegible]	9.8 × 10^[illegible]	2.8 × 10^[illegible]
Strong flares	1.0 × 10^[illegible]	9.8 × 10^[illegible]	2.8 × 10^[illegible]

Table 13

variation in X-ray intensities (I) and the ionisation coefficients ($I_\lambda \sigma_\lambda$) with solar activity and at zero optical depth.

Nicolet's suggestion concerning the possibility of the photo-ionisation of NO as a contributor to the ionisation of the D-region was placed on a quantitative basis by the photo-ionisation experiments of Watanabe and Marmo. Watanabe reported that at Lyman-α, NO had an absorption cross section of 2.4 x 10^{-18} cm^2 and an ionisation cross section of 2 x 10^{-18} cm^2. That Lyman-α could penetrate to the altitudes of the D-region was demonstrated by the measurement of Watanabe et al who obtained the absorption cross section of molecular oxygen as 1 x 10^{-20} cm^2. It remained for Nicolet to calculate the concentration of NO and relate this to the Lyman-α flux of 3 ergs cm^{-2} sec^{-1} measured by Rense.

The ionisation rates for the various radiations were computed by Nicolet and Aiken according to

$$q_j = n_j I_{j,\infty} \exp\left[- \sum n_j K_j H \sec\chi \right] \qquad (29)$$

where the j subscript refers to the jth constituent, I_j is the ionisation rate coefficient corresponding to zero optical depth and the exponent refers to the unabsorbed fraction. In other words this term corresponds to the optical depth τ_λ for an overhead sun multiplied by the solar zenith distance χ. The optical depths for Lyman-α and X-rays are given by

$$\tau_\lambda^{L} = n(O_2)\, K_\lambda(O_2)\, H \qquad (30$$

$$\tau_\lambda^{x} = n(m)\, K_\lambda(M)\, H$$

where K_λ is the absorption cross section. The unit optical depths for an overhead sun for x and Lyman-α radiations are:

λ (A)	2	4	6	1216
Altitude (km)	70	80	87	75

The conventional equation of ionization below 80 km is given by Nicolet and Aiken as

$$\frac{dn_e}{dt} = \frac{\Sigma q_j}{1+\lambda} - \alpha_e n_e^2 - \frac{n_e}{1+\lambda}\frac{d\lambda}{dt} \qquad (31)$$

where q_j denotes the electron production rate for the j specie, α_e represent the effective recombinance between positive ions and electrons and λ the ratio of negative ions to electrons. Assuming that processes dealing with attachment and detachment of electrons are rapid then $d\lambda/dt = 0$ so that

$$\frac{dn_e}{dt} = \frac{\Sigma q_j}{1+\lambda} - \alpha_e n_e^2 \qquad (32)$$

This then represents a practical equation for calculating the variation of the electron concentration. Table 14 and Figures 21 and 22 give the calculations of Nicolet and Aiken for the expression $(n^+ n_e)$ produced by the three sources at altitudes of 60, 70, and 80 km, the variation of electron density with solar zenith angle, and the variation of the electron density with solar activity, respectively. Figure 23

n^+n_e at 60, 70, and 80 km			
Altitude: 60 km	Cosmic Rays	X Rays	Lyman α
$n^+(O_2)n_e$	2.1×10^4	1.8×10^1	
$n^+(N_2)n_e$	4.7×10^4	2.3×10^1	
$n^+(NO)n_e$			3.0×10^0
Totals	6.8×10^4	4.1×10^1	3.0×10^0
Total	$6.8 \times 10^4\ cm^{-6} = (1 + \lambda)n_e^2$		
Altitude: 70 km	Cosmic Rays	X Rays	Lyman α
$n^+(O_2)n_e$	4.6×10^4	2.8×10^2	
$n^+(N_2)n_e$	2.9×10^4	0.8×10^2	
$n^+(NO)n_e$			7.0×10^4
Totals	7.5×10^4	3.6×10^2	7.0×10^4
Total	$1.54 \times 10^5\ cm^{-6} = (1 + \lambda)n_e^2$		
Altitude: 80 km	Cosmic Rays	X Rays	Lyman α
$n^+(O_2)n_e$	2.7×10^4	2.1×10^4	
$n^+(N_2)n_e$	6.6×10^3	2.9×10^3	
$n^+(NO)n_e$			1.8×10^6
Totals	3.4×10^4	2.4×10^4	1.8×10^6
Total	$1.8 \times 10^6\ cm^{-6} = (1 + \lambda)n_e^2$		

Table 14 (after Nicolet and Aiken)

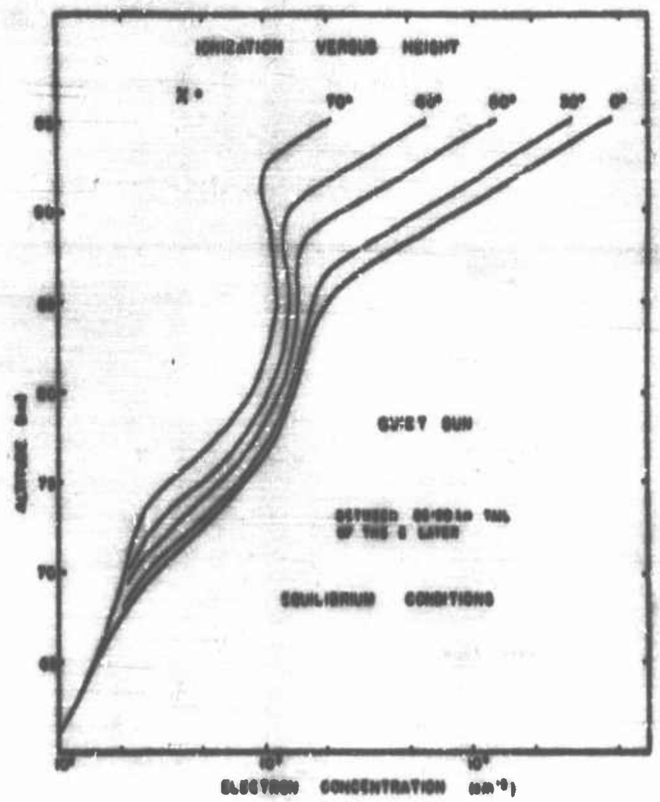

Figure 21. Variation of the Electron Concentration with the Solar Zenith Distance when Equilibrium Conditions are Considered (after Nicolet and Aiken)

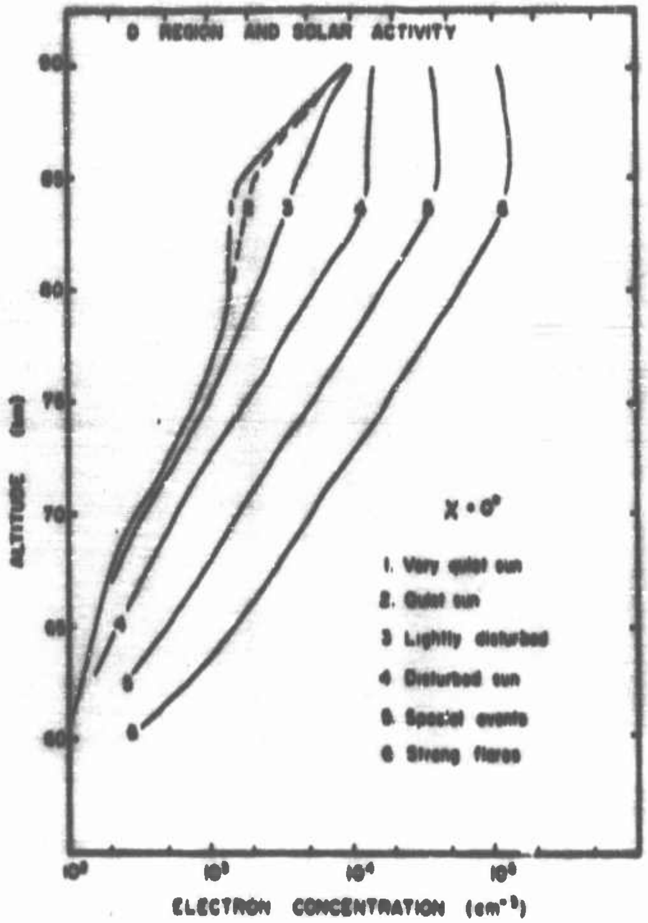

Figure 22. Variation of the Electron Concentration according to Solar Conditions. No effect from 35 to 100 Å is considered (after Nicolet and Aiken).

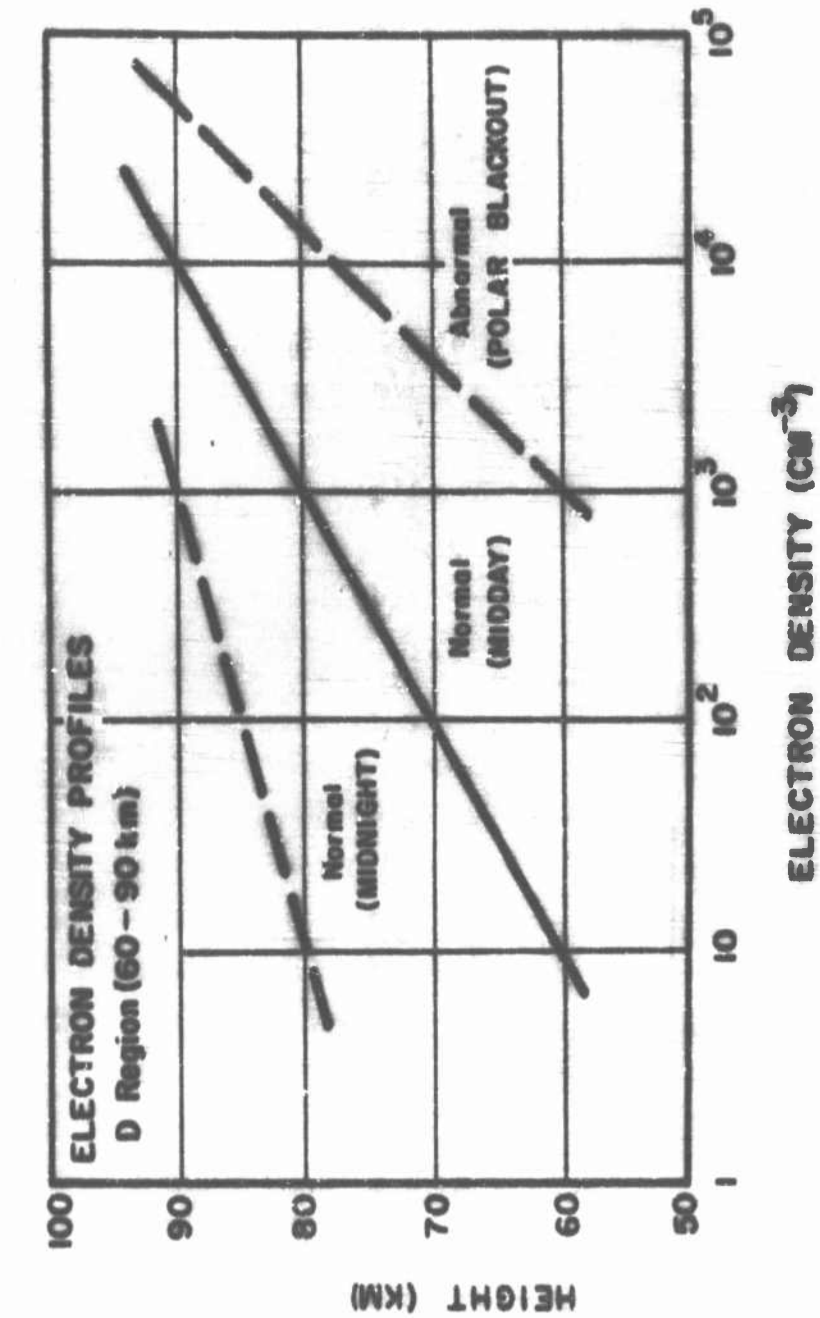

Electron density profiles, D region (60-90 km)

Figure 23

gives some estimate of the effect of auroral particles on the ionisation in the D-region for magnetic latitudes greater than 60°.

3.3 The E and F Regions*

The two competing theories for the formation of the E region are: (A) photoionization of O_2,

$$O_2 + h\nu\ (800\text{-}1027\,\mathrm{A}) \rightarrow O_2^+ + e \qquad (33)$$

as proposed by Wulf and Deming[28] and modified by Nicolet[29]; (B) general ionization of air by soft X-rays (10-100 A) suggested by Vegard[30] and Hulburt[31] in 1938. Subsequently, many investigators (Ref. 32-41) have made studies to determine the dominating process; however, these studies were based on rather incomplete data and often on incorrect assumptions such as blackbody solar spectrum. Most investigators[42] seem to favor the X-ray theory on the basis of intensity measurements by Byram, Chubb, and Friedman[43,35]; while Watanabe, Marmo, and Pressman[39] have given reasons for not rejecting the molecular oxygen theory.

Watanabe's study differs from earlier work in that a flux (0.6 erg $cm^{-2}sec^{-1}$ or about 2.8×10^{10} photons $cm^{-2}sec^{-1}$) in the region 800-1027 A is much higher than previous estimates (less than 0.001 erg $cm^{-2}sec^{-1}$ by Byram et al[35] and about 0.01 by Kamiyama[41]. The higher flux is still about one-half of Hinteregger's value[23] at 210 km. For the soft X-ray region, 10-100 A, the value observed by Byram et al[43] was used.

---

* Section 3.3 through 3.36 were taken from GCA Tech. Report 60-3-N prepared for NASA

If the selected intensities are approximately correct, soft X-rays contribute less than 5% to the total ionization rate in the E region. Thus the production of the normal E layer is apparently due to photo-ionization of O_2 by the action of ultraviolet radiation in the range 800-1027 A. Some O^+ ions are formed in the upper E region by radiation in the spectral region 800-911 A which includes the strong Lyman continuum of hydrogen.

During the time of flares, the X-ray intensities may be enhanced considerably and may make a greater contribution to the E region electron density. In fact according to Friedman[44], X-ray intensities as high as 1.0 erg $cm^{-2}sec^{-1}$ have been observed. However, in view of the difficulty in the interpretation of photon counter data[43], it seems desirable to further study this spectral region with monochromators.

According to Nicolet and Aikin[24] the dissociative recombination rates for N_2^+ is 5×10^{-7} $cm^3 sec^{-1}$ and for O_2, 3×10^{-8} $cm^3 sec^{-1}$. If these rates are approximately correct, the effectiveness of X-ray ionization is reduced because the slower reaction

$$O_2^+ + e \rightarrow O' + O''$$

will tend to control the electron density in the lower E region.

As the altitude increases, the relative amount of O^+ ion increases, additional amount of radiation in the region below 911 A becoming available. Following Bates[45], the recombination of O^+ ion may be largely controlled by the reactions

$$O^+ + O_2 \rightarrow O_2^+ + O \qquad (34)$$

$$O_2^+ + e \rightarrow O' + O'' \qquad (35)$$

where Eq. (34) tends to become the rate limiting process; on the other hand N_2^+ recombines rapidly by dissociative recombination.

The Watanabe computations show that the base of the E region is controlled mainly by Lyman-beta and partly by other radiation in the spectral region 1000-1027 A where N_2 is very transparent. For example, in the case of Z = 0°, Lyman beta contributes about 60% of the total ionization rate at 100 km and about 70% at 105 km, so that the electron density curve in the region 95-105 km should closely approximate an ideal Chapman curve. Above this region there is increasing superposition of Chapman-type curves due to several prominent emission lines in the spectral region 900-1000 A. The results for the lower E region appear to be in harmony with the description by Ratcliffe and Weekes[46]: "The shape of the layer and the way in which its height varies through the day are roughly what would be expected for an equilibrium Chapman layer found in an atmosphere of scale height 8 km, with its peak at a level of 105 km for vertically incident ionizing radiation".

3.3.1 Solar Flux and Photoionization Cross Sections

The recent advances (by means of rockets and satellites) in the measurements of the parameters of the upper atmosphere permit a more detailed and quantitative study of the photoionisation rates than was previously possible. Nicolet and Aikin[24] had accomplished this in the D region where the critical spectral ranges are 1100-1340 Å. Calculations of the ion production rates depend upon three basic data the solar ultraviolet flux, the composition of the atmosphere, and the cross sections of the various reactions (macroscopic motion such as vertical drift are tentatively neglected). Table 15 gives reduced versions of the solar flux (as deduced from the measurement of Tousey[22] and Hinteregger[23]) and Table 16 the composition. The total densities used by Watanabe as given in Fig. 2 do not include the G.S.P. effect. However, below the F-2 maximum, the differences between these total densities and those of Minzner and Jacchia are small. For the spectral range 911-1027 A, the listed values lie between those of Tousey and of Hinteregger, the latter being higher. For the range 100-911 A, the selected flux is about 30% higher than the flux observed by Hinteregger at 210 km but is about one third their extrapolated value. Such an extrapolation, of course, depends on the choice of reference atmosphere and absorption cross sections. For the region 10-100 A, the total flux given in Table 15 is a little higher than the 0.1 erg cm^{-2} sec^{-1} obtained by Byram et al[43] who matched the responses of three photon counters to a single coronal temperature. Some values in Table 15 are Watanabe's estimates based on visual comparison of emission lines in the solar spectrum[47]. The uncertainty in the total flux is probably no more than a factor of two, since Hinteregger has used a photoelectric technique which is very amenable to energy calibration and quite insensitive to scattered light.

TABLE 15

Solar flux, q_o in the 10^8 photons $cm^{-2} sec^{-1}$, for the spectral range 1027-10 A at normal incidence outside of Earth's atmosphere. The q's of weak lines and continuum are lumped together for each interval, while q's of prominent lines are listed separately.

λ (in A)		q_o	λ (in A)		q_o
1025.7	Ly β	35	629.7	O V	10
1011	lines	2.5	610,625	MgX	10
1000-1027		3.5	584.3	HeI	13
989.8	N III	10	554	O IV	2
977.0	C III	29	537	HeI	4
972.5	Ly γ	9.7	520	Si XII	9
949.7	Ly δ	4.0	500-650		60
937.8	Ly ϵ	2.3	499	Si XII	5
934,944	S VI	1.9	303.8	He II	68
930-1000		6.7	300-500		63
911-930		13.7	250-300		21
850-911		134	170-250		25
834	O II,III	6	100-170		4.5
800-850		21	60-100		4.2
788,790	O IV	5	40-60		0.5
770,780	Ne III	5	20-40		0.15
650-800		71	10-20		0.015

TABLE 16

Number density n (in particles/cm^3) and layer thickness L (in cm reduced to STP) at various altitudes H (in km)

H	n			L		
	O	O_2	N_2	O	O_2	N_2
90	7.1×10^{11}	1.16×10^{13}	4.2×10^{13}	3.0×10^{-2}	2.14×10^{-1}	8.2×10^{-1}
95	7.3	4.2×10^{12}	1.62	2.36	8.4×10^{-2}	3.3
100	4.2	1.55	6.2×10^{12}	1.30	3.6	1.46
105	2.3	6.5×10^{11}	2.7	7.2×10^{-3}	1.63	7.0×10^{-2}
110	1.13	2.8	1.18	4.1	8.3×10^{-3}	3.7
115	3.8×10^{10}	1.31	5.7×10^{11}	2.64	4.7	2.14
120	3.3	7.1×10^{10}	3.1	1.64	2.96	1.36
130	1.29	2.4	1.09	1.07	1.41	6.8×10^{-3}
140	6.6×10^{9}	1.10	5.1×10^{10}	7.4×10^{-4}	8.2×10^{-4}	4.0
150	3.8	5.7×10^{9}	2.7	5.6	5.2	2.63
160	2.5	3.3	1.62	4.4	3.6	1.85
170	1.75	2.1	1.07	3.7	2.62	1.36
180	1.28	1.42	7.3×10^{9}	3.1	1.97	1.03
200	8.1×10^{8}	7.5×10^{8}	4.0	2.37	1.22	6.2×10^{-4}
220	5.8	4.6	2.4	1.87	7.9×10^{-5}	4.0
250	3.7	2.3	1.12	1.35	4.3	2.1
300	1.98	8.1×10^{7}	3.8×10^{8}	8.4×10^{-5}	1.63	8.4×10^{-5}
350	1.20	3.2	1.57	5.4	6.5×10^{-6}	3.8
400	7.9×10^{7}	1.32	7.2×10^{7}	3.6	2.6	1.81
500	3.6	1.9×10^{6}	1.6	1.6	4×10^{-7}	4×10^{-6}

The longest wavelength in Table 15 corresponds to the first ionization potential of O_2 but it should be noted that photons of longer wavelengths can ionize an O_2 which is in an excited state. For example, at a temperature of 1000°K about 10% of O_2 molecules are in the first vibrational level; hence radiation of wavelengths up to 1043 A can ionize these molecules. In the altitude region above about 150 km the solar O VI emission lines at 1032 A and 1038 A with intensities (6×10^9 photon cm^{-2} sec^{-1}) comparable to that of Lyman-beta can produce some ionization. As to the absorption and photo-ionization cross sections, existent information appears to be adequate since the effects are integrated over many wavelengths. Watanabe[48] has reviewed the data on absorption cross sections and has listed in Table 17, recommended values for O_2 and N_2. Similarly, Dalgarno[49] has presented sets of recommended values for O and N atoms from their ionization threshold to 0.1 A.

The wavelengths corresponding to the ionization threshold of O_2, O, and N_2 are, respectively, 1027, 911, and 796 A. Calculations of photoionization rates require both the total absorption and the photoionization cross sections of these constituents, since part of the solar ultraviolet flux in the region below 1027 A is removed by absorption processes not leading to ion production. For example, solar Lyman-gamma (972.5 A) can ionize O_2 molecules but it is almost entirely absorbed by N_2 molecules at altitudes above 200 km and therefore makes a negligible contribution to the E and F regions. As pointed out by Kato[50], part of the solar Lyman-beta is absorbed

TABLE 17.

Absorption coefficient k (cm^{-1}) of N_2 and O_2 for some solar ultraviolet lines in the region 200-1000 A.

λ		$K(N_2)$	$K(O_2)$
200		200	300
303.8	(He II)	160	500
584.3	(He I)	520	540
609.7	(Mg X)		600
787.7	(O IV)	250	?
790.2	(O IV)	670	?
832.7	(O III)	92	670
833.3	(O II)	260	380
833.7	(O III)	230	340
835.3	(O III)	120	300
903.6	(C II)	300	250
903.9	(C II)	25	240
904.5	(C II)	250	210
937.8	(H I)	200	115
949.7	(H I)	90	160
972.5	(H I)	7600	1000
977.0	(C III)	100(?)	90
989.8	(N III)	(?)	60
1025.7	(HI)	0.01	45

by atomic oxygen, but the amount appears to be small[51] due to the fact that Lyman-beta is broadened; this is also the case of Lyman-alpha[52].

Atmospheric absorption in the spectral region 800-1100 A which is important to the E region is essentially controlled by O_2 and N_2. For O_2, both the absorption and photoionization cross sections have been measured by Watanabe and Marmo[53] at many wavelengths. But for N_2, published data are meager, partially due to the complexity of the N_2 absorption spectrum. Absorption coefficients vary from almost zero to as high as 7600 cm^{-1} in this region. Some data by Itamoto et al[54] were used.

For the spectral region 100-800 A which is critical to the F region, available data are again rather meager; however, the spread in the absorption coefficient is comparatively small owing to the fact that continuous absorption sets in for all major constituents. The spread is probably from 100 cm^{-1} to 1000 cm^{-1}. For example at 584 A, the absorption coefficients of O_2, N_2, and O are, respectively, 540, 520 and 330 cm^{-1}, and at 304 A, respectively, 300, 160, and 250 cm^{-1}. The photoionization yield is also uniformly high, nearly 100 percent in most cases. Thus, errors in the cross section appear to be less serious than errors in composition.

3.3.2 Penetration of Solar Ultraviolet

The solar ultraviolet flux at each altitude is calculated by means of the equation

$$q = q_o \exp\left(-\sum k_i L_i\right) \qquad (36)$$

where q_o and q are the incident and transmitted flux for a given wavelength, k_i = absorption coefficient of each constituent, and L_i is the layer thickness for each constituent as given in Table 16. The transmission, T in percent, is defined by

$$T = 100\,(q/q_o) \qquad (37)$$

The results for particular wavelengths are shown in Figure 24 for $Z = 0^{\circ}$. Figure 24 indicates that for $Z = 0^{\circ}$, radiation of wavelengths 800-1027 A is absorbed mainly in the altitude range 100-150 km (E region), while radiation in the range 100-800 A is absorbed mostly at altitudes 140-200 km or the lower F region. Only a small portion of the solar ultraviolet is absorbed in the region above 200 km at $Z = 0^{\circ}$ since the absorption coefficient of the gases is less than 1000 cm^{-1} at most wavelengths. An interesting exception is Lyman-gamma; at its wavelength, k = 7600 cm^{-1} for N_2 and about 1000 cm^{-1} for O_2. The results for the depth of penetration are somewhat higher than previous estimates[19] because the recent atmospheric densities above 150 km are higher than pre-satellite data.

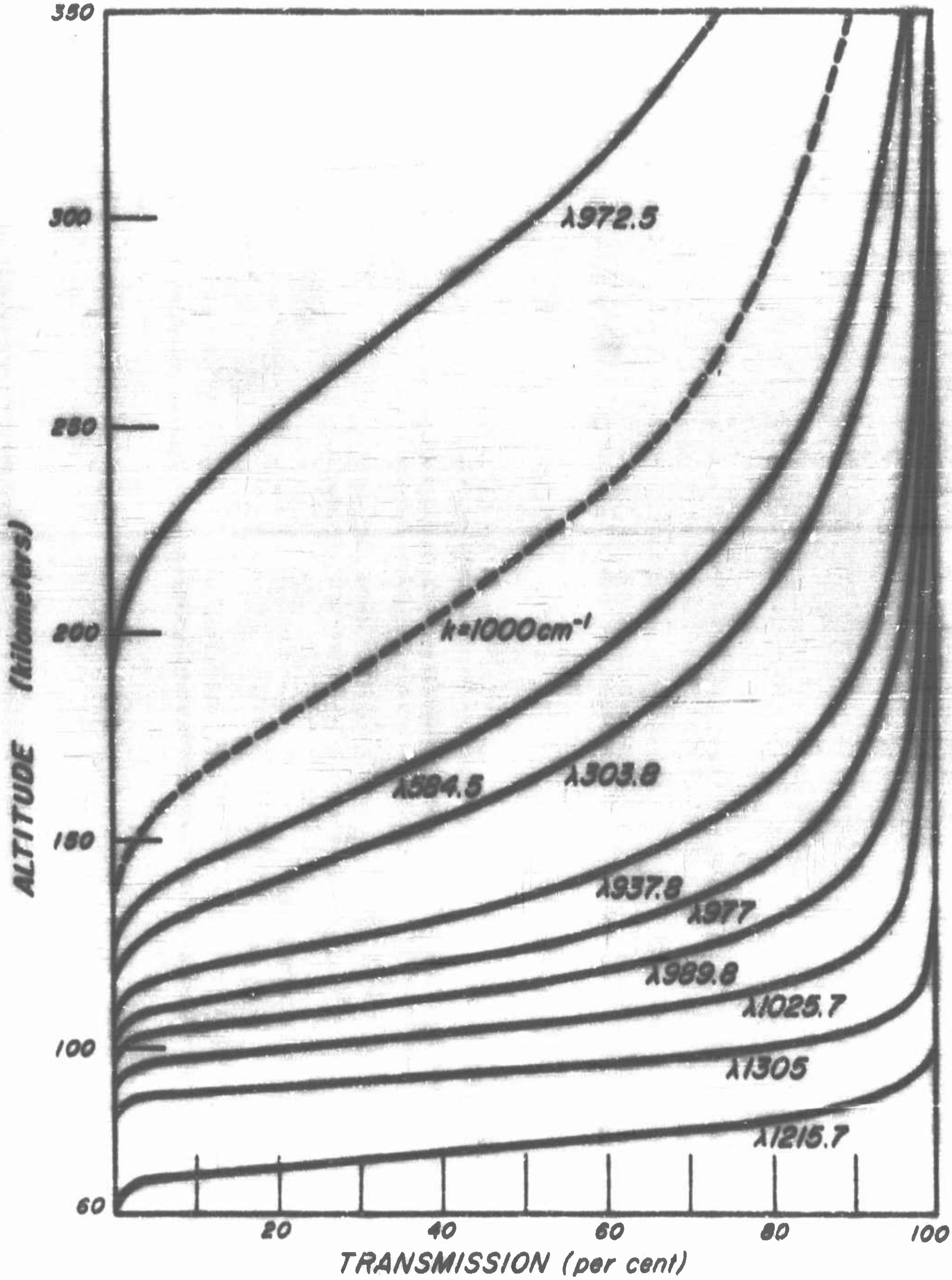

Figure 24. Transmission at Normal Incidence Versus Altitude for Several Solar UV Emission Lines. Broken curve is for air with effective $k = 1000\ cm^{-1}$.

The calculations can be checked against photographs of solar spectrum.[47] For example, the solar C III line at 977 A penetrates to about 110 km and Lyman gamma down to 200 km, in agreement with rocket observations. Although no serious discrepancies are found, the calculations are considered tentative since the available spectra are still insufficient to permit quantitative comparisons. It should also be noted that laboratory absorption coefficients may not be directly applicable if the solar emission line is much broader than the corresponding line used in the laboratory. This appears to be the case in Lyman-gamma, which is indeed detectable at altitudes below 200 km.

Figure 24 is also consistent with the rapid change in the scale height at about 120-170 km. Since the maximum rate of absorption of radiation in the range 100-1100 A occurs in this region, there should be considerable heating here.

3.3.3 Photoionization Rates

Expressions for the rate of ion-pair production in the atmosphere under the action of solar radiation have been derived previously by Chapman[55-57] and others[58-59] using various assumptions. The original Chapman theory[55] assumes monochromatic radiation, isothermal atmosphere, and a single gas constituent. The theory has been extended to include other assumptions such as varying scale height[58-59] and band absorption.[56] These derived expressions serve as valuable theoretical background but cannot be applied readily to the present conditions (varying composition, varying scale height, complex solar spectrum and many absorption and photoionization cross sections). Therefore, it was necessary to resort to numerical summation of the various components for the layer thickness.

The photoionization rate p in ion-pair cm^{-3} sec^{-1} at a given altitude is given by the expression

$$p = \sum_{\lambda} q_{\lambda} (\Sigma \sigma_i n_i) \qquad (38)$$

where q_{λ} is the UV flux for a given wavelength at the given altitude defined by Eq.(36), σ_i = photoionization cross section of each constituent at each wavelength, and n_i is the number density of each constituent at the given altitude.

It is of interest to subdivide the total p at each altitude into contributions from several spectral ranges: 911-1027 A which ionizes only O_2; 796-911 A which ionizes both O and O_2; 100-796 A which ionizes O, O_2 and N_2; and 10-100 A which is absorbed in the E region. Figures 25 and 26 give the photoionization rates for $Z = 0^{\circ}$ and $Z = 84.3^{\circ}$, respectively. The broken curves represent the contributions of the four spectral ranges and the solid curve with two principal maxima, ϵ and ϕ, gives the total rate. Figure 26 also shows secondary maxima between ϵ and ϕ. For $Z = 0^{\circ}$, the

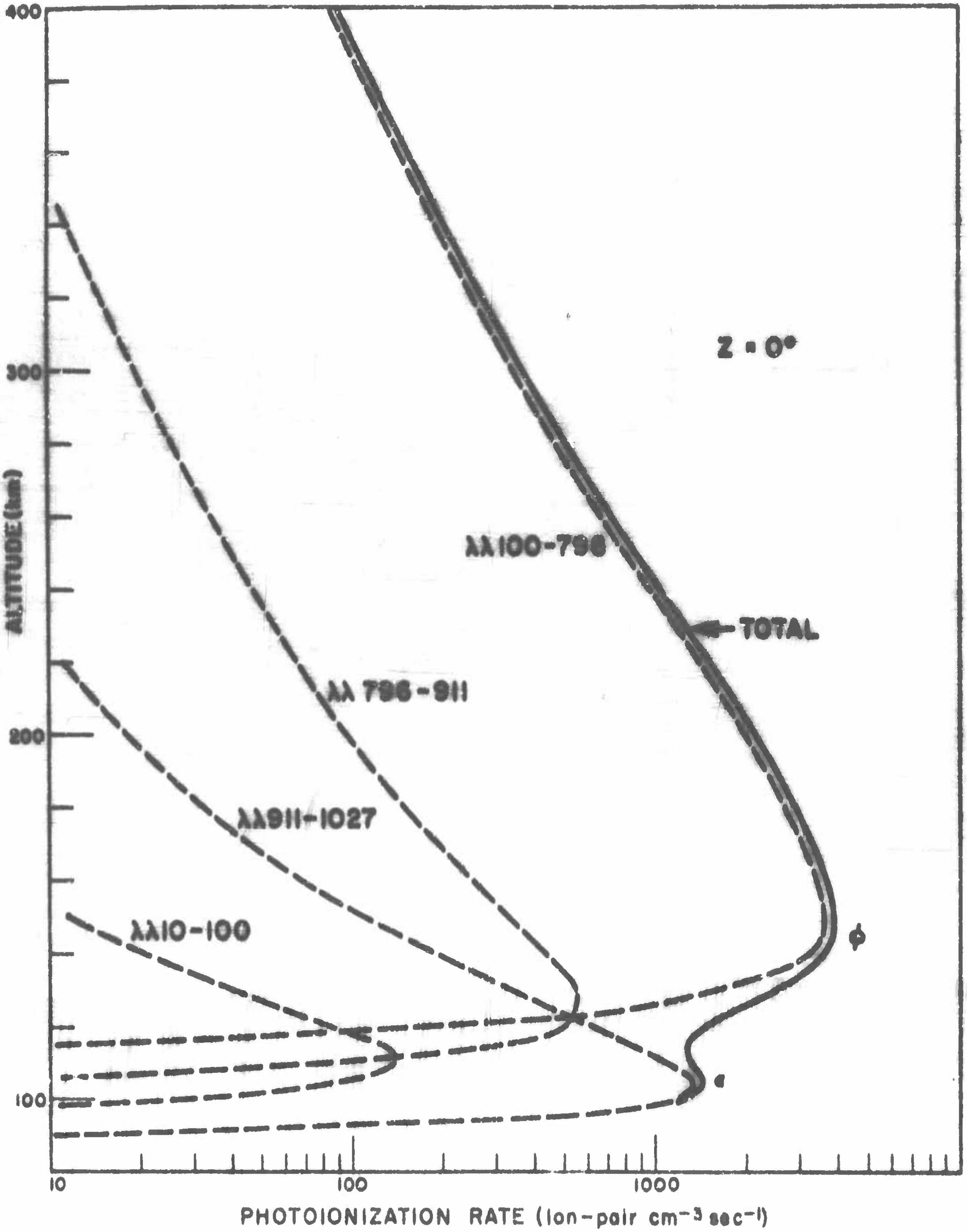

Figure 25. Photoionization Rate Versus Altitude for Normal Incidence. Broken curves give rates due to respective spectral ranges and solid curve total rates.

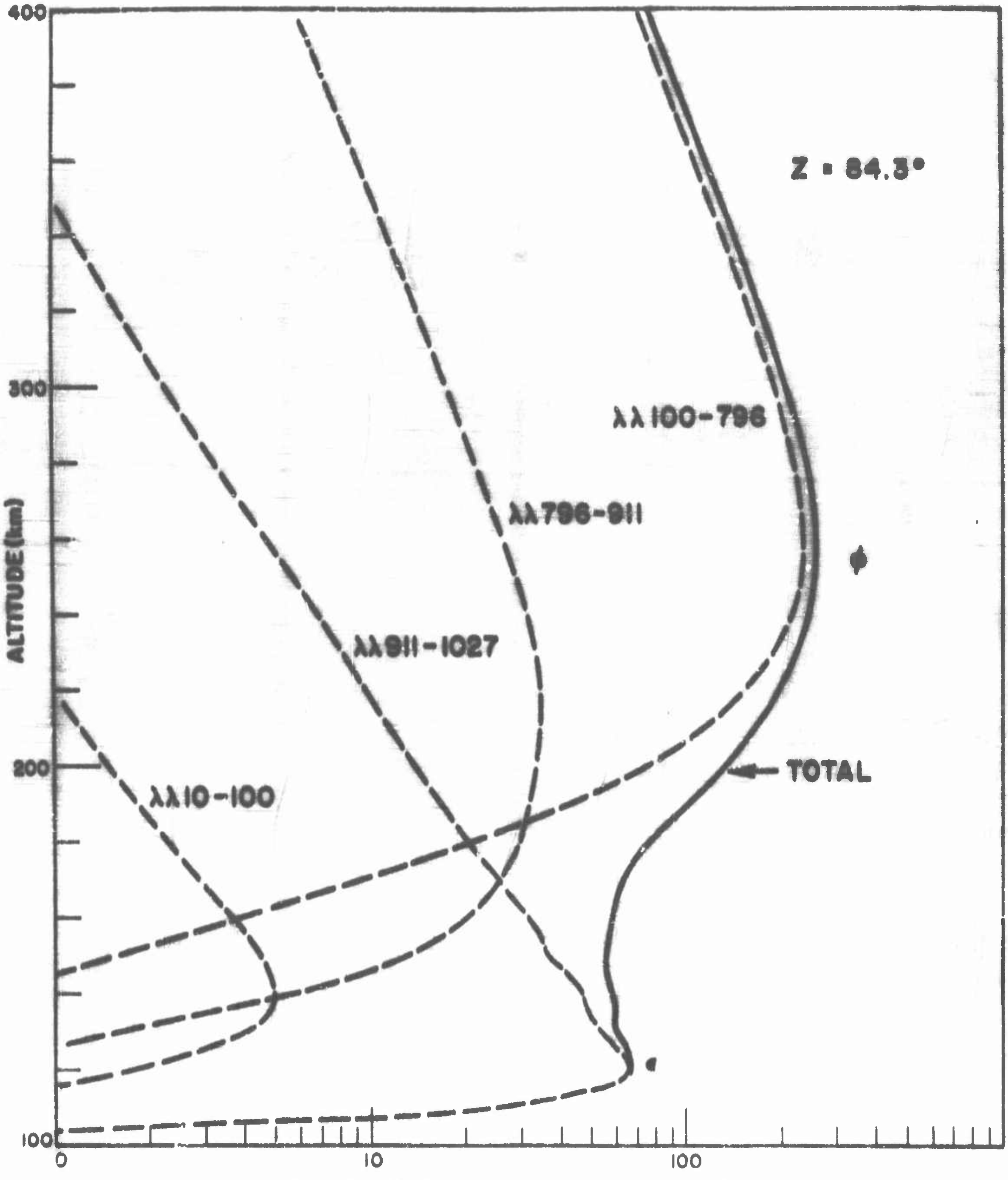

Figure 26 Photoionization Rate Versus Altitude for Solar Zenith Angle Equal to 84.3°

lower maximum is at about 105 km (E region) and the higher maximum is at about 150 km (bottom of the F_1 region). For $Z = 84.3^o$, the corresponding maxima have shifted to 120 and 280 km, respectively. The larger shift of the maximum is due to the large scale height in the region above 150 km and is the basis for the formation of the F_2 region.

The photoionization rates (see Table 18) are from 20 to 100 times larger than those computed by Havens, Friedman, and Hulburt,[60] and are more nearly in agreement with rates implied by radio measurements.

Table 18

PHOTOIONIZATION RATES (ION-PAIR CM^{-3} SEC^{-1})

Altitude (km)	150	200	250	300	350
Havens *et al*	200	80	20	5	1.6
Present study $Z = 0^o$	3850	2140	890	370	180
$Z = 90^o$	17	36	125	155	115

In addition, Johnson[61] found it necessary to increase the flux used by Havens *et al*[60] by fifteen times in order to account for the high temperatures existing in F region, and his indirect estimate of the flux for the He II line at 304 A is remarkably close to Hinteregger's[23] results.

The comparatively high ionization rates in the F region for $Z = 90^{\circ}$ show that ionization in this region is not negligible even during the twilight period. The ionization rate at about 300 km changes only by a factor of two throughout the day, but at 150 km the change is more than a factor of 10^2.

3.3.4 Formation of the F Region

As a result of the work of Jackson[62] and others, the concept of a vertical distribution of electron density as a succession of layers has been replaced by changes in the gradient of a monotonically increasing function (to the F-2 maximum). E and F_1 "peaks" become regions of high electron density gradient.

Early theories[63] of the F-layer usually involved two different absorption processes to explain the origin of the two F regions; but according to Bradbury's hypothesis[64] both "layers" are produced by the same radiation and the double layer is then due to the rapid decrease of recombination coefficient with altitude. Bates[45,32] considers this hypothesis to be essentially correct.

Watanabe's study of the various radiation and related cross sections has failed to reveal any photoionization process giving maximum, noon-time rate in the F_2 region. As shown in Figure 34, Lyman-gamma is largely absorbed in the F_2 region by N_2 rather than O_2, so its absorption provides negligible amounts of ionization.

The radiation responsible for the ionization in the F_1 and F_2 regions lies in the broad spectral range 100-1000 A, with the 304 A line of He II as the strongest emission line and with large contributions from the ionization continua of hydrogen and helium. As shown in Figure 25, ultraviolet radiation in this range at vertical incidence produces a maximum ionization rate at 150 km; however, it should be emphasized that many wavelengths and several absorption processes are involved.

A further insight into the production of the F_1-ledge and F_2 peak can be obtained with the aid of Figure 27 which shows the photoionization rates for different zenith angles. At sunrise the maximum ionization rate ϕ is at about 300 km, approximately coinciding with the height of the peak of the night-time electron density ($\sim 10^5 cm^{-3}$). Hence during the hour period around sunries, there is a comparatively high "build up" of electron density at this altitude due to the combined effect of the low recombination rate and relatively high ionization rate. As the sun rises, the location of the maximum ionization rate ϕ descends rather rapidly to the F_1 region, but due to the higher recombination rates found at lower altitudes, the F_2 electron density peak at 300 km does not correspondingly shift downward; instead, a ledge appears in the electron density curve and descends to about 150 km. In other words

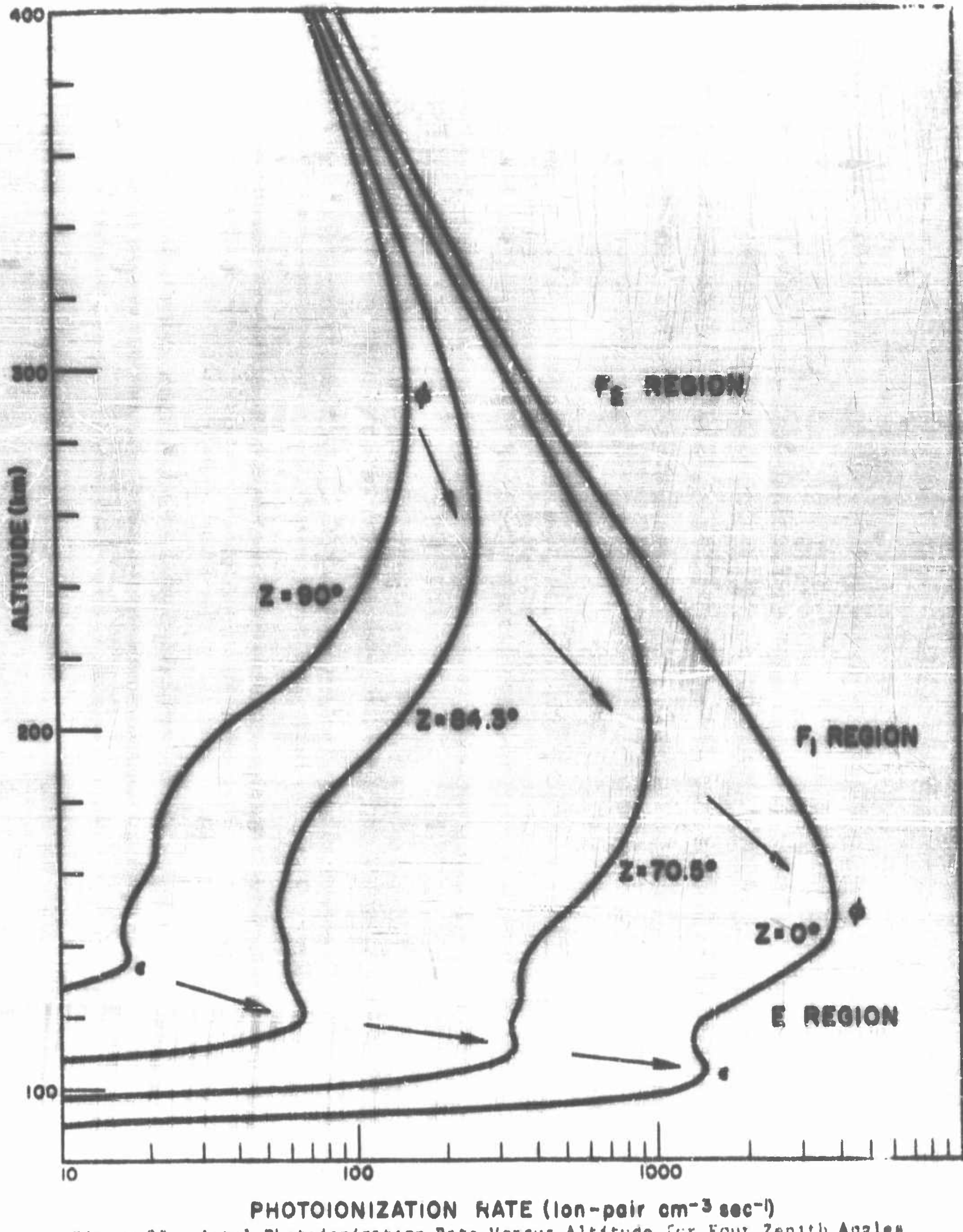

Figure 27 Total Photoionization Rate Versus Altitude for Four Zenith Angles Arrows show the direction of displacement of the peaks, phi, and epsilon

the so-called "splitting" or "bifurcation" of the F layer is the result of the enhancement and persistence of the F_2 peak and the movement of the F_1 ledge. Thus this study supports the work of Bradbury,[64] Bates,[32] and others.

3.3.5 Electron Density and Recombination Coefficients in the E and F Regions

Ignoring vertical drift, the following equation may be used to estimate the electron density and its variation with time,

$$dn/dt = q - \alpha' n^2 \tag{39}$$

where n = electron density, q = effective electron production rate and α' = effective recombination coefficient. Published values of α' show a wide spread; for example Bates and Massey[65] have used $1 \times 10^{-8} cm^3 sec^{-1}$ for the E layer (at 120 km) and Mitra and Jones[66] have reported $3 \times 10^{-8} cm^3 sec^{-1}$ at 100 km and $1.6 \times 10^{-8} cm^3 sec^{-1}$ at 140 km. The variation of α' with altitude is approximately represented by the broken curve in Figure 28.

Near the bottom of the E region at about 105 km, photons in the range 1000-1027 A produce most of the electron-ion pairs by photoionization of O_2, (absorption by O and N_2 is negligible). q, the photoionization rate, is very small at sunrise but reaches about $100 cm^{-3} sec^{-1}$ after half an hour and exceeds $300 cm^{-3} sec^{-1}$ in 2 hours. By numerical integration and successive approximation n is

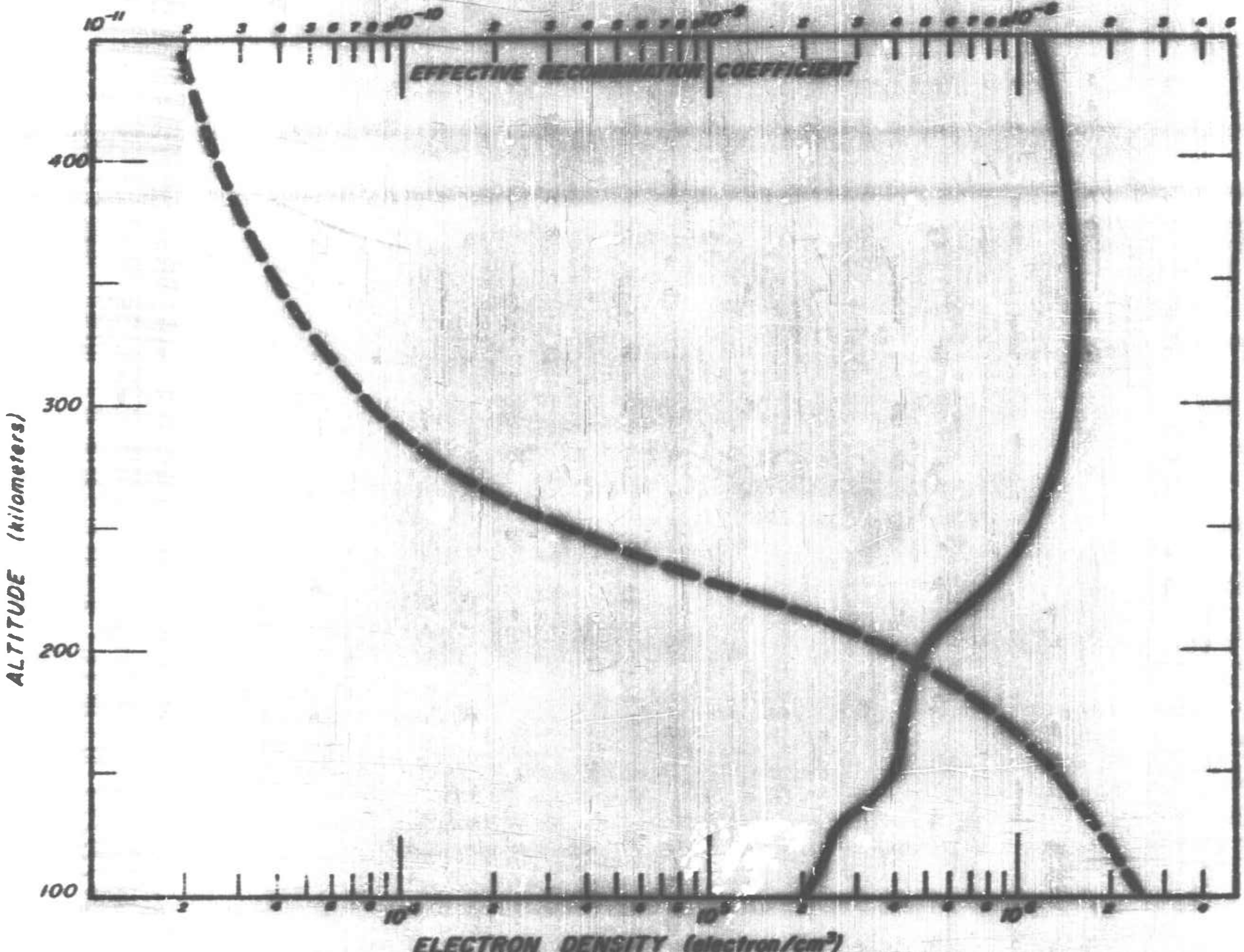

Figure 28. Broken curve represents effective recombination coefficients (in $cm^3 sec^{-1}$) versus altitude. Solid curve represents electron density versus altitude according to Jackson.

found to increase rapidly during the same period so that during the greater part of the day dn/dt is small compared to q and αn^2. This is quasi-equilibrium or $dn/dt \sim 0$. Using α = $2.5 \times 10^{-8} cm^3 sec^{-1}$, $q = 1400\ cm^{-3} sec^{-1}$ for $Z = 0$, $n = 2.4 \times 10^5 cm^{-3}$ which is the correct order of magnitude for the maximum electron density in the E region. It should be added that X-rays produce some N_2^+ and O^+ ions, the former recombining more rapidly, and the latter more slowly, than O_2^+. Ionic composition determined by Johnson et al[67] shows that O_2^+ is much more prevalent than O^+ at this altitude; a result which tends to support the above calculation. Furthermore, the effective recombination coefficient at this altitude appears to be controlled mainly by the dissociative recombination of O_2^+.

In the upper E region at about 130 km, the radiation in the region below 911 A as well as radiation in the region 911-1000 A plays an important role, especially for near-vertical sun. Photons in these regions can ionize O and N_2 as well as O_2. Since the loss rate of N_2^+ is faster than that of other ions, the calculated photo-ionization rate ($2000\ cm^{-3} sec^{-1}$) is reduced to an effective electron production rate of about $500\ cm^{-3} sec^{-1}$. This value combined with $\alpha = 1.8 \times 10^{-8} cm^3 sec^{-1}$ yields $n = 1.6 \times 10^5\ cm^{-3}$ for the noon time electron density. Though this density is somewhat lower than that for the 105 km level, it does not establish firmly that there is shallow minimum in the electron density curve.

Near the bottom of the F_1 region at about 160 km, the night-time electron density is about $10^4 cm^{-3}$, and according to the above numerical integration, this density is increased to $10^5 cm^{-3}$ at the end of the first hour after sunrise. Subsequent to this period, dn/dt again becomes small compared to q and αn^2, so that quasi-equilibrium exists in the F_1 region. If q is taken to be one-third the calculated photoionization rate ($3700\ cm^{-3} sec^{-1}$) and $\alpha = 8 \times 10^{-9} cm^3 sec^{-1}$, the maximum electron density of the F_1 ledge is $n = 3.9 \times 10^5 cm^{-3}$; this value is in line with the observed electron density curve[62] (Figure 28). The recombination coefficient used here may seem high but is consistent with the relatively high O_2 concentration in the assumed model atmosphere (Table 16). In other words, the slower recombination process involving O^+ is not fully effective as the rate determining process.

In the F_2 region at about 300 km, the night-time electron density is about $2 \times 10^5 cm^{-3}$, and according to the numerical integration, this density is doubled during the first hour after sunrise and subsequently increases rather slowly (compared to the situation at lower altitudes). As shown in Figure 27, the photoionization rate is nearly constant after the first hour. For constant q, the electron density is given by the equation

$$n = (q/\alpha)^{\frac{1}{2}} \tanh \left[(\alpha q)^{\frac{1}{2}} t + \text{const.} \right] \qquad (40)$$

and n approaches the limit $(q/\alpha)^{\frac{1}{2}}$. If the effective q is one-third of the photoionization rate and $\alpha = 8 \times 10^{-10} cm^3 sec^{-1}$

the maximum electron density is 1.3 x $10^6 cm^{-3}$ which compares favorably with observed value. It is to be noted that this is a somewhat simplified picture of the dynamics of the ionization of the F-region. Considerations of the sub-solar bulge(and its implications concerning vertical drift) would have to be added if the fine-structure of the F-2 region as exhibited in Figure 29 is to be generated quantitatively.

3.3.4 Degree of Ionization above 700 km

With the satellite-drag data, direct measurements on the ionic species, and the radio data, it appears that the total density and the electron density (Figures 2 and 30) are fairly well known up to altitudes of 700 km. At 700 km, Jacchia has found that variations in the density (due to both random and solar-associated phenomena) may be as high as a factor of 20. This, of course, implies that a static model is of limited use at the extreme heights of the terrestrial atmosphere. Present ideas on the effect of the solar wind in distorting the terrestrial magnetic field (and thus the distribution of the dominantly ionized medium) tend to substantiate change as the basic attribute of the upper regions. On the other hand, it is presently considered that even to heights of 700 km, the neutral composition remains relatively unknown. In spite of the lack of information concerning the composition, it might be possible to arrive at probable values of the degree of ionization. This parameter is of some

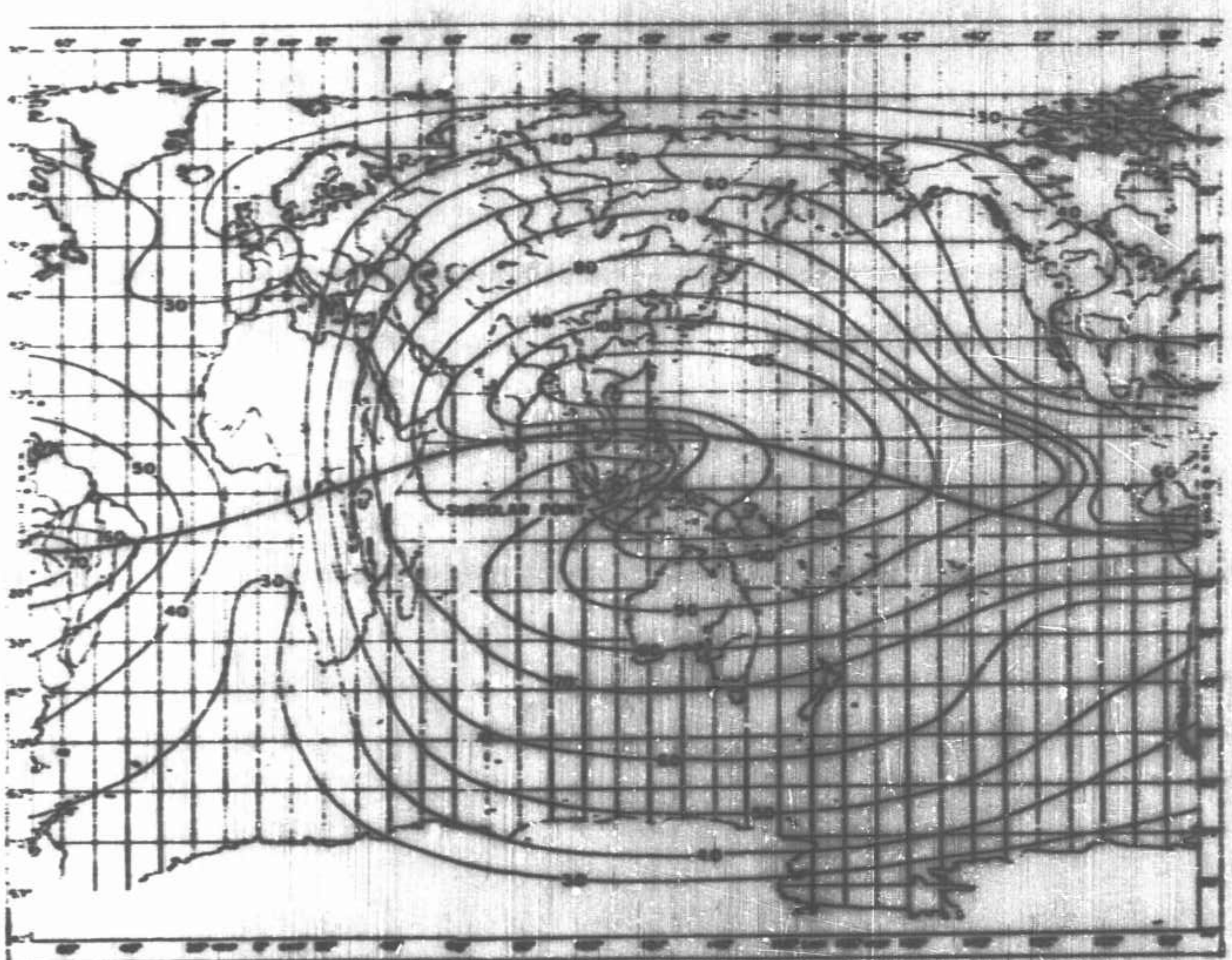

Figure 29. World Wide Distribution of Critical Frequency of F2 Layer (f° F2) in Megacycles for Equinox, 1945, When it is Noon at 111°E.

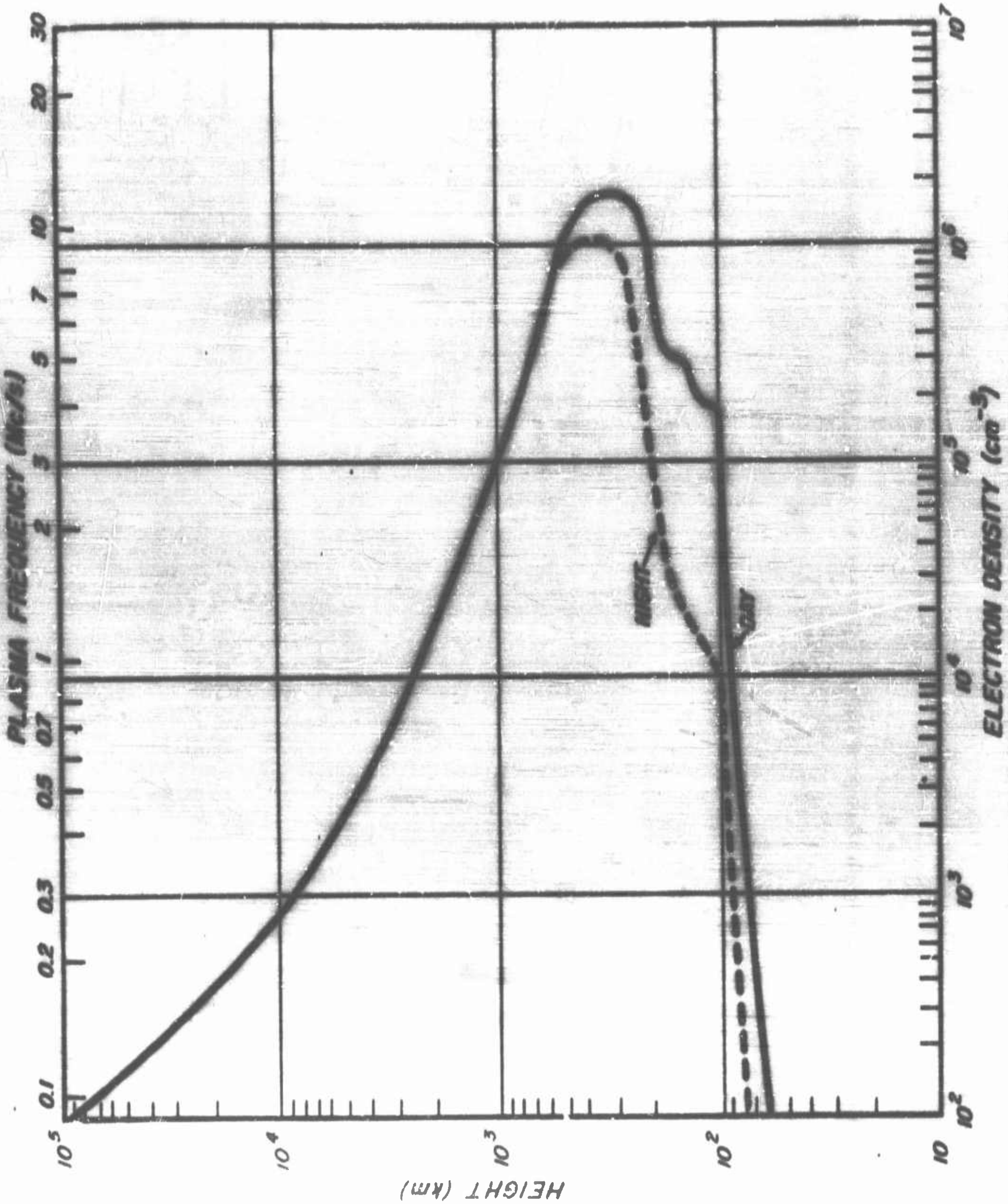

Figure 30. Average Ionosphere: Summer Noon - Middle Latitudes - Sunspot Maximum

importance to the theorist in that it marks the areas where existent theories of hydrodynamics and magnetohydrodynamics may be used to approximate the phenomena. Too frequently in the past, magnetohydrodynamics has been used in regions where the degree of ionization is still small.

Estimates of the degree of ionization at the asymptotic point, the intersection of the terrestrial atmosphere and the solar wind, are available. Tousey et al[22] have made measurements on the self-absorption of the collisionally broadened H-α lines. Hinteregger[23] has investigated the altitude dependence of the solar flux and concluded that if the mean density of inter-planetary space (sun-earth) is of the order of 500 particles/cm^3 and further that the recombination rate-coefficient is 10^{-12} cm^3 sec^{-1} (this is a reasonable value for a radiative recombination process), then the degree of ionization in the solar corpuscular stream is 0.999. With current estimates of the extent of the terrestrial magnetic field as about 5 earth radii, this determines the degree of ionization above 35,000 km. In Figure 30a values are plotted to 700 km using the electron density of the Middle Latitudes at noon for sunspot maximum and the neutral densities of the 1959 ARDC Atmosphere. The latter is not quite appropriate since Jacchia[4] has indicated that with these sub-solar angles, Minzner's[68] values at 700 km are too low by factors of 3 to 5. The values between 700 and 2000 km are taken from Gripp and Christian[69] who extended the Minzner model assuming a constant temperature in the region. The constant

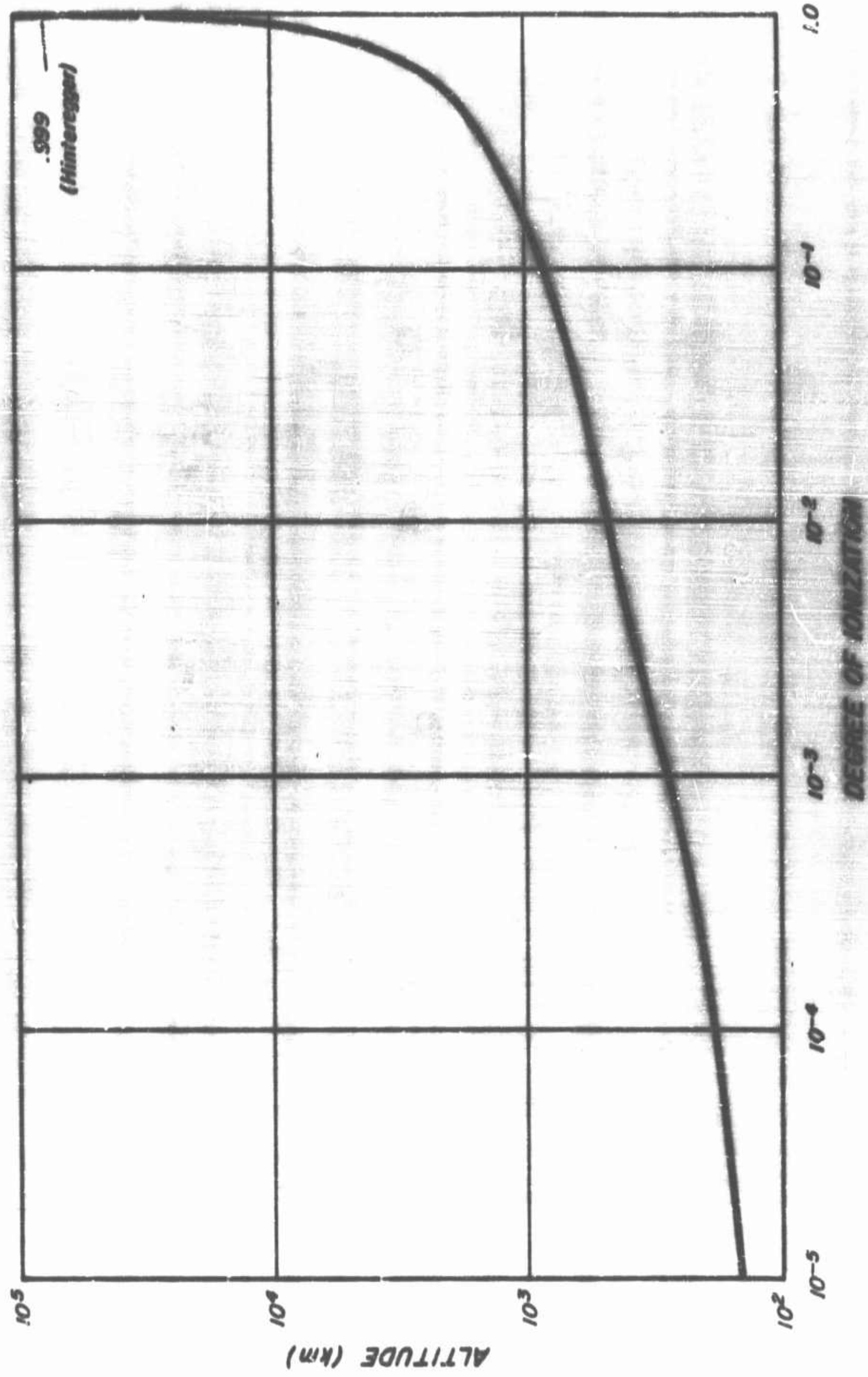

ALTITUDE (km)
10^5
10^4
10^3
10^2
DEGREE OF IONIZATION
10^{-5}
10^{-4}
10^{-3}
10^{-2}
10^{-1}
1.0
.999
(Hinteregger)

Figure 30a

temperature postulate is not favorably considered by Minzner. The profile given in Figure [illegible] must therefore be considered tentative, and the degree of ionization may, as was pointed out, exhibit large secular variations. In spite of its restricted validity, it may point up the basic attributes which determine the selection of an appropriate mathematical discipline.

4. Solar Spectrum

4.1 0-2100 A Region

The major observational gap in the solar spectrum, 100-1100 A, has been largely closed during the past two years by the work of Hinteregger et al,[23] Hense et al,[70] and Tousey et al.[47] Their results (Figure 31, 32 and Table 19) show that the solar spectrum in this region is quite different from all previous estimates or assumed spectra; and for the first time, calculations of ion-production rates for the E and F regions can be based on realistic values of solar flux. Unpublished data [71, 72] of these investigations have supplemented the published data in the construction of Figure 33. The solar spectrum in the range 100-1100 A is very complex; there are many emission lines, both weak and strong and there are also emission continua such as the Lyman continuum of hydrogen which provides a significant amount of energy.

It is well known that radiation intensities in the x-ray region can vary by several orders of magnitude, depending on the "activity" of the sun. Moreover, inherent difficulties in the interpretation of the measured x-ray photon count have led to ambiguities. For example, Friedman et al. originally report the x-ray flux (7-10A) for September 29, 1949, as 10^{-4} erg cm^{-2} sec^{-1}, but later reinterpret the same data as indicative of a flux as high as 0.44 erg cm^{-2} sec^{-1}. Consequently, estimates for this region in the case of the normal sun may be in error by one or more order of magnitude.

THE SOLAR SPECTRUM - APRIL 19, 1960
200 TO 148 KM
USNRL

Figure 31. The Solar Spectrum as Obtained from Rocket Experiment (after Tousey)

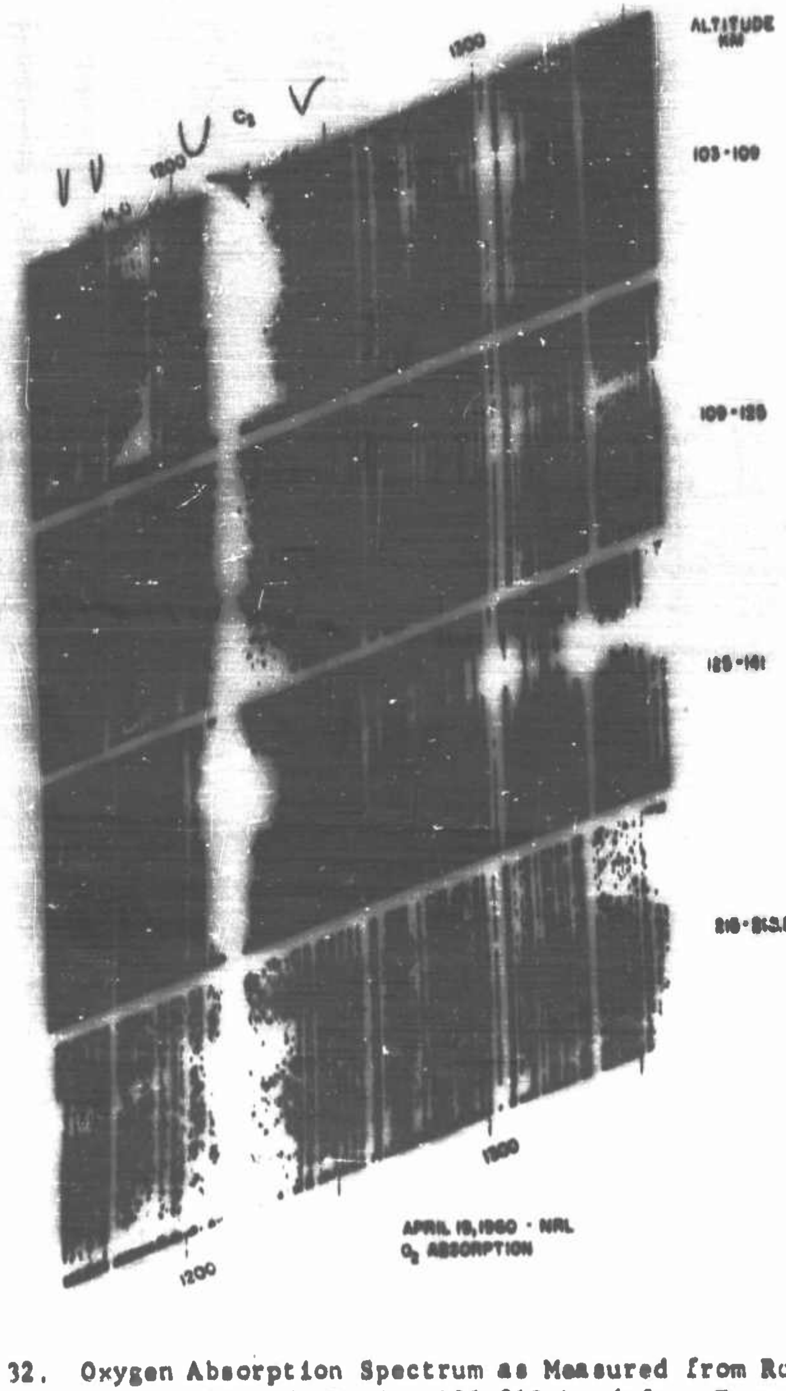

Figure 32. Oxygen Absorption Spectrum as Measured from Rocket Experiment in the Altitude Regime 103-218 km (after Tousey)

SOLAR PHOTON FLUX, INTENSITIES, AND CROSS SECTIONS
Φ_∞ = PHOTON FLUX ON TOP OF THE ATMOSPHERE

WAVELENGTH BAND, OR WAVELENGTH IN ANGSTROMS	SOLAR PHOTON FLUX DENSITY IN $10^9\ CM^{-2}\ SEC^{-1}$		INTENSITIES IN ERGS $CM^{-2}\ SEC^{-1}$		APPROX. IONIZATION CROSS-SECTIONS σ_i IN $10^{-18}\ CM^2$					IONIZATION PROBABILITIES PER UNIT TIME IN UNITS $10^{-9}\ SEC^{-1}$: $\sigma_i \Phi(210\ km)$ WHITE SANDS, NEAR NOON, JAN. 1960			$\sigma_i \Phi_\infty$ ON TOP OF THE ATMOSPHERE				
	Φ_∞	$\Phi(210\ km)$	I_∞	$I(210\ km)$	N	O	N	N_2	He	O	N	N_2	N	O	N	N_2	He
1216	376	370	6.0	6.0													
1300–1040	50	40	.85	.60													
1040–1000	45	36	.90	.72													
1000–950	40	18	.80	.36													
950–912	20	6	.40	.13													
912–850	50	20	1.1	.45	6	3.5				7.0			300	175			
850–650	30	3	.8	.08	4	7	11	(25)		21	33	84	120	210	330	840	
650–475	30	3	1.10	.11	2	14	11	25		42	33	75	60	420	330	750	
475–300	10	1.5	.50	.08	.7	14	7	12	4.5	31	10	18	7.0	160	70	120	45
304	6	3	.40	.20	.3	10	1.7	3.4	1.6	30	5	10	1.8	6[illegible]	10	20	10
300–60	20	12	2.17	1.30						39	10	19	2.4	66	26	53	52
TOTALS 1300–60	670	510	15	10						220	90	200	450	1000	750	1700	100

Table 19 (after Hinteregger)

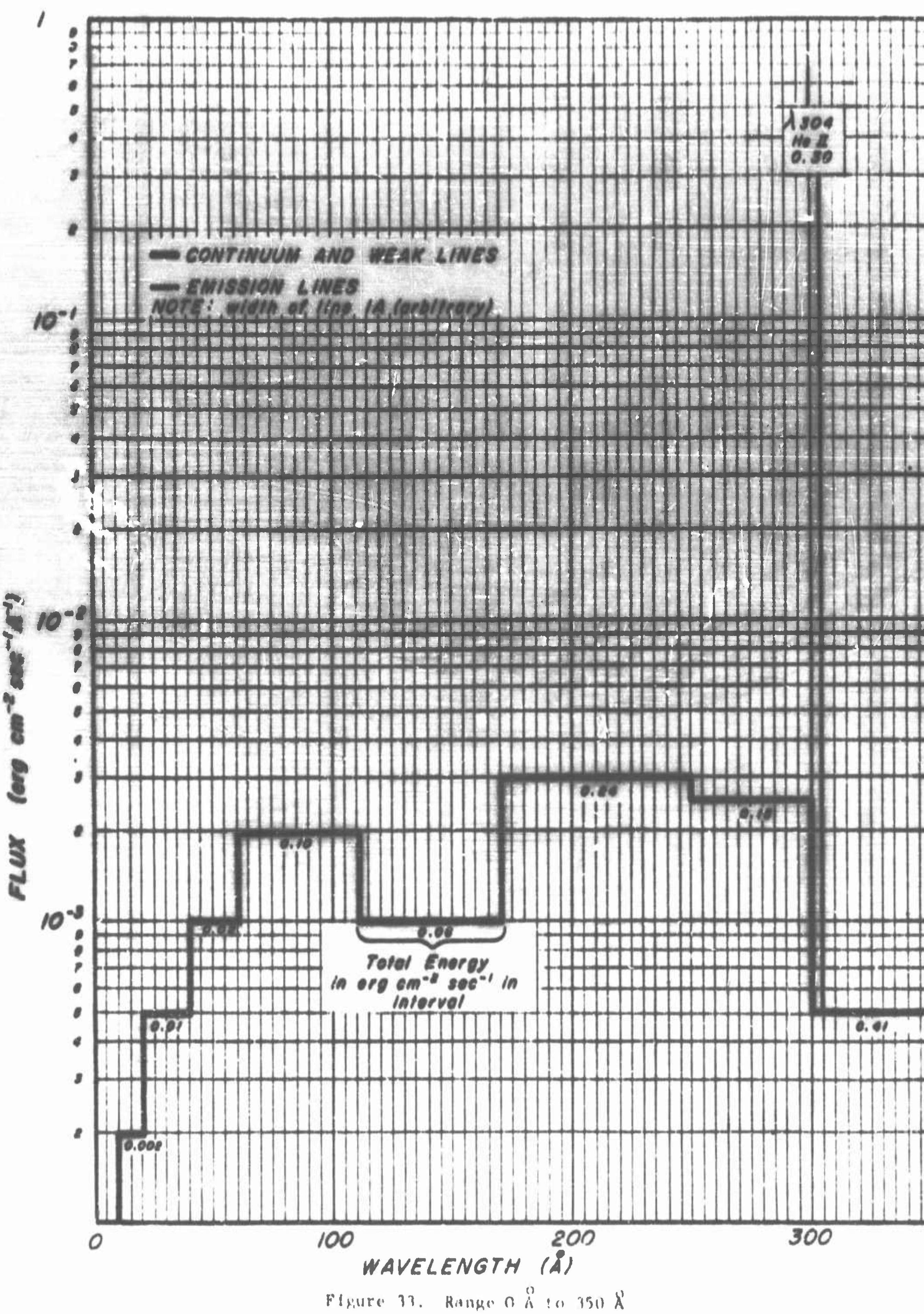

Figure 33. Range 0 Å to 350 Å

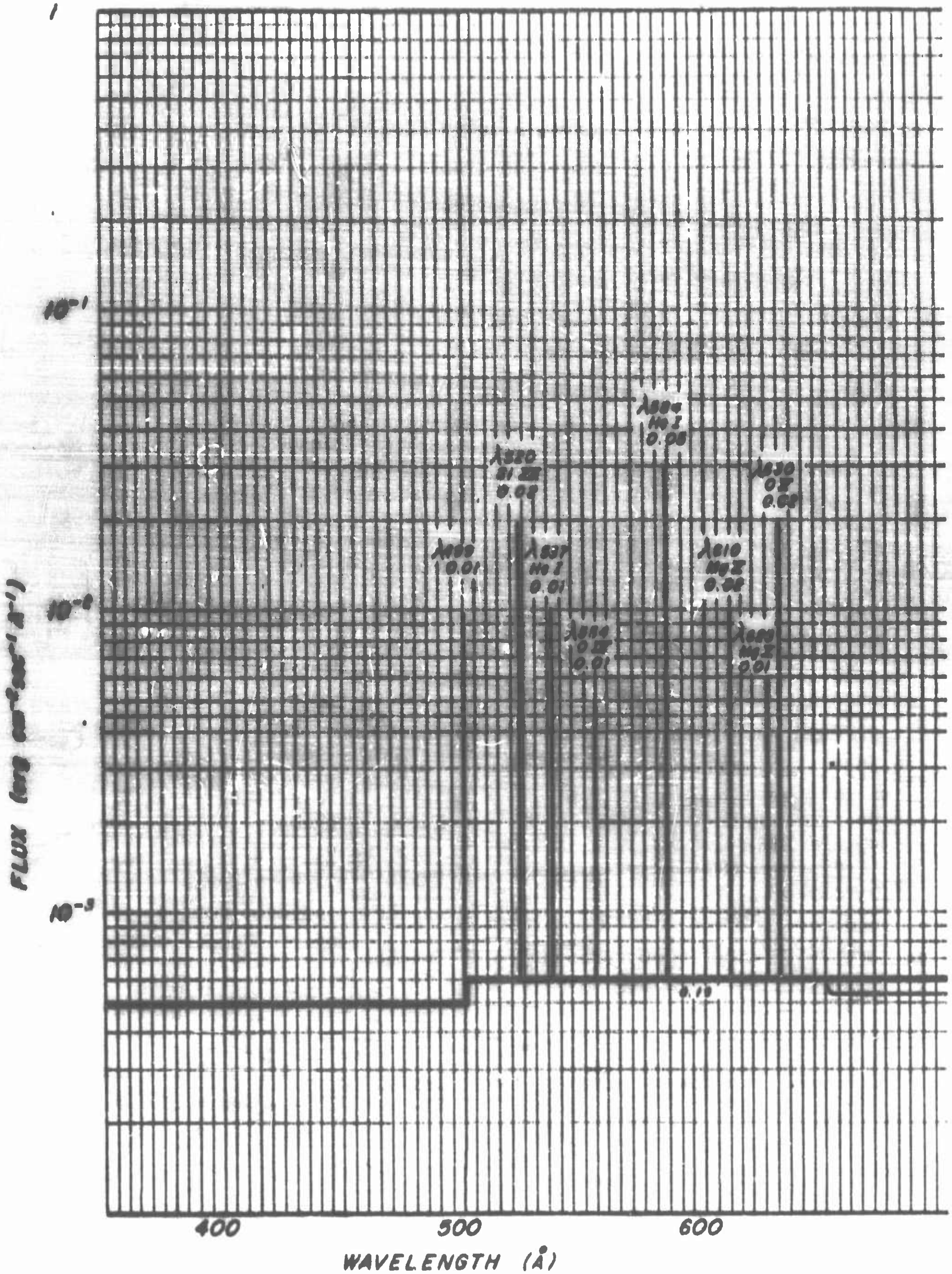

Figure 33 (cont). Range 350 Å to 700 Å

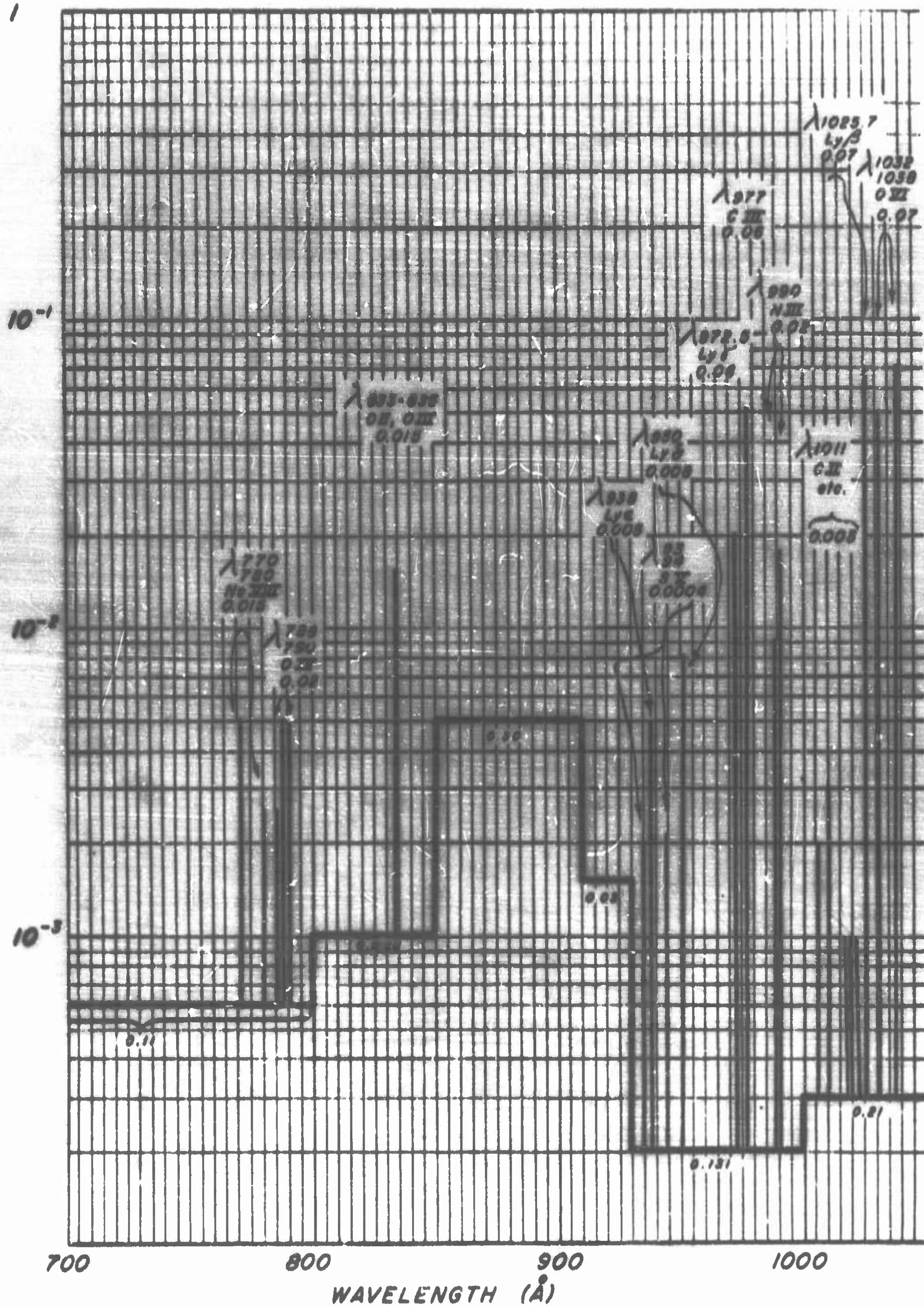

Figure 33 (cont.). Range 700 Å to 1050 Å

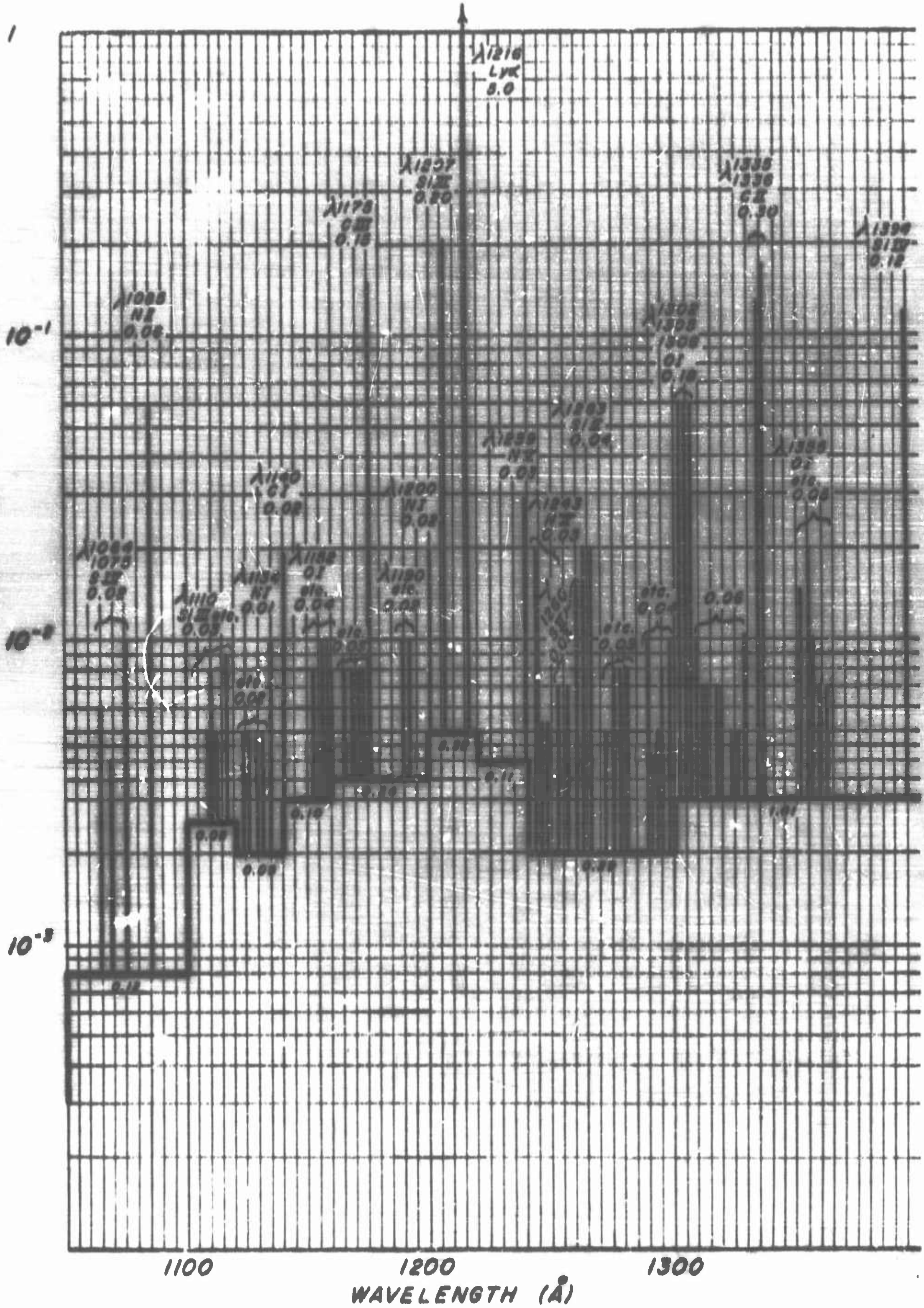

Figure 33 (cont.). Range 1050 Å to 1400 Å

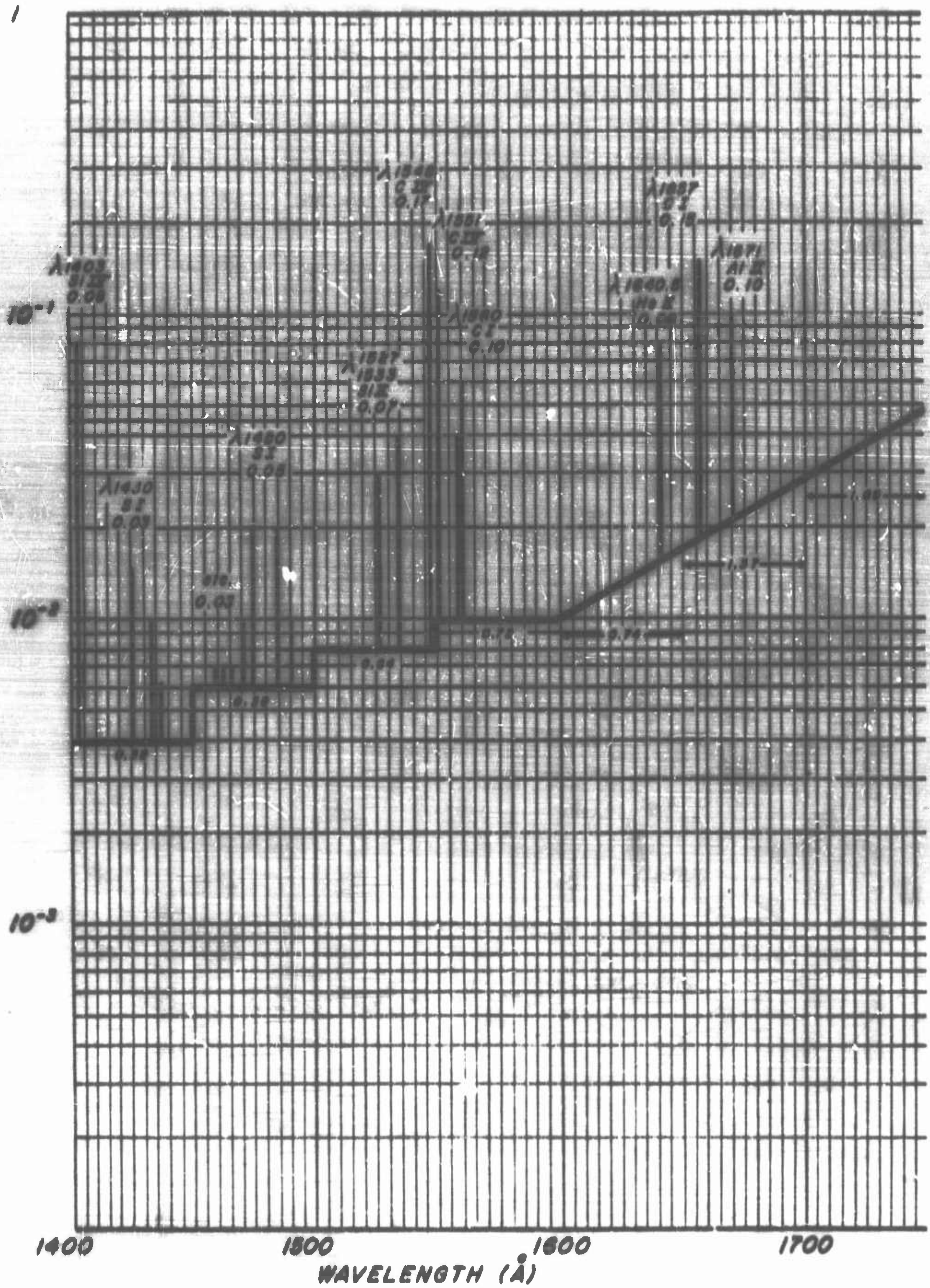

Figure 33 (cont.). Range 1400 Å to 1750 Å

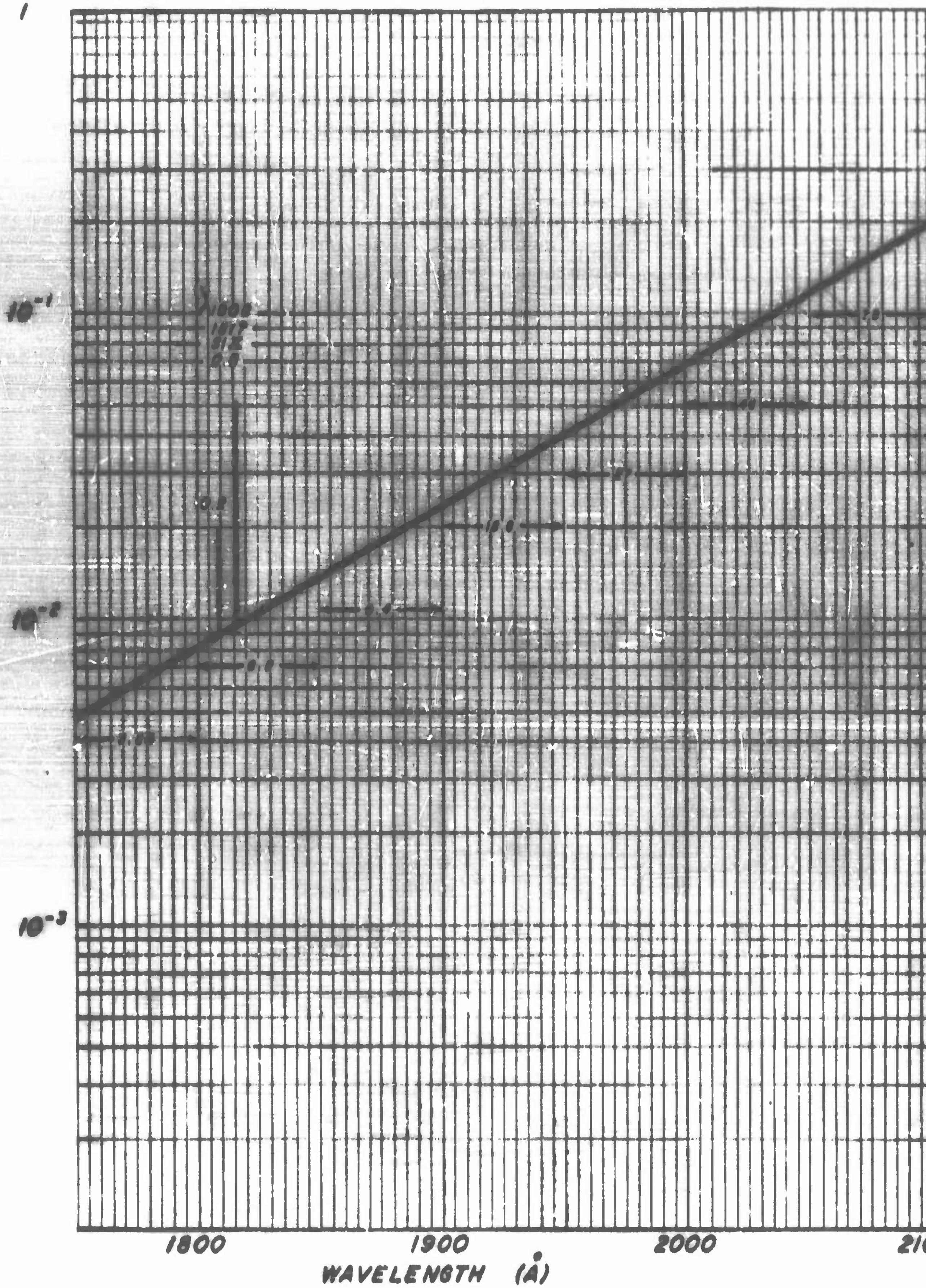

Figure 33 (cont.). Range 1750 Å to 2100 Å

For the region of 60-1300A, Dr. Hinteregger obtained 10 ergs cm^{-2} sec^{-1} at an altitude of 210 km, of which 6.0 ergs cm^{-2} sec^{-1} is attributed to Lyman-alpha. He estimates a total of 15 ergs cm^{-2} sec^{-1} outside of the terrestrial atmosphere. His estimates plus the spectrographs of Dr. Tousey are the principal sources in this region of the spectrum. The total flux pertinent to the tabulated estimates in the region 300-1200A is 11 ergs cm^{-2} sec^{-1}. This value is obtained by correcting Hinteregger's results (for atmospheric absorption) and is, therefore, higher than the uncorrected data of Tousey (taken at 197 km).

For the region of 1200-2100A, estimates of line intensities by Tousey differ from those of Violet and Rense[73] by a factor of about five. Greater weight has been given to Tousey's data in view of the lower contribution of scattered light in the NRL photographs.

As indicative of the uncertainties involved, it is estimated that the line intensities may be in error by a factor of two in most cases, but as high as a factor of five in others. On the other hand, the intensity of the continuum may be in error by a factor of three at frequencies above 300A and by a larger factor at the lower portion of the spectrum. For many of the line intensities, it has been necessary to make estimates on the basis of a visual comparison of the line intensities and the continuum in the spectrographs provided by Dr. Tousey.

The magnitude of the minimum ion production rates can be used as a guide to select the solar flux from the available data. Bates[(6)] has pointed out that the flux used by Haven, Friedman, and Hulburt[(5)] lead to insufficient ionization rates. On the other hand, the flux of 15 ergs cm^{-2} sec^{-1} for the He II line[3] gives too high rates of ionization when the flux of other emission lines and continua is proportionately included. Preliminary calculations for the altitude range 90-400 km indicate that the data by Hinteregger and Tousey can yield reasonable ionization rates.

4.2. Photon Flux from Sun Outside Atmosphere in Region 1000-20,000 Å

Table 20 provides tabulated data of calculated photon fluxes.

Basic information:

Column 1 - Wavelength region (every 50 Å)

2 - Mean wavelength (i.e. 2400-2450 A is 2.42 in cm)

3 - $Q\lambda$ in watts/m^2

4 - $Q\lambda$ converted to ergs/cm^2 sec

1 Watt = 10^7 erg/sec 1 Meter^2 = 10^4 cm^2

$$10^7 \text{ erg/sec} \times \frac{1}{10^4 \text{ cm}} = 10^3 \text{ erg/cm}_2 \text{ sec}$$

5 - $E\lambda$ = energy of photon mean $\lambda = \frac{1.98 \times 10^{-11}}{(10^5)}$ ergs
with λ in cms

6 - $N\lambda = Q\lambda / E\lambda$

7 - $N\lambda$ (running total for increasing wavelengths

Range:

Between	0 - 3500 Å	$\Delta\lambda$ = 50 Å
	3500 - 6000	$\Delta\lambda$ = 50 Å
	6000 - 11,000	$\Delta\lambda$ = 100 Å
	11,000 - 20,000	$\Delta\lambda$ = 1000 Å

TABLE 20

Range (Å)	Mean λ (cm)	Q_λ (watts/m^2)	Q_λ (ergs/cm^{2}sec)	E_λ (ergs)	N_λ	ΣN_λ
0-1000	$0.5x10^{-5}$	.01	$x10^2$	$4x10^{-11}$	$2.5x10^{13}$	
1000-2200	$1.6x10^{-5}$	.27	$2.7x10^2$	$1.24x19^{-11}$	$2.18x10^{13}$	$2.18x10^{13}$
2200-2250	$2.22x10^{-5}$	.14	$1.4x10^2$	$8.92x15^{-12}$	$1.57x10^{13}$	$3.75x10^{13}$
2250-2300	2.28	.26	2.6	8.68	$2.99x10^{13}$	$6.74x10^{13}$
2300-2350	2.32	.27	2.7	8.54	3.16	$9.90x10^{13}$
2350-2400	2.38	.28	2.8	8.32	3.37	$1.33x10^{14}$
2400-2450	2.42	.29	2.9	8.18	3.55	$1.69x18^{14}$
2450-2500	2.43	.30	3.0	7.98	3.76	$2.07x10^{14}$
2500-2550	2.52	.38	3.8	7.86	4.83	2.55
2550-2600	2.58	.53	5.3	7.68	6.90	3.24
2600-2650	2.62	.95	9.5	7.56	$1.26x10^{14}$	4.50
2650-2700	2.68	1.20	$1.2x10^3$	7.39	1.62	6.12
2700-2750	2.72	1.14	1.14	7.28	1.57	7.69
2750-2800	2.78	1.09	1.09	7.12	1.53	9.22
2800-2850	2.82	1.56	1.56	7.02	2.22	$1.14x10^{15}$
2850-2900	2.88	2.42	2.42	6.88	3.52	1.49

TABLE 20 (continued)

Range (Å)	Mean λ (cm)	Q_λ (watts/m^2)	Q_λ (ergs/cm^{2}sec)	E_λ (ergs)	N_λ	$\sum N_\lambda$
2900-2950	2.92	3.08	3.08	6.78	4.54	1.94
2950-3000	2.98	3.02	3.02	6.62	4.56	2.40
3000-3050	3.08	3.50	3.50	6.43	5.44	3.40
3150-3150	3.12	3.90	3.90	6.35	6.14	4.01
3150-3200	3.18	4.05	4.05	6.25	6.48	4.66
3200-3250	3.22	4.65	4.65	6.15	7.56	5.42
3250-3300	3.28×10^{-5}	5.50	5.50×10^{3}	6.04×10^{-12}	9.11×10^{14}	6.33
3300-3350	3.32×10^{-5}	5.60	5.60×10^{3}	5.96×10^{-12}	9.40×10^{14}	7.27×10^{15}
3350-3400	3.38	5.60	5.60	5.86	9.56	8.23
3400-3450	3.42	5.80	5.80	5.79	1.00×10^{15}	9.23
3450-3500	3.48	5.82	5.82	5.69	1.02×10^{15}	1.03×10^{16}
3500-3550	3.52	5.90	5.90×10^{3}	5.62	1.05×10^{15}	1.13×10^{16}
3550-3600	3.58	5.85	5.85	5.53	1.06	1.24
3600-3650	3.62	6.15	6.15	5.47	1.12	1.35
3650-3700	3.68	6.35	6.35	5.38	1.18	1.47

TABLE 20 (continued)

Range (Å)	Mean λ (cm)	Q_λ (watts/m^2)	Q_λ (ergs/cm^2 sec)	E_λ (ergs)	N_λ	ΣN_λ
3700-3750	3.72	6.62	6.62	5.32	1.24	1.59
3750-3800	3.78	6.18	6.18	5.24	1.18	1.71
3800-3850	3.82	6.00	6.00	5.18	1.16	1.83
3850-3900	3.88	5.63	5.63	5.10	1.10	1.94
3900-3950	3.92	5.73	5.73	5.05	1.13	2.05
3950-4000	3.98	7.00	7.00	4.97	1.41	2.19
4000-4050	4.02	8.71	8.71	4.93	1.77	2.37
4050-4100	4.08	9.48	9.48	4.85	1.95	2.57
4100-4150	4.12	9.60	9.60	4.81	2.00	2.77
4150-4200	4.18	9.67	9.67	4.74	2.04	2.97
4200-4250	4.22	9.47	9.47	4.69	2.02	3.17
4250-4300	4.28	8.80	8.80	4.63	1.90	3.36
4300-4350	4.32	8.70	8.70	4.58	1.90	3.55
4350-4400	4.38	9.40	9.40×10^3	4.52	2.08	3.76
4400-4450	4.42	10.40	1.04×10^4	4.48	2.32	3.99

TABLE 20 (continued)

Range (Å)	Mean λ (cm)	Q_λ (watts/m^2)	Q_λ (ergs/cm^{2}sec)	E_λ (ergs)	N_λ	$\sum N_\lambda$
4450–4500	4.48	10.70	1.07×10^4	4.42	2.42×10^{15}	4.23×10^{16}
4500–4550	4.52×10^{-5}	10.89	1.09×10^4	4.38×10^{-2}	2.49×10^{15}	4.48×10^{16}
4550–4600	4.58	10.89	1.09	4.32	2.52	4.73
4600–4650	4.62	10.75	1.08	4.28	2.52	4.98
4650–4700	4.68	10.89	1.09	4.23	2.58	5.24
4700–4750	4.72	10.70	1.07	4.19	2.56	5.50
4750–4800	4.78	10.80	1.08	4.14	2.61	5.76
4800–4850	4.82	10.47	1.05	4.11	2.56	5.92
4850–4900	4.88	10.00	1.00	4.06	2.46	6.17
4900–4950	4.92	10.20	1.02	4.02	2.54	6.42
4950–5000	4.98	10.30	1.03	3.98	2.59	6.68
5000–5050	5.02	9.80	9.80×10^3	3.94	2.49	6.93
5050–5100	5.08	9.80	9.80	3.90	2.51	7.18
5100–5150	5.12	9.65	9.65	3.87	2.49	7.43
5150–5200	5.18	9.60	9.60	3.82	2.51	7.68

TABLE 20 (continued)

Range (Å)	Mean λ (cm)	Q_λ (watts/m^2)	Q_λ (ergs/cm^2 sec)	E_λ (ergs)	N_λ	ΣN_λ
5200-5250	5.22	9.65	9.65	3.79	2.55	7.95
5250-5300	5.28	9.75	9.75	3.75	2.60	8.21
5300-5350	5.32	9.85	9.85	3.72	2.65	8.46
5250-5400	5.38	9.90	9.90	3.68	2.69	8.73
5400-5450	5.42	9.90	9.90	3.65	2.71	9.00
5450-5500	5.48	9.75	9.75	3.61	2.70	9.27
5500-5550	5.52	9.74	9.74	3.59	2.71	9.54
5550-5600	5.58	9.58	9.58	3.55	2.70	9.81×10^{16}
5600-5650	5.62	9.52	9.52	3.52	2.70	1.01×10^{17}
5650-5700	5.68	9.50	9.50×10^{3}	3.49×10^{-12}	2.72×10^{15}	1.04
5700-5750	5.72×10^{-5}	9.57	9.57×10^{3}	3.46×10^{-12}	2.77×10^{15}	1.07×10^{17}
5750-5800	5.78	9.57	9.57	3.43	2.79	1.10
5800-5850	5.82	9.52	9.52	3.40	2.80	1.13
5850-5900	5.88	9.52	9.52	3.37	2.83	1.16
5900-5950	5.92	9.48	9.48	3.34	2.84	1.19

TABLE 20 (continued)

Range (Å)	Mean λ (cm)	Q_λ (watts/m^2)	Q_λ (ergs/cm^2 sec)	E_λ (ergs)	N_λ	$\sum N_\lambda$
5950-6000	5.98	9.35	9.35	3.31	2.83	1.22
6000-6100	6.05×10^{-5}	18.02	1.80×10^{4}	3.28	5.40×10^{15}	1.27
6100-6200	6.15	17.64	1.76×10^{4}	3.22	5.47	1.33
6200-6300	6.25	17.32	1.73	3.18	5.44	1.38
6300-6400	6.35	16.90	1.69	3.12	5.42	1.44
6400-6500	6.45	16.61	1.66	3.07	5.41	1.49
6500-6600	6.55	16.38	1.64	3.02	5.44	1.55
6600-6700	6.65	16.25	1.63	2.98	5.47	2.00
6700-6800	6.75	15.81	1.58	2.93	5.39	2.06
6800-6900	6.85	15.39	1.54	2.89	5.33	2.11
6900-7000	6.95	14.95	1.50	2.85	5.26	2.16
7000-7100	7.05	15.06	1.50	2.81	5.34	2.22
7100-7200	7.15	14.41	1.44	2.77	5.20	2.27
7200-7300	7.25	14.20	1.42	2.73	5.20	2.32
7300-7400	7.35	13.90	1.39	2.69	5.17	2.37

TABLE 20 (continued)

Range (Å)	Mean λ (cm)	Q_λ (watts/m^2)	Q_λ (ergs/cm^{2}sec)	E_λ (ergs)	N_λ	$\sum N_\lambda$
7400-7500	7.45	13.47	1.35	2.66	5.19	2.48
7500-7600	7.55	13.59	1.36	2.62	5.19	2.48
7600-7700	7.65	12.98	1.30	2.59	5.02	2.53
7700-7800	7.75	12.53	1.25×10^{4}	2.56×10^{-12}	4.88×10^{15}	2.61×10^{17}
7800-7900	7.85×10^{-5}	12.38	1.24×10^{4}	2.52×10^{-12}	4.92×10^{15}	2.66×10^{17}
7900-8000	7.95	12.08	1.21	2.49	4.86	2.71
8000-8100	8.05	11.90	1.19	2.46	4.84	2.76
8100-8200	8.15	11.58	1.16	2.43	4.78	2.81
8200-8300	8.25	11.45	1.15	2.40	4.79	2.86
8300-8400	8.35	11.01	1.10	2.37	4.64	2.91
8400-8500	8.45	10.71	1.07	2.34	4.57	2.96
8500-8600	8.55	10.51	1.05	2.32	4.52	3.00
8600-8700	8.65	10.21	1.02	2.29	4.45	3.04
8700-8800	8.75	10.08	1.01	2.26	4.47	3.08
8800-8900	8.85	9.93	9.93×10^{3}	2.24	4.43	3.12

TABLE 20 (continued)

Range (Å)	Mean λ (cm)	Q_λ (watts/m^2)	Q_λ (ergs/cm^{2}sec)	E_λ (ergs)	N_λ	ΣN_λ
8900-9000	8.95	9.63	9.63	2.21	4.36	3.17
9000-9100	9.05	9.27	9.27	2.19	4.23	3.21
9100-9200	9.15	9.14	9.14	2.17	4.21	3.25
9200-9300	9.25	8.99	8.99	2.14	4.20	3.29
9300-9400	9.35	8.77	8.77	2.12	4.14	3.33
9400-9500	9.45	8.55	8.55	2.10	4.07	3.37
9500-9600	9.55	8.25	8.25	2.08	3.97	3.41
9600-9700	9.65	8.15	8.15	2.05	3.97	3.45
9700-9800	9.75	8.09	8.09	2.03	3.99	3.49
9800-9900	9.85	7.54	7.54	1.99	3.79	3.53
9900-10000	9.95	7.54	7.54	1.99	3.79	3.57
10000-10100	10.05	7.30	7.30	1.97	3.71	3.61
10100-10200	10.15×10^{-5}	7.15	7.15×10^{3}	1.95×10^{-12}	3.67×10^{15}	3.65×10^{17}
10200-10300	10.25×10^{-5}	7.02	7.02×10^{3}	1.93×10^{-12}	3.64×10^{15}	3.69×10^{17}
10300-10400	10.35	6.87	6.87	1.92	3.58	3.73

TABLE 20 (continued)

Range (Å)	Mean λ (cm)	Q_λ (watts/m^2)	Q_λ (ergs/cm^{2}sec)	E_λ (ergs)	N_λ	$\sum N_\lambda$
10400-10500	10.45	6.73	6.73	1.90	3.54	3.77
10500-10600	10.55	6.60	6.60	1.89	3.49	3.80
10600-10700	10.65	6.46	6.46	1.87	3.46	3.83
10700-10800	10.75	6.33	6.33	1.86	3.40	3.87
10800-10900	10.85	6.19	6.19	1.85	3.35	3.90
10900-11000	10.95×10^{-5}	6.05	6.05	1.83	3.31	3.94×10^{17}
11000-12000	11.5	52.92	5.29×10^{4}	1.72×10^{-2}	3.07×10^{16}	4.25
12000-13000	12.5	42.29	4.23	1.59	2.66	4.52
13000-14000	13.5	34.06	3.41	1.47	2.32	4.75
14000-15000	14.5	27.68	2.77	1.37	2.02	4.95
15000-16000	15.5	22.65	2.27	1.28	1.78	5.13
16000-17000	16.5	18.70	1.87	1.20	1.56	5.29
17000-18000	17.5	15.55	1.56	1.13	1.38	5.43
18000-19000	18.5	13.02	1.30	1.07	1.22	5.55
19000-20000	19.5	10.98	1.10	1.02	1.08×10^{16}	5.66×10^{17}

1. Nicolet, M. - "Physics of the Upper Atmosphere" (Academic Press; New York) Ed. J. Ratcliffe (1960)

2. King-Hele, D. G., G. E. Cook, and D. M. C. Walker, Roy. Aircraft Establishment (Farnborough) Tech. Note G.W. 533, (1959)

3. Jacchia, L. G., Smithsonian Astrophys. Observatory Spec. Rept. 20, 1959a.

4. Jacchia, L. G., Nature, 183, 526-527, (1959b)

5. Jacchia, L. G., Smithsonian Astrophys. Observatory Spec. Rept. 13, (1958)

6. Bates, D. R., Proc. Roy. Soc. A257, 22 (1960)

7. Omholt, A. J. Atmos. Terr. Phys. 10, 320 (1957)

8. Bates, D.R., Proc. Roy. Soc. B64, 805 (1951)

9. Harang, L., Geophys. Publ. 20 No. 5 (1958)

10. Harang, L. and Omholt A. Geophys. Publ. (in press) (1960)

11. Van Allen, J. A., McIlwain, C. E. and Ludwig, G. A., J. Geophys. Res. 64, 271 (1959)

12. Krassovsky, V. I. Space Research (North-Holland:Amsterdam) Ed. H. Kallman (1960)

13. Bates, D. R., Proc. Roy. Soc. A253, 451 (1959)

14. Dessler A. J. and Vestine E.H., J. Geophys. Res. 65, 1069 (1960)

15. Jastrow, R. J. Geophys. Res. 64, 789 (1959)

16. Jastrow, R., Space Research (North-Holland:Amsterdam) Ed. A. Kallman (1960)

17. Dalgarno, A., Geophysics Corporation of America Technical Report No. 60-4-G (1960)

18. Dessler, A. J. J. Geophys. Res. 64, 347 (1959)

19. Bates, Dr. and Nicolet, M. J. Atmos. Terr. Phys. 18, 65 (1960)

20. Miller, L. J. Geophys. Res 62, 351 (1957)

21. Bricard, J. J. Geophys. Res. 54, 39 (1949)

22. Tousey, R., Purcell, J. C. and Parker, D. M., paper presented at the "First International Space Science Symposium" Nice (1960); private communication

23. Hinteregger, H. et al, paper presented at the "First International Space Science Symposium" Nice (1960); private communication

24. Nicolet, M. and Aiken, A. C., J. Geophys. Res. 65, 1469 (1960)

25. Kistiakowsky, G. B. and Volpi, G., J. Chem. Phys. 27, 1141 (1957)

26. Papa, R., "Cosmic Rays and Geomagnetism" Geophysics Corporation of America Technical Report, to be published (1960)

27. Nawrocki, P. J. and Papa, R., "Energy Loss Processes of Solar Corpuscles In Air" Geophysics Corp. of America Technical Report 61-12-A (AFCRL 26)

28. Wulf, O. R. and Deming, L. S., Terre. Mag. Atmos. Elect. 43, 283 (1938).

29. Nicolet, M., Mem. Inst. R. Met. Belgique, 19, 124 (1945)

30. Vegard, L., Geofys. Publ. 12, No 5 (1938).

31. Hulburt, E. O., Phys. Rev. 53, 344 (1938).

32. Bates, D. R., Proc. R. Soc. (London) A196, 562 (1949).

33. Nicolet, M., Ann. Geophys. 8, 141 (1952).

34. Choudhury, D. C., Phys. Rev. 88, 405 (1952)

35. Byram, E. T., Chubb, T. A. and Friedman, H., Phys. Rev. 92, 1066 (1953)

36. Bauer, E. and Wu, T. Y., Phys. Rev. 92, 1101 (1953)

37. Rawer, K. and Argence, E., Phys. Rev. 94, 253 (1954)

38. Sato, T., Rep. Ionosphere Res. (Japan) 8, 49 (1954)

39. Watanabe, K., Marmo, F. F., and Pressman, J., J. Geophys. Res. 60, 513 (1955).

40. Houston, R. E., J. Atm. Terr. Phys. 12, 225 (1958)

41. Kamiyama, H., Science Rept. Tohoku Univ. (Japan) 11, 98 (1959).

42. Appleton, E. V., See for example. Proc. IRE, 47, 155 (1959)

43. Byram, E. J., Chubb, T. A. and Friedman, H., J Geophys. Res. 61, 251 (1956).

44. Friedman, H. Astrophys. J. 129, 193 (1959)

45. Bates, D. R., "Solar Eclipse and the Ionosphere" Special Supplement Vol. 5, J. Atmos. Terr. Physics, 191 (1956)

46. Ratcliffe, J. A. and Weekes, K., Astrophys. J. 129 417(1956)

47. Tousey, R., Purcell, J. D. and Packer, D. M., paper presented at the "First International Space Science Symposium", Nice (1960); private communication.

48. Watanabe, K.,"Advances In Geophysics 5, 153 (1958)

49. Dalgarno, A.,"Charged Particles In the Upper Atmosphere" GCA Technical Report 60-4-G

50. Kato, S., J. Geomagn. Geoelectricity (Japan) 4, 153 (1954).

51. Brandt, J. C., Astrophys. J. 129, 228 (1959):

52. Purcell, J. D. and Tousey, R., In "Physics of the Upper Atmosphere: edit. by J. A. Ratcliffe, Academ. Press, p. 557, (1960).

53. Watanabe, K. and Marmo, F. F., J. Chem. Phys. 25, 965 (1956).

54. Itamoto, F., Matsunoga, F., McAllister, H., and Watanabe, K., unpublished material. Univ. of Hawaii (1960)

55. Chapman, S., Proc. Phys. Soc. 43, 26 (1931); 43, 484 (1931).

56. Chapman, S., Proc. Phys. Soc. 51, 93 (1939).

57. Chapman, S., Proc. Phys. Soc. B 67, 717 (1954)

58. Nicolet, M. and Bossy. L., Ann. De Geoph. 5, 275 (1949)

59. Glendhill, J. A. and Szendrei, M. E., Proc. Phys. Soc. B 63 427 (1950).

60. Havens, R. J., Friedman, H. and Hulburt, E. O., in "Physics of the Ionosphere", Physical Society, London, p. 237 (1955).

61. Johnson, F. S. J. Geophys. Res. 61, 71 (1956).

62. Jackson, J. E., Astrophys. J. 129, 108 (1959)

63. Mitra, S. K. "The Upper Atmosphere" second ed. The Asiatic Society, Calcutta (1952).

64. Bradbury, N. E., Terr. Mag. Atmos. Elect, 43, 55 (1938).

65. Bates, D. R. and Massey, H. S. W., Proc. Roy, Soc. 187, 261 (1946).

66. Mitra, A. P. and Jones, R. E., J. Geophys. Res. 59, 391 (1954).

67. Johnson, C. Y., Meadows, E. B., Holmes, J. C., J. Geophys. Res. 63, 443 (1958).

68. Minzner, R. A., Champion, K. S. W. and Pond, H., "The ARDC Model Atmosphere, 1959" AFCRC-TR-59-267 (1959)

69. Gripp, A. P. and Christian, R. H., private communication

70. Reese, M. H. and Rense, W. A., J. Geophys. Res. 64, 1251 (1959)

71. Hinteregger, H. E., private communication (1960). Copy of paper to be published in the Astrophysics Journal.

72. Tousey, R., private communication (1960). A table of estimated intensities, photographs of solar spectrum (1960).

73. Violet, R. and Rense, W. A., Astrophys. J. 130, 954 (1959).